Alexander Adelmann, BSc

Investigation of the Temperature Distribution in Co-Rotating Twin-Screw Extruders

MASTER'S THESIS

to achieve the university degree of

Diplom-Ingenieur

Master's degree programme: Biomedical Engineering

submitted to

Graz University of Technology

Supervisor

Ao.Univ.-Prof. Dipl.-Ing. Dr.techn. Hermann Scharfetter

Institute of Medical Engineering

Istvan Kondor, MSc
Research Center Pharmaceutical Engineering

Graz, November 2017

AFFIDAVIT

I declare that I have authored this thesis independently, that I have not used other than the declared sources/resources, and that I have explicitly indicated all material which has been quoted either literally or by content from the sources used. The text document uploaded to TUGRAZonline is identical to the present master‘s thesis.

Date	Signature

Abstract

Intermeshing extruders are most commonly used in the polymer and food industries, but lately the importance of extrusion in the pharmaceutical industry is increasing related to the production of solid drug products. Although extruders have been used for decades, the process of extrusion is not well understood yet.

Simulations are not routinely carried out because of the complex intermeshing geometry of the screw elements. Common simulations approaches are struggling with the intermeshing region of the screws. Moreover, it is also difficult to predict the shape of the free surface in partially filled regions. Since Smoothed Particle Hydrodynamics (SPH) can handle moving and intermeshing boundaries and also predict free surfaces it is a promising modeling approach. Compared to regular mesh-based CFD methods, such as FVM, SPH cannot handle complex wall boundaries properly. To overcome this difficulty a potential-based wall interaction model has been developed by Andreas Eitzlmayer [1].

Based on this work I want to investigate hot melt extrusion and therefore calculate the temperature distribution in Co-Rotating Twin-Screw Extruders using SPH as the modeling approach to get a deeper understanding of the HME process and therefore contribute to possible scale up techniques or screw design optimisations. Since hot melt extrusion has the potential to solve problems related to poorly soluble drug molecules via amorphous solid dispersion formation, this work is significant for the pharmaceutical industry.

Acknowledgement

First and foremost I want to thank my supervisor Ao.Univ.-Prof. Dipl.-Ing. Dr.techn. Hermann Scharfetter, dean of the Institute of Medical Engineering at the TU-Graz for accepting and mentoring my master thesis.

I would like to express my deepest gratitude to my supervisor MSc Isvtan Kondor of the Research Center for Pharmaceutical Engineering at the TU-Graz for his excellence guidance, help, motivation, and knowledge he shared with me.

Furthermore I want to thank Dipl.-Ing. Josip Matic and Dipl.-Ing Hannes Bauer of the RCPE for their support and the discussions we had.

The Research Center Pharmaceutical Engineering has provided the support and equipment I have needed to complete my thesis.

Finally I want to thank my loved ones, my parents, sister, partner and friends for always supporting me throughout all my studies.

Contents

Abstract i

Acknowledgement iii

Contents v

List of Figures ix

List of Tables xiii

1. Introduction 1

1.1. Overview & importance of hot-melt extrusion 1

1.1.1. Hot melt extrusion process and extruder setup 2

1.1.2. Descriptive features of co-rotating TS-HME 10

1.1.3. Monitoring and controlling parameters of HME 10

1.1.4. Pharmaceutical applications of HME 12

1.1.5. Materials used in HME 17

1.1.6. Marketed products 20

1.2. Overview & advantages of SPH in HME 20

1.2.1. Experimental approach 20

1.2.2. 1D simulations 22

1.2.3. 3D simulations 22

1.2.4. Simulation studies 25

2. Modeling approach 31

2.1. Thermodynamics and fluid modeling 31

2.1.1. Governing equations 31

2.1.2. Heat transfer 33

2.1.3. Rheological properties 33

2.1.4. Shear flows 41

2.1.5. Molecular parameters influencing polymer melts 42
2.1.6. Dimensionless relations in fluid dynamics 42
2.2. Equations of SPH 43
2.3. The foundation 43
2.3.1. Smoothing length 45
2.3.2. Discrete Lagrangian 46
2.3.3. Derivation of Euler Lagrange 46
2.3.4. Equation of motion 47

3. Comparison **51**
3.1. Pressure and drag flow 51
3.1.1. Couette flow 51
3.1.2. Poiseuille flow 53
3.2. Heat transfer 54
3.3. Viscous heating 55
3.4. Power law viscosity 56
3.5. Viscous heating in Couette flow for Newtonian and Powerlaw fluids 57
3.5.1. Newtonian fluids with exponential temperature dependent viscosity and constant thermal conductivity 59
3.5.2. Non-Newtonian fluids with temperature dependent viscosity and thermal conductivity 59
3.6. Back flow characteristics 61

4. Simulation details **65**
4.1. Geometries, materials and operating conditions 65
4.1.1. Geometries: 65
4.1.2. Materials: 65
4.1.3. Simulation setting: 67
4.1.4. Master curve 68
4.1.5. Hardware and computational time 69

5. Results **71**
5.1. Heat-up rate 71
5.2. Pressure characteristics 72
5.3. Temperature characteristics 74
5.4. Frozen Simulation approach 88

6. Conclusion 89

Bibliography 91

A. Algebraic and differential operations for scalars, vectors and tensors for Cartesian coordinates A-1

B. C++ source code B-3

List of Figures

1.1.1. The Cochlea Archimedis as the origin of the first extruder screw [2]. 2
1.1.2. Schematic principles of TS-HME [3]. 3
1.1.3. Stand-alone 20mm Clamshell Segmented TSE 20/40 [4]. 6
1.1.4. A variety of the sections of a co-rotating twin-screw extruder. . . 6
1.1.5. Various mixing zones of an extrusion screw [5]. 8
1.1.6. End-view of intermeshing twin-screw extruder [5]. 9
1.2.1. Triangulations to build the mesh [6]. 23
1.2.2. Mesh of the conveying element of a screw. 23
1.2.3. Factors affecting the polymerization in TSE with FLUENT [7]. . 28

2.1.1. Range of application of the power-law viscosity models. 37
2.1.2. Newtonian, pseudo plastic and dilatant characteristics. 37
2.1.3. Overview of the viscous behaviour of a variety of models. 38
2.3.1. SPH approach to computed the density [8]. 44
2.3.2. Support domain with the kernel function W [9]. 45

3.1.1. Sketch of the simulation setup for a Couette flow. 51
3.0.1. Geometry of the channel flow simulation. 52
3.0.2. Post view of the simulation for the heat transfer of $\triangle T$ is 1 Kelvin for 0.1 second. 52
3.1.2. Velocity profile of a drag induced flow for 1, 6 and 30 ms, [10]. . . 53
3.1.3. Sketch of the simulation setup for a Poiseuille flow 53
3.1.4. Velocity profile of a pressure induced flow for 1, 6 and 30 ms, [10]. 54
3.2.1. Sketch of the simulation setup for the heat transfer 54
3.2.2. Temperature profile for 0.06 , 0.1 and 1 s. 55
3.3.1. Sketch of the simulation setup for viscous heating 55
3.3.2. Temperature profile with viscous heating for 5 ms. 56
3.4.1. Sketch of the simulation setup for a power law viscosity in a Couette flow 56

3.4.2.Sketch of the simulation setup for a power law viscosity in a Poiseuille flow 56

3.4.3.Viscosity profile of a non-Newtonian pseudo-plastic drag driven fluid flow. 57

3.4.4.Viscosity profile of a non-Newtonian pseudo-plastic pressure driven fluid flow. 58

3.5.1.Sketch of the simulation setup for a power law viscosity in a Couette flow. 59

3.5.5.Sketch of the simulation setup for a power law viscosity in a Couette flow. 59

3.5.2.Velocity profiles for Newtonian fluids with temperature dependence. 60

3.5.3.Temperature profiles for Newtonian fluids with temperature dependence. 60

3.5.4.Viscosity profiles for Newtonian fluids with temperature dependence. 61

3.6.1.Sketch of the back flow simulation setup for a Newtonian fluid. . 61

3.5.6.Velocity profiles for non-Newtonian fluids with temperature dependence. 62

3.5.7.Temperature profiles for non-Newtonian fluids with temperature dependence. 62

3.5.8.Viscosity profiles for non-Newtonian fluids with temperature dependence. 63

3.6.2.Sketch of the back flow simulation setup for a non-Newtonian fluid. 63

3.6.3.Velocity profile of the Couette-Poiseuille-backflow for Newtonian fluids. 64

3.6.4.Velocity profile of the Couette-Poiseuille-backflow for non-Newtonian fluids. 64

4.1.1.Geometry of an double flighted intermeshing conveying element and within a barrel [11]. 66

4.1.2.Detail 1 of the conveying element displaying the gab of 0.5mm between the extruder screws [11]. 66

4.1.3.Comparison of the viscosity models and experimental data of Soluplus at 140, 150 and 160°C. 68

5.1.1.Qualitative post view of the heat generation in rotating cylinders. 71

5.1.2.Qualitative post view of the velocity of the particles in rotating cylinders. 72

5.2.1.Pressure characteristic and throughput in extrusion. 73

5.2.2.Pressure characteristics of the conveying element. 74

5.3.1. Times to reach a steady state temperature distribution of the test cases 1-6. 75
5.3.2. Velocity and temperature profiles of case 1. 77
5.3.3. Velocity and temperature profiles of case 2. 78
5.3.4. Viscosity profiles of case 2. 79
5.3.5. Velocity and temperature profiles of case 3. 80
5.3.7. Viscosity profiles of case 4 81
5.3.6. Velocity and temperature profiles of case 4. 82
5.3.8. Velocity and temperature profiles of case 5. 83
5.3.9. Viscosity profiles of case 5. 84
5.3.10. Velocity and temperature profiles of case 6. 85
5.3.11. Viscosity profiles of case 6. 86
5.3.12. Lowest viscosity and highest temperature of case 2 and case 6. . . 87
5.4.1. Post view of the heat generation in rotating cylinders. 88

List of Tables

1.1.1. Setting and processing parameters in HME. 3

1.1.2. Summary of the extruder zones and the corresponding tasks, parameters and characteristics. 7

1.1.3. Properties of some generic Polymers. 17

1.1.4. Temperature-range for different materials used in HME. 18

1.1.5. Melting temperature of a set of drugs. 19

1.1.6. Products manufactured by HME. 20

3.5.1. Boundary Conditions for the channel flow. 58

4.1.1. Geometry parameters of the conveying element in HME. 65

4.1.2. Geometry parameters of the rotating cylinders. 66

4.1.3. Material parameters used in the simulation. 67

4.1.4. Simulation settings used in the simulation of the extruder. 67

4.1.5. Simulation settings used for the cylinder simulation. 67

4.1.6. Computation time of the channel flow simulations. 69

4.1.7. Computation time of the cylinder simulations 69

4.1.8. Computation time of the extruder simulations. 69

4.1.9. Development of the GPU performance. 70

5.3.1. Modifications of the test cases 1-6. 75

5.3.2. Overview of the times to reach steady state. 76

5.3.3. Minimum, maximum and average temperature of the test cases 1-6. 76

List of Symbols

Abbreviation:

APIs	Smoothed Particle Hydrodynamics
HME	Hot Melt Extrusion
APIs	Active Pharmaceutical Ingredients
scCO2	Supercritical carbon dioxide
HSEI	High-speed energy input
LSLF	Low-speed late fusion
CQAs	Critical quality attributes
CELF	Standard deviation of
ELF	Extruder load factor
SME	Specific mechanical energy
NMR	Nuclear magnetic resonance imaging
LDA	Laser doppler anemometer
SSE	Single screw extruder
SVD	Slit die viscometers
TSE	Twin screw extruder
IR	Infrared
PE	Polyethylene
CFD	Computational fluid dynamic
FVM	finite volume method
FEM	Finite element
FDM	Finite discrete models
PDEs	Partial differential equations

Latin letters:

A	Area
a	Acceleration
Br	Brinkman number
c_p	Heat capacity
D	Diameter
d	Number of spatial dimensions
E_A	Activation Energy
$\mathbf{f}$	Friction coefficient
F_n	Friction force
h	Smoothing length
I	Identity matrix
K	Consistency index
L	Lagrangian equation
m	Mass
n	Power law index
p	Pressure
Pr	Prandtl number
$\dot{Q}$	Frictional heat
R	Gas constant
r	Particle position
Re	Reynolds number
s	Entropy
t	Time
T	Temperature
u	Internal energy per unit mass
U	Internal energy per unit volume
V	Potential Energy
v	Velocity
$\mathbf{v}$	Flux
W	Weight function

Greek letters:

α	Thermal diffusivity
β	Dimensionless coefficient in exponential viscosity-temperature relation
γ	Shear rate
δ	Dirac delta
η	Dynamic viscosity
θ	Dimensionless temperature rise
κ	Thermal conductivity
λ	Time constant
μ	Viscosity
ξ	Dimensionless rectangular coordinate
ρ	Density
σ	Normal stress
τ	Shear stress
ϕ	Viscous dissipation
Θ	Dimensionless temperature rise
Ω	Equi-spaced particles

Chapter 1.

1 Introduction

1.1. Overview & importance of hot-melt extrusion

The basic principle of hot melt extrusion (HME) consists of axially conveying and melting a polymer by applying heat and pressure before “squeezing” it through an opening under controlled conditions to produce a well-mixed and uniformly shaped polymer product with homogeneous density. The extruder screw dates back to 225 B.C. This invention allowed to move water out of a leaking ship. Archimedes in Syracuse, the inventor of the first extruder screw named the invention Cochlea Archimedis, described in the four books on “de Cochlea” by Guidobaldo Del Monte (1545-1607), stated by Aterini et al. [12]. In Figure 1.1.1 the Cochlea Archimedis for the purpose of lifting water from the Nile, is shown, presented by Haberbusch and Bata et al. [2, 13].

The first applications carried out by HME was the manufacturing of lead pipes and can be dated back to the end of the 18’s century, stated by Jani et al. [14]. By introducing the first screw compounder (ZSK, Zweiwellige Knetscheiben Schneckenpresse) by Werner & Pfleiderer in 1957 [15], the success story of twin screw extruders has begun. Until now it is one of the most important processing technologies in the rubber, plastic and food manufacturing industries, captured by Singhal et al. [16]. Products such as hoses, cables and polystyrene tiles are made of plastic that is manufactured by HME. Acrylics, cellulosics, or poly propylene are some of the substances used for the production of this plastics. Another application of HME called extrusion cooker is used in the food industry to produce pasta. In the veterinary and animal feed industry pelletized feeds or implants have been manufactured by HME. More recently Maniruzzaman et al. [17] found, that HME has gained its importance in the health-care and pharmaceutical industry. Hot melt extruders in pharmaceutical application have to meet certain requirements regarding processing drug mixtures for different solid dosage forms and the manufacturing of wet granulation. Some of the most important differences of HME equipment in pharmaceutical application compared with applications in plastic industry are:

- The contact parts of the barrel-wall and the screw aren’t allowed to be reactive, additive or absorptive with the manufactured product
- Proper configuration for cleaning and validation related to the pharmaceutical environment is needed
- Different operating range (physical quantities)

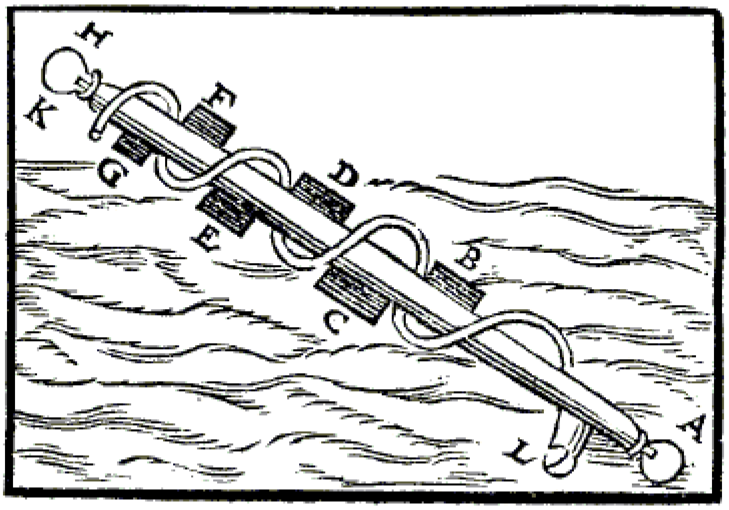

Figure 1.1.1.: The Cochlea Archimedis as the origin of the first extruder screw [2].

There are also different critical quality attributes regarding the pharmaceutical applications, described in section 1.1.7, but other than that, the setup and procedure of HME in plastic and in pharmaceutical applications are identical. In this work the pharmaceutical aspects of hot melt extrusion will be discussed. A more detailed description about HME in pharmaceutical applications can be found in section 1.1.8.

1.1.1. Hot melt extrusion process and extruder setup

HME is a complex process, where different processing zones are linked together in order to obtain the required end product. Before operating with the extruder certain rheological and thermodynamic properties and also operating parameters have to be identified. In Table 1.1.1 the most relevant setting and process parameters are listed, captured by Kohlgrüber [18].

Patil et al. [19] showed that in step one of the process, the extruder is supplied with the material to be extruded through a hopper. The configuration of the hopper provides easy feed of the raw material. The pitch and the helix angle are crucial for the output with constant screw speed. Then the solid material is conveyed to the transition zone. In the next step the process of melting, mixing, grinding, reducing particle size, venting or kneading is carried out. Particularly, there are various mixing zones for a complete modular screw designed for specific end products. Figure 1.1.2 shows a schematic illustration of the HME-process with a twin-screw configuration.

The process of melting in co-rotating TS-HME (twin-screw hot-melt extrusion) is induced by frictional heating within the barrel and additionally with heat generated by heaters attached on the barrel. The temperature of the heaters can be controlled ranging from 30°C up to 250°C. A major part of the heat is generated by shearing material between the screws and the walls of the barrel. In certain applications up to 80% of the heat required for melting or fusing the

Setting Parameters	Processing Parameters
Throughput	Torque
Screw speed	Pressure/filling degree profile
Extruder configuration (screw/barrel)	Temperature profile
Die geometry	Residence time distribution
Barrel heating	Dispersion/mixing quality
Vacuum	Plastification characteristics
Product properties	Intake characteristics
	Degassing efficiency

Table 1.1.1.: Setting and processing parameters in HME.

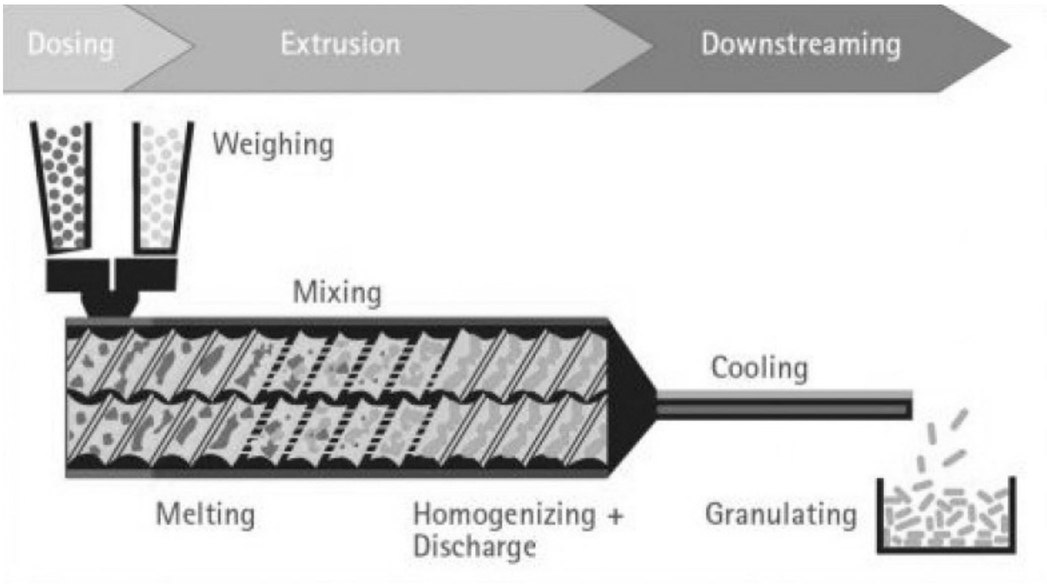
Dosing
Extrusion
Downstreaming
Weighing
Mixing
Cooling
Melting
Homogenizing +
Discharge
Granulating

Figure 1.1.2.: Schematic principles of TS-HME [3].

material is delivered by friction, while the heating elements are used for keeping the temperature of the melt in equilibrium. Considering the high shear forces and the heat generated by the heating-element mounted on the barrels, the process of melting is initiated by frictional work, stresses between the rotating screws, the screw barrel interface and the induced temperature by the heaters. Bastian et al. [20] captured that melting can be accelerated by:

- High Degree of filling
- Low melting temperatures
- Small particle size
- Low degree of crystallinity
- High melting viscosities
- Narrow kneading discs

Furthermore the results of his study showed that the melting length is dependent on the melting enthalpy of the material, the viscosity of the melt and also on the geometry and the speed of the screws. Another interesting finding showed that variations of the barrel-temperature at the plastification zone has no major impact on the melt. Melting does not only occur in the plastification zone, but also in the dispersion and discharge zones, where remaining solid particles will be melted. Residence time and also pressure may have crucial impact on some quality attributes like the impurity of the end-product, stated by Kohlgruber et al. [18]. It was also found, that proper handling and also understanding of the temperature distribution in the process of HME is a fundamental aspect to guarantee, that heat-sensitive materials are not thermally degraded by high temperatures. The sectional temperatures within the barrel are usually optimized for specific viscosity, so that the material can be transported down the barrel and also to accomplish proper mixing. There have been several experimental and simulation approaches carried out to get a deeper understanding of the hot melt extrusion process, which is detailed in section 1.2. The molten material flows in helical paths by transverse-, drag-, pressure-flow and also leakage.

After melting and mixing, the components are homogeneously discharged to generate a uniformly shaped material. Different post processing equipment can cool, cut or collect the final product. Twin-screw extruders are used for devolatilization and for melt-mixing polymers with additional materials. Single screw extruders are mainly used for melting and conveying polymers to produce uniform shaped material. In the last step, shaping the melt as it leaves the extruder-die is carried out. Patil et al. [19] and Breitenbach et al. [21] showed specific pharmaceutical applications regarding calendaring and pellet forming:

1. Calendaring: The melt is supplied to two calendar rollers to create films, flakes or sheets mainly used for packaging for pharmaceutical or medical productions. This method is also used for transthermal drug delivery systems to obtain a uniform mixture of the active pharmaceutical ingredient with a carrier.

2. Pellet forming: In order to obtain pellets, additional equipment, such as travelling shears, travelling saws and a rotating knife is needed. Usually the length of the pellets reaches from 3 up to 20 mm.

In pharmaceutical applications TSE are favoured, because of its capability to generate homogeneous and consistent mixing. There are also multi screw extruder (MSE) used, but in this work I will focus on twin screw extruders. White et al. and Crowely et al. [22, 23] stated the advantages of TSE over SSE:

- Feeding-rate
- Kneading capacity
- Dispersing capacity
- Lower heat generation
- Process efficiency
- Process flexibility
- Control of process parameters

There are also some advantages with the SSE design:

- Mechanical design
- Maintenance costs
- Overall costs

SSEs are simpler, based on a more trivial mechanical design, thus the maintenance costs and the overall costs are much lower compared to TSE. TSE and SSE are operating in different modes. The TSE is designed with a superior flexibility improving not only multiple processing function (mixing, melting, venting, cooling etc.) but also the productivity, and the process efficiency. TSE extruders work with higher operational speed, hence feeding-rates are improved. The screw configuration leads to enhanced kneading and dispersing capacity. Since cooling and heating elements in TSE are used, a precise control of the temperature profile can be achieved. In SSE heat is generated by friction between material, screw and barrel. Therefore increasing the rotating speed leads to higher temperature. This can cause degradation of heat sensitive drugs. Patil et el. [19] found, that the geometry of SSE (screw+barrel) leads to a high pressure generation and hence to agglomeration. The agglomeration causes poor mixing induced by minor shear deformation. As mention in section 1 frictional heating can lead to very high temperatures. In order to overcome problems with excessive heat stress, residence time is held short (about 2 minutes). In general the heat generation can be controlled from external sources (heaters/coolers) mounted on the barrel. In Figure 1.1.3 a Stand-alone 20mm Clamshell Segmented Twin Screw Extruder 20/40 from Brabender is shown.

Rauwendaal et al. [24] stated that the screws of a twin screw extruder are designed with multiple sections for different applications. In Figure 1.1.4 different screw elements are shown. Picture 1 and 2 illustrates the conveying elements, 3 the

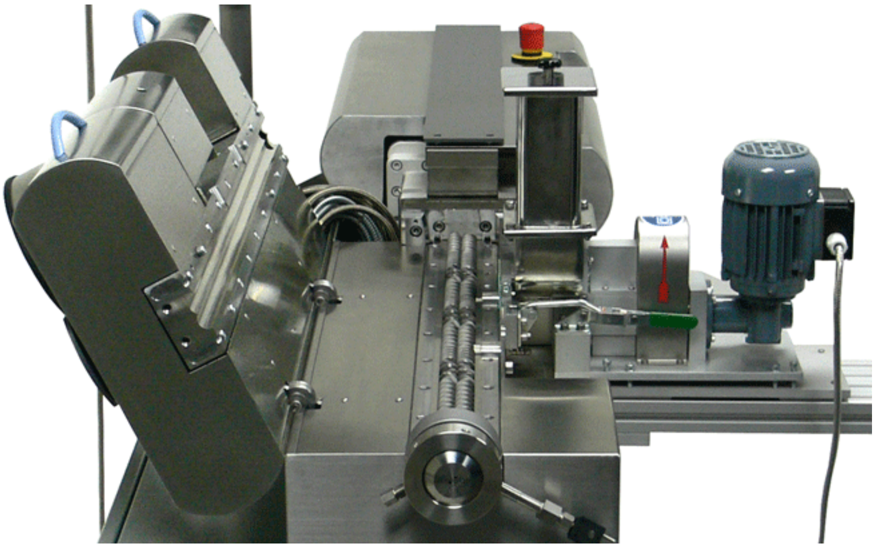

Figure 1.1.3.: Stand-alone 20mm Clamshell Segmented TSE 20/40 [4].

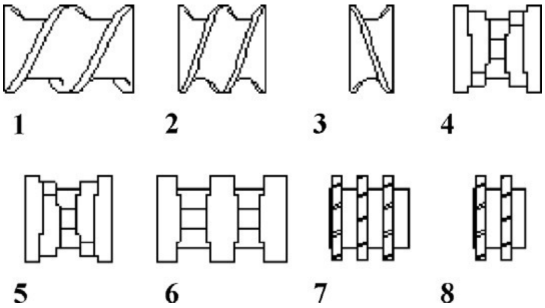

Figure 1.1.4.: A variety of the sections of a co-rotating twin-screw extruder.

back-conveying element, 4-6 the kneading elements and 7-8 the mixing elements. The use of different screw elements are designed to improve the proceedings such as mixing and pressure build-up in the extruder. The screws usually consists of surface coated stainless steel. Patil et al. [19] found, that this compound not only reduces the friction within the screws and barrel but also minimizes the tendency of chemical reactions. A more detailed description of the screw design is outside of the scope of this thesis.

With the length of the screw- to diameter of the barrel-ratio, the degree of mixing can be optimized. A usual application range of the L/D-ratio can be set from 20-60:1 mm, captured by Crowley et al. [23]. In Figure 1.1.5 a complete modular screw with different sections is shown. In Figure the processing zones of a TSE are shown.

Kohlgrüber [18] provided an overview of the tasks, setting parameters and characteristics of different processing zones of a co-rotating TSE, listed in Table 1.1.2.

Wang et al. [25] showed that rotating screws generate distributive and dispersive mixing, where dispersive mixing describes the break up of small particles and distributive mixing generates a homogeneous three-dimensional distribution of the particles. In other words, distributive mixing describes the rearrangement of

Zone	Tasks	Setting Parameters	Characteristic
Intake	Convey, Compress, Remove air	Screw speed, Throughput, Free screw volume, Pitch, Bulk density, Friction (material walls)	Intake-processes limited by the volume
Plastification Melting	Melt, Pre-dispersion,	Screw speed, Throughput, Screw geometry, Heat flux, Specific heat capacity, Heat conduction, Melt enthalpy, Particle Size	Highly influenced by screw speed and throughput
Melt Conveying	Convey	Screw speed, Throughput, Pitch, Material properties	Partially filled, fully filled back-pressure zones, Leakage-flows over screw tips, Backmixing caused by intermeshing screws, As little energy as possible applied
Distributive mixing	Distribution, Homogenization of the melt temperature	Screw speed, Throughput, Screw Geometry	Homogeneous distributed material with short mixing length and minimum energy input
Dispersive Mixing	Break down particles	Screw speed, Throughput, Screw Geometry, Viscosity	Dependent on the kinematics of the flow
Devolatilization	Remove water, residual monomers and solvents	Screw speed, Throughput, Screw volume, Vacuum	Partially filled 1.5 D pitches
Pressure build-up	Pressure build-up	Screw speed, Throughput, Pitch, Gab between screw- and barrel-element	located in discharge zone and in backward pumping screw elements (mixing-, re-conveying-, kneading-blocks), to overcome pressure generated by backward pumping elements

Table 1.1.2.: Summary of the extruder zones and the corresponding tasks, parameters and characteristics.

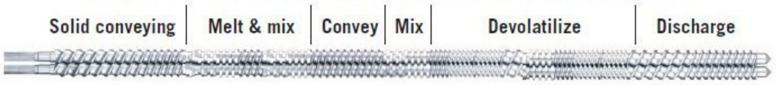

Figure 1.1.5.: Various mixing zones of an extrusion screw [5].

small particles into a homogeneous dispersion. The most important flow properties regarding distributive mixing are shear stresses and the quality of the flow. Cong et al. [26] showed that interfacial tension of the droplets/particles leads to agglomerates. In order to break the agglomerates and reduce its length scale, a certain amount of stress is needed. Some of the most important features of the mixing-modes are:

1. Distributive mixing:
    a) Maximizes division
    b) Recombines materials
    c) Minimizing energy (low extensional / planar shear effects)
    d) Uniform blending of the material
    e) No reduction of dispersed material particle size
    f) Minimal thermal/shear degradation
2. Dispersive mixing:
    a) Extensional/planar shear forces to reduce the size of the dispersed particles by breaking them up

Both methods can be utilized by using different mixing elements. This allows twin screw extruders to execute not only particle size reduction but also mixing. These effects are very important for the incorporation of dispersed or dissolved APIs into polymers. Furthermore, Martin et al. [27] stated, that twin screw extruders are separated into 2 different types: High-speed energy input (HSEI) and low-speed late fusion (LSLF) twin-screw extruders. HSEI extruders are used for compounding, devolatilization and reactive processing. LSLF twin-screw extruders are widely used to mix and pump at consistent pressure. The screws itself can be designed as co-rotating or counter-rotating, as shown in figure 1.1.6.

Patil et. al [19] found that counter rotating twin screws have some negative effects compared to the co-rotating design:

- Air entrapment
- High pressure generation
- Low maximum screw speed
- Low maximum output

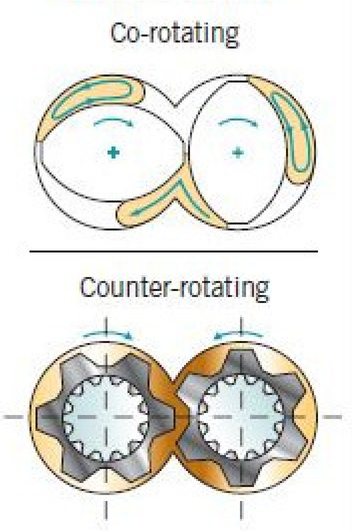

Figure 1.1.6.: End-view of intermeshing twin-screw extruder [5].

Co-rotating twin screws can furthermore be separated into inter meshing and non inter meshing designs. Crowely et al. [23] stated, that the inter meshing screws provide several advantages compared to a non inter meshing setup:

- Self-wiping high screw
- High Speed (see pharma pp of hme page 912)
- High output
- Good mixing and conveying
- No outward pushing effect

Fully intermeshing extruders are the state of the art in twin screw extruders. It also reduces the non-motion and hinders overheating of materials. To remove volatiles and for highly viscous material, a non-intermeshing design is preferred. In the case of non-intermeshing the screws are more remote than in intermeshing design, hence large volume devolatilization can be carried out, presented by Eitzlmayr et al. [1]. Kohlgrüber [18] investigated the historical development of the co-rotating twin screw and found that in the 1940s a team consisting of experts in physical, mathematical, engineering and mechanics called W. Meskat, A. Geberg and R. Erdmenger et al. [28] started detailed investigation on co-rotating extruder systems in Wolfen Germany. The team was looking for an optimal mechanical apparatus regarding high viscosity technology and therefore investigated adhesive, frictional, and antifrictional behaviours of the product with different material consistencies. Additionally they were looking for solutions to overcome rheological variations. Bayer AG continued this work and created different expert groups regarding co-rotating extruder systems. R. Erdmenger the leader of one group called “High Viscosity Technology” was specialised in chemical engineering focused on high viscosity engineering and found that the co-rotating intermeshing TS-design had advantages like self cleaning characteristic, while counter rotating screws tend to get blocked by solids and also could not provide proper mixing, so this kind of design had been discarded.

Rauwendaal [24] describes the process of devolatilization in polymer engineering as the removal of volatile components from the polymer. After the step of polymerization there might remain some “unwanted” substances, such as unreacted monomers, oligomers, toxic material or other impurities, therefore the process of devolatilization is very important in the polymer manufacturing process. The “purification” consists of 2 relatively complex processes:

1. Diffusional mass transport
2. Convective mass transport

With this work the characteristics of Newtonian as well as non-Newtonian fluid flows in the melt-conveying zone with a co-rotating double-flighted screw geometry and an inter-meshing screw design for HME will be studied. A precise representation of the other processing zones is outside of the scope of this work.

1.1.2. Descriptive features of co-rotating TS-HME

Patil et al. [19] examined the descriptive features charactierzing TS in HME. They found, that residence time is usually very short, in the range of 5-10 minutes. Furthermore screws are self-wiping, which leads to a minimized product wastage and also very little inventory is needed. Especially when working with hazardous materials, the use of minimum inventory is very beneficial. Different operating parameters can be chosen to increase the versatility and to adapt to certain applications. Materials with a wide range of viscoelasticity can be processed. Different mixing elements enable superior mixing (distributive and dispersive mixing). Temperatures reaching from 30 up to 300°C with a typical throughput of 0.5-5 gm/min can be achieved.

1.1.3. Monitoring and controlling parameters of HME

Some of the most important parameters stated by Chokshi et al. [29] are barrel temperatures, feed rate, screw speed, motor load and melt pressure. While barrel temperature, feed rate and screw speed can be controlled, motor load and melt pressure can be monitored. The fill-rate of the extruder is controlled by two parameters, these are feeding rate and screw speed. With these parameters constant shear stress and constant residence time can be achieved. Motor load and melt pressure are related to feed rate and screw speed. If these parameters are held constant motor load and melt pressure depends on molecular weight of the material and also on polymer miscibility in binary mixtures. Rauwendaal et al. [30] found that melt pressure and temperature are the most important indicators of “how well” the extruder is working. Rauwendaal compared the condition of an extruder with the health status of the human body. When a person visits a doctor with a certain problem, the first thing the doctor usually does, is to check blood pressure and body temperature. Both parameters are very significant indicators not only for the health of a human body but also for extruders.

Melt pressure measurement This parameter is not only important for process monitoring and control but also for the safety of the extrusion process. The die-head pressure is critical for the quality of the output. Here a certain pressure has to be applied to overcome the resistance within the die. The output corresponds to the die-head pressure. This also indicates the stability of the process over time. Also the pressure in the extruder has to be controlled. Pressure transducers with two diaphragms are mainly used. One is used directly in the melt, while the other one is located away from the melt with a hydraulic or push-rod connection between the diaphragms. In the process of extrusion very high pressure can arise quickly. In the worst case this can lead to a catastrophic explosion. Additionally, every extruder is equipped with an over pressure safety device to prevent accidents.

Temperature measurement For the Measurement of temperature in HME, thermocouple TC sensors or resistance temperature detectors are used. TC sensors consists of two different metals with different junctions leading to a temperature difference $T\text{-}T_0$ causing a generation of voltage related to the temperatures. The resistance thermometer (RTD-type) measures the resistance changes of metals with temperature. RTDs provide a higher output signal, superior stability and accuracy but inferior point sensing and also higher costs. In order to measure the melt temperature an immersion TC is used. For barrel temperature measurements either TC or RTD pressed into the barrel can be used. More recently infrared detectors (IR-detectors) are used for temperature measurments. Here the emitted radiation caused by changes in temperature is metered for the detection. Hence non contact measurement is possible.

Process data and critical quality attributes (CQAs) of the HME-process In pharmaceutical applications CQAs and process data are crucial for the manufacturing process. The process data in the extrusion process is monitored and also saved into a database, while CQAs are usually measured. Baronsky et al. [31] described the most important ones as follows:

- Specific mechanical energy (SME)
- Extruder load factor (ELF)
- Calculated extruder load factor (CELF)
- ELF the standard deviation of CELF
- Melt temperature (heating elements)
- Melt pressure
- Standard deviation of CELF and melt pressure

The SME is defined as amount of input power per kilogram of the manufactured material. CELF/torque is defined as the power used for the maximum motor specification. The heating elements are important for the stability of the API, the appearance of the setup and also has to be checked after each batch. The extruder output (strands) are visually controlled. Raman- and NIR-spectroscopy is used to qualify the APIs homogeneity.

Critical quality attributes (CQAs) are also crucial for the evaluation of the quality of processed material, described by Baronsky and Patil et al. [19, 31]. There are several attributes measured in order to determine the quality of the end-product such as:

- Appearance content
- Uniformity dissolution
- Viscosity
- Cores resistance to crushing
- Resistance to crush
- Purity
- Degradation products (aldehyde, water content)
- Taste/Flavour

Baronsky et al. [31] also found, that additional factors such as feed rate, screw speed and the concentration of the API influence the critical quality attributes of the product. For the qualification of the degradation of the API, the SME and temperature at the die are necessary data points. The degradation should be as low as possible while the feed rate and the revolution speed should be held high. With these parameters a predetermination of cost and efficiency of the manufacturing process can be achieved. Screw speed, processing temperature and feeding rate are adjustable parameters affecting the mean residence time and the shear stress. The main disadvantages of the HME-technology are difficulties related to high energy input, shear forces and temperature condition. In order to overcome the problems like temperature depended degradation and to get a better understanding of the complex processes in HME-technology, investigation of the temperature distribution in HME is carried out by in work.

1.1.4. Pharmaceutical applications of HME

In this section, the most relevant and latest developments regarding HME in the field of pharmacy will be described. Lang and Crowley et al. [23, 32] found that the process of HME can be used to produce medical devices and develop molecular dispersion of active pharmaceutical ingredients (APIs) mixed with polymers to improve different properties of the end product (drug). HME-technology can also be used to produce delivery systems with defined amount of active ingredients in micrometer range for specific applications. Markl et. al [33] stated, that the active pharmaceutical ingredient dissolved into a polymer matrix, also called a carrier, leads to advanced features of the compound, such as:

- Thermal binder
- API stabilizer
- API solubilizer
- API release control

Additional by the procedure of HME has certain advantages compared to conventional pharmaceutical manufacturing techniques listed by Maniruzzaman et al. [34].

- Bioavailability (sustained, modified and targeted drug delivery)
- Solubility
- Solvent-free non-ambient mechanism
- Reduced manufacturing time Continuous, altered (modified), targeted release
- Homogeneity in extrudates
- Consistent dispersion
- PH-Stability
- Prepare precursors for thermoplastic drug eluting devices
- Taste masking of bitter active pharmaceutical
- Different screw geometries for different applications
- Fast
- Scale up possibility
- etc.

Nevertheless, HME has some drawbacks as well including:

- Thermal drug/polymer stability
- High flow properties
- Substrate required
- Negative effects with high heat sensitive molecules such as proteins

Considering the capabilities of HME in pharmaceutical research a wide range of products such as granules, pellets, modified release tablets like enteric matrix tablets up to implantable reservoir devices have been developed already, stated by Maniruzzaman et al. [34]. To cite some examples nifedipinie, nimodipine and itraconazole have been manufactured as solid dispersion. Moreover, Miller et al. [35] have shown the ability of aggregating fine particles to enhance breakup rate properties. This improvement could be realized by enhancing the wettability of the particles. Another investigation of Verreck et al. [36] could demonstrate the reduction of processing temperature without any disadvantages by using supercritical carbon dioxide (scCO2) as a provisional plasticizer during the production of ethylcellulose with HME. Porosity and hygroscopicity could also be improved and the application with scCO2 led to an increase of the surface area.

Solid dispersions for solubility and bioavailability enhancement Patil et al. [19] collected some important pharmaceutical applications of HME. A solid dispersion usually consists of at least two different components. The crystalline or amorphous hydrophilic matrix and a hydrophobic drug which can be dispersed either in amorphous or crystalline particles. Aqueous media will dissolve the carrier and the drug can be released as colloidal particles. With HME, APIs can change the crystalline form into a well-water-soluble amorphous form, increasing the solubility. Another advantage is the fact that the HME-method does not need a solvent for the formation of solid dispersion. Hence, stability risks of the solvent appearing during formulation is excluded from the process. Wang et al. [37] studied the improvement of the bioavailabilty of Ginkgo biloba extract (GBE-SD) solid-dispersion produced with HME. In vivo experiments showed that GBE-SD released 93% of the drug within 20 min while dissolution of GBE without solid dispersion takes 2h to release 30% of the drug. Several studies give evidence that HME is a very eligible technique for the formation of solid dispersion and also improves the bioavailability of the manufacture.

Microencapsulation Patil et al. [19]found that microencapsulation plays a very important role in the transport process of materials, especially when the systemic environment is varying. Here small portions of solids or fluids are immobilized by encapsulating them. It has been found that HME is a very suitable technique for the production of encapsulates to guarantee a “safe” transport of an enclosed drug to specific regions of the body. This procedure not only improves the targeted release of the API but also ensures the transport process including proper degradation and reduces costs of production. Additionally, the absence of solvents plays a very beneficial role.

Targeted drug delivery HME can improve selectivity and specificity regarding the target tissue and hence ensure proper drug delivery. Bruce et al. [38] produced HME tablets of 5-aminosalicylic acid (5-ASA) with Eudragit S 100 as a carrier and added two plasticizers, triethyl citrate (TEC) and citric acid. He could show that TEC decreased the process temperature t_p, hence led to less degradation with the plasticisers present. The approach of sustained drug release is based on defined and targeted drug release rate, time and location. The sustained-release preparations generated by the HME technique also guarantees specific and constant concentration resulting in lower side effects. Verhoeven et al. [39] created sustained-release mini matrices with HME. He used metoprolol tartrate (MPT) as the drug, ethyl cellulose as the sustained release polymer, dibutyl sebacate as the plasticizer and xanthan gum as the hydrophilic polymer resulting in a smooth and homogeneous end product. Additionally, he could show that the drug distribution was homogeneous within the matrices.

Taste masking Another problem to overcome is the bitter taste of several active ingredients used for pharmaceutical products. There are 2 different approaches described by Remington et al. [40]:

1. Reducing the solubility of the product in the saliva, in order to prevent the molecules to interact with the taste buds. This is achieved by changing the drug from its amorphous into a crystalline state.
2. Another solution suggests an alternation of the interplay between drug and the receptors.

With HME a method has been developed, where the manufacturing process includes a solid dispersion coupled with a taste-masking polymer. The dispersion hinders the interaction of the bitter drug-substance with the receptors, by stopping the release of the substance into the saliva. This is accomplished with hydrogen bonding between the drug-substance and the solid dispersion (polymer matrix).

Films Films can be used as a drug delivery system or applied onto wounds in order to achieve a healing effect. Solvent-casting technique with HME is the state-of-the-art technique for the production of films. Palem et al. [41] used HME to create bioadhesive domperidone buccal immediate release films including PEO N100 alone or with HPMC E5 and LV or Eudragit RL Po as polymer matrix. The films appeared smooth, without cracks. The manufacture had consistent thickness of about 810 to 850 μm with a drug load from 86.5 up to 99.2 %. The end product also passed the requirements of a buccal film.

Implants Several studies have approved that HME technology is very efficient for preparing an implantable medical device. Versatility, advantages and the critical factors related to the HME process have been reported. A PhD thesis carried out by Ghalanbor [42] show that implants based on protein (hen egg white lysozyme)/PLGA formulations can be produced by HME. He could also prove the stability of the protein by high performance chromatography (HPLC), DSC, FTIR and the biological activity after the extrusion process. Additionally, the in-vitro release of the protein remained from 60 to 80 days. Another study by Li et al. [43] could show that HME is a very promising technique to produce implants as local delivery systems. The in vivo release of dexamethasone was about 50% per month and the degradation showed a loss in weight of 25% per month. Additionally no negative sideffects could be found. These findings imply that HME is an great technique for the production of biodegradable implants and delivery-systems.

Nanotechnology Applying nanotechnology on HME-technique to create drug delivery systems show some important advantages:

1. bioavailability
2. drug presence (increase half-life for clearance)
3. drug delivery
4. Incorporation of hydrophilic and hydrophobic APIs
5. carrier capacity
6. Lower processing time
7. Reduction in product cost
8. etc.

There are plenty of studies emphasising the advantages of nanotechnology in HME-process. Baumgartner et al. [44] developed a one-step nano-extruder for the production of nanoparticle formulations. This was accomplished by feeding the nano-suspension into the hopper of the extruder. Afterwards the solvent was eliminated by devolatilization. Phenytoin was used as the drug and Soluplus as the polymer. He could show a crucial improvement of the solubility and also increased dissolution rate. The enhanced effective particle surface allowed a full release of the drug within 5 minutes.

Continuous manufacturing process Tablets are the most used solid dosage form nowadays. In order to guarantee a homogeneous distribution of the ingredients, wet granulation has been the method of choice. High shear- or fluid bed granulation technique has bee used. In order to improve the traditional "batch-process", researchers have been looking for alternatives, especially with the aim to create a continuous manufacturing process. Continuous manufacturing uses the so called "one-in one-out" method resulting in superior production capacity, lower costs, faster production, smaller working space, superior scale-up possibilities and production quality, collected by Almeida and Van Melkebeke et al. [45,46]. Hence studies on the incorporation of the continuous HME-technique with wet granulations process have been carried out. Several studies showed the advantages of the continuous process. Ghebre Sellassie et al. [47] developed a patent regarding this matter. More recently Mu et al. [48] studied the hot melt granulation process for high-shear mixers and fluidized bed. The hot melt granulation process generates an enlargement of the particles with molten binders such as polyethylene glycols. Therefore the TSE generated the granules and two PEGs had been used as binders at processing temperatures ranging from 80°C up to 120°C. Several parameters such as screw design, binder attributes and temperatures had been investigated. It was found that hot melt granulation characterized for high shear mixers and fluidized beds can be used properly for extrusion in order to generate a continuous manufacturing process.

Scale-up Since HME is a continuous process, it can not only reduce production time and cost but also improve the possibility of scale up solutions compared to conventional batch-processing. In fact, the scale-up process is very critical in pharmaceutical application, found by Potente and Guns et al. [49, 50]. There have been major problems regarding drug production delays, especially while introducing them on the market and hence generating millions of losses of the industry. In order to perform a proper scale-up in HME, an accurate replication of certain parameters are necessary, stated by Dreiblatt et al. [51]:

- Batch-size
- Feed rate
- Extruder geometry

In order to verify the correct scale up, melt- temperature/viscosity, mechanical behaviour of the die and the melt-distribution in the extruder are necessary parameters. A well working scale up mechanism requires a complete knowledge of the complex proceedings in the hot melt extrusion process. This has yet to be accomplished.

1.1.5. Materials used in HME

Rauwendaal [24] listed the most important polymer properties used in extrusion. Acrylonitrile butadiene styrene (ABS), polyvinyl chloride (PVC), polystyrene (PS) and linear low-density polyethylene (LLDPE) are some polymers used in HME. This data can be found at CAMPUS (Computer Aided Material Preselection by Uniform Standards), a material database for polymers:

Polymer	k [J/ms°C]	C_p [J/g°C]	ρ[g/cm^3]	T_g[°C]	T_{mp}[°C]	n [-]	$d\eta/\eta dT[°C^{-1}]$
ABS	0.25	1.40	1.02	115	-	0.25	0.20
PVC	0.21	1.10	1.40	80	-	0.30	0.20
PS	0.12	1.20	1.06	101	-	0.30	0.08
LLDPE	0.24	2.30	0.92	-120/-90	125	0.60	0.02

Table 1.1.3.: Properties of some generic Polymers.

Crowely et al. [23] listed different material parameter regarding the temperature-range in HME. In Table 1.1.4 some carriers for the preparation of HME dosage forms, and in Table 1.1.5 a variety of drug substances for the proceedings in HME are listed.

Since the lowest working temperature regarding different polymers/drugs in HME must be found, in order to prevent degradation or extrusion defects, glass transition temperature and melting temperatures values can be used to choose the processing temperature correctly.

Name (chemical)	Trade name	Glass Transition temperature tg (°C)	Melting Temperature tm (°C)	Reference
Ammonio methacrylate copolymer	Eudragit ® RS/RL	64	-	Follonier, N. et al., 1994; Kidokoro et al., 2001; Zhu et al., 2002
Cellulose acetate butyrate	CAB 381-0.5	125	157	Follonier, N. et al., 1994; Follonier et al., 1995; Sprockel
Poly(ethylene-co-vinyl acetate)	Elvax ® 40W	–36	45	Follonier, N. et al., 1994; Van Laarhoven, J. A. H. et al., 2002
Poly(ethylene glycol)	Carbowax ®	–20	37–63	Cuff et al., 1998; Forster et al., 2001c; Hamaura et al., 1999

Table 1.1.4.: Temperature-range for different materials used in HME.

Drug	Melting Temperature tm (°C)	Reference
Nifedipine	175	Forster et al., 2001a, 2001c; Nakamichi et al., 2002
Ibuprofen	76	De Brabander et al., 2002, 2000; Kidokoro et al., 2001
Acetylsalicylic Acid	135	Stepto, 1997; Stepto, 2000
5-Aminosalicylic acid	280	L. Diane Bruce, 2005

Table 1.1.5.: Melting temperature of a set of drugs.

1.1.6. Marketed products

In Table 1.1.6 products manufactured by HME for pharmaceutical application including indication, purpose and the the responsible company, stated by DiNunzio [52] are listed.

Product	Indication	HME purpose	Company
Lacrisert (Opthalmic Insert)	Dry eye syndrome	Shaped system	Merck
ZoladexTM (Goserelin Acetate Injectable Implant)	Prostate cancer	Shaped system	AstraZeneca
Gris-PEG (Griseofulvin)	Anti-fungal	Crystalline dispersion	Pedinol Pharmacal Inc.
Norvir (Ritonavir)	Anti-viral (HIV)	Amorphous dispersion	Abbott Laboratories
Eucreas (Vildagliptin/Metformin HCI)	Diabetes	Melt granulation	Novartis
Zithromax (Azythromycin enteric-coated muliparticulates)	Anti-biotic	Melt congeal	Pfizer
Fenoglide TM (Fenofibrate)	Dyslipidemia	MeltDose (solid disperion)	Life Cycle Pharma

Table 1.1.6.: Products manufactured by HME.

1.2. Overview & advantages of SPH in HME

1.2.1. Experimental approach

One major problem of understanding the HME-process is the limited access of usable data from experimental measurements. Eccher, Valentinotti and Mohr et al. [53, 54] used streak photography to examine the flow behaviour and the velocity profile in extrusion. They used a stationary screw with a rotating transparent barrel. Measurements were carried out at very low rotation speeds, which are not realistic for large extruders. Choo et al. [55] used a deep-channel single-screw extruder with perspex windows to have better insight on the velocity profiles. He used a glucose solution, a Newtonian fluid, and tracers in order to take streak photographs of the tracers from two perpendicular directions at the same time. They found out that it was very difficult to get proper data near the screw root because of the limited optical access. Also experimental measurement with perspex at high temperatures is not usable due to the degradation of the perspex at high temperature. McCarthy et al. [56] used nuclear magnetic resonance imaging (NMR) to monitor the motion of magnetically marked tracers. This measurement-technique showed the same results as predicted in theory. The fluid velocity varied linearly between the barrel wall and the screw surface. Chandrasekaran, Karwe and Sernis et al. [57, 58] used a laser Doppler anemometer (LDA) to measure the velocity in a co-rotating twin screw extruder through perspex windows. This method also showed good results but it is not usable for extrusion working at high temperature.

Capillary or rotational viscometers are tools to measure viscosity. Therefore slit die viscometers (SVD) have been designed and tested extensively. SVD can continuously measure in-line rheological data while using an experimental setup presenting a realistic extrusion process. It was found that understanding of the complex proceedings in heat transfer relating to the melt temperature is difficult to carry out. Another approach of temperature measurements in HME carried out by Nietsch et al. [59], had been accomplished with an infrared-thermometer. Nietsch was able to capture temperature differences of a black polyethylene melt performed by changes of the concentration of black traced PE particles. He could show that:

- Melt temperature decreases to a minimum and then increases again (time-dependent)
- The increment is related to the shear heating during the flow

The sensor design and experimental setup developed by Wood et al [60] has been followed up by Sombatsompop et al. [61] and consists of an interconnected series of thermocouples. Hereof 2-D temperature profiles of PE (polyethylene) with respect to the flowing melt and screw rotating speed in HME was carried out, leading to some interesting findings such as:

- Close relation between flow pattern and temperature profile
- The melt temperature increases with the screw rotating speed
- High melt temperature at the centre with low speed
- Uniform melt temperature across the flow channel with increasing speed
- Melt temperature is related to shear heating, heat-conduction effects and the flow length of the melt
- Experimental temperature results do not match theoretical predictions

Although the experimental setup revealed fundamental information of the processes in HME, this knowledge is not sufficient to completely understand the complex behaviour of the fluid flow and the temperature distribution.

Slit die/torque rheometer combined with a co rotating twin screw extruder had been used to measure pressure drop and torque stated by Pöyry et al. [62]. It was found that it is a difficult task to gain meaningful results with this experimental setup. The high costs are also a limiting factor in experimental observation in twin-screw extrusion.

Considering the complexity of different approaches, problems related to the experimental setup, the associated financial effort and the limited information gained, scientist have been looking for a different approach on measuring crucial properties in the extrusion process.

A promising method of understanding the processes in HME is carried out by using computer based simulations. There are 1-D and 3-D Simulations carried out, regarding this matter. While the less expensive one-dimensional approach provides a rough description by considering the distribution along the axis but neglecting the mathematical description in radial and azimuthal directions, the three-dimensional simulations could provide the complexity of flow and mixing phenomena related to the interplay of the extruder geometry, material properties and process conditions in hot melt extrusion. This also could lead to valid scale-up approaches. Nevertheless, no fully-resolved first-principles simulations of this type have been accomplished yet.

1.2.2. 1D simulations

A 1-D simulation study carried out by Eitzlmayr et al. [1] showed that the 1-D approach is less expensive, because the flow at the screw elements is not fully resolved and not all spatial directions are considered for the simulation. The simplified first principle model can calculate different properties such as flow rate or axial pressure with consideration of realistic influence of the screw geometry. This approach is based on integral properties of the flow field. For different screw-sections or screw-geometries parameters can be extracted from analytic equations or experimental data and fully resolved simulations. In order to receive correct data, averaging over the cross section has to be considered, hence spatial properties like material dependent viscosity is required. By now 1-D simulations represent a simplified method of realistic processes, hence provides adequate information to improve insight on specific problems and therefore drastically reduces the experimental effort. A 1-D approach is also the only way of simulating the complete extrusion process because of it's affordable computational expense.

1.2.3. 3D simulations

Eitzlmayr et. al . [1] stated, that for 3-D simulations, primarily mesh-based CFD (computational fluid dynamics) such as FVM (finite volume method), FEM (Finite element) and FDM (Finite discrete models) have been preferred. All three methods are systematic numerical methods to solve PDEs (partial differential equations) which describe the physics of interest. The main difference of the methods are the ease of implementation, which can be very complicated for certain problems. Fundamentals of CFD can be read in [63] written by Chung.

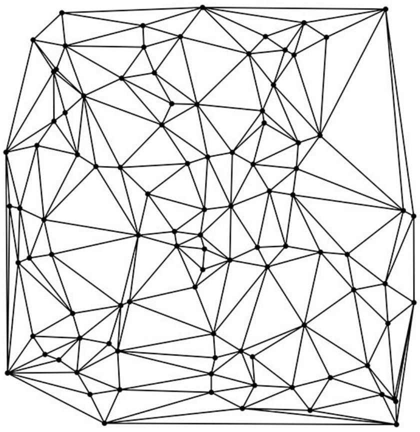

Figure 1.2.1.: Triangulations to build the mesh [6].

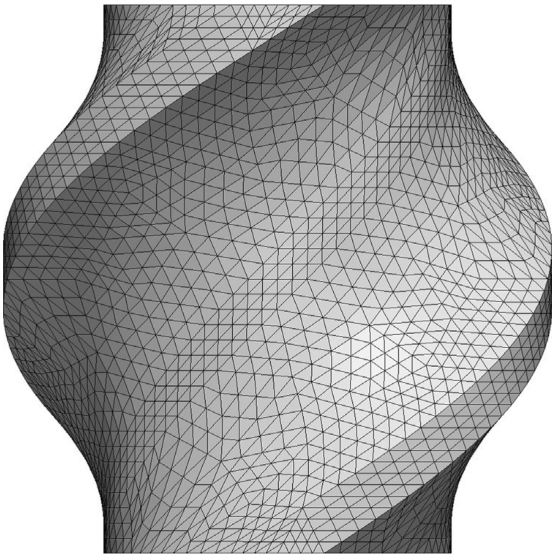

Figure 1.2.2.: Mesh of the conveying element of a screw.

Bjorn et al. [6] stated that FEM is designed for structural analysis like heat transfer, chemical engineering, CFD, or electromagnetics while FDM is preferred in weather calculations or astrophysics. FVM is mainly used in CFD, heat transfer or chemical engineering. The very basic principle of FEM/FVM/FDM considers a body with a finite number of element or volumes which describe a distribution or a field variable. The body, a 1, 2 or 3-D solid can be divided into smaller parts (elements). A finite number of elements define the object. The proceedings of the whole body can be described by a set of elements. These elements are connected with interconnected joints, so-called nodes. Consequently a meshed object with a grid is created. Certain field variable can be described as a body containing a set of partial differential equation for each element presented at [64]. In Figure 1.2.1 the triangulations to construct a mesh is illustrated. In Figure 1.2.2 a complete mesh of the conveying element which will be used as one of the elements for the simulations carried out by this thesis is shown. Apart from the conveying screw elements, a barrel and also a back and a front element had been constructed.

Based on the number of elements the FEM is getting more accurate by increasing them. FEM is a very robust numeric simulation tool to describe physical processes such as heat conduction or dynamic effects on solids. FEM was not only used to describe flow behaviour in co-rotating twin-screw extruder but also to simulate wall slip phenomena. However working with FEM has some major problems for certain simulation applications stated by Chajecadvances et al. [65]:

- Free surface
- Deformable boundary
- Moving interface
- Very large deformation
- Crack propagation
- Partially filled objects
- Extremely thin structures

Additionally some issues related to computational fluid dynamic simulations in hot melt extrusion can be found:

- Free-surface flows in partially filled sections
- Flow behaviour is very complex
- Non-Newtonian
- Non-isothermal behaviour of the extruder (linking between mass, momentum and energy balances)
- Very small gaps between screws and barrel (highly resolved flow is needed)
- Transition from granular to molten state is currently impossible (fully resolved simulation)

In order to overcome problems related to the drawbacks of FEM, SPH (smoothed particle hydrodynamics) is a very promising simulation approach, stated by Hofler and Speith et al. [66, 67]. SPH represents a mesh-less alternative to conventional methods in CFD. This method was originally developed for astrophysics to calculate cosmological and astrophysical phenomena such as galaxy formation, stellar collision or supernovas with reasonable mathematical effort stated by Lucy, Gingold and Monaghan et al. [68, 69]. The difficulty with this type of simulations is the high computational expense. For mesh based methods the expansion of the simulation region has to be know a priori in order to guarantee a gapless/-complete discretisation. The relative scale of length of effects in this kind of simulations and the related expanse of material are ranging over several orders of magnitude, causing extreme increase of mesh cells/elements. Whereas SPH is based on a Lagrangian approach of continuum mechanic conservation laws it can handle this kind of application. The sampling points are moved while calculating in the simulation region. The calculation of properties for the fluid at each sampling point is carried out with an interpolation of a smoothing function over neighbour sampling/mass points. As the sampling/mass points are moving with the velocity field neither empty spaces have to be discretised nor knowledge of the final expansion of the simulation is required a priori. These so-called “particles” represent the material or fluid. The fundamental mathematical principle transfers a system of partial differential equations into a system of ordinary differential equations. A detailed mathematical description of the fundamental equations in SPH can be read in Chapter 2.

After introducing SPH in astrophysics, this method is getting more and more popular in a variety of technical applications. In certain areas such as implementing boundary conditions, evaporation models, description of surface tension, simulations of multiphase flow and multicomponent substances, SPH is still in development stage. Due to the nature of SPH, it is a promising modeling approach which can provide deeper understanding in the of hot melt extrusion process. SPH can handle 3-D simulations in complex geometries like rotating twin screws and deliver related effects on fluid flow properties.

SPH can offer certain advantages relating to the simulation of twin-screw extruder in hot melt extrusion, listed by Eitzlmayr et al. [11]:

- The complex rotation in extrusion and the intermeshing screw geometry can be calculated
- Simulation of partially filled and full elements
- Non-Newtonian material properties
- Analysis of throughput, power loss and mixing can be carried out
- Free surface flows
- Mesh free
- Tracking of tracer particles

1.2.4. Simulation studies

Zhou et al. [70] investigated the temperature evolution during an extrusion process of 7075 aluminium alloy at various ram speeds, using FEM as a modeling approach based on analytical and semi-analytical methods. The initial temperature of the billet was 450°C in order to benchmark the maximum temperature regarding homogenised and fast cooled billet, without applying high pressure. Nevertheless the maximum temperature rise in this deforming material ranges from 35°C to 100°C. The tooling temperature was set at 400°C in order to consider heat loss. Temperature inside the barrel reached from 21°C- 40°C. Zhou could show that the temperature distribution in extrusion depends on different effects. Heat is generated due to deformation, friction and shear stresses. Temperature loss is caused by heat loss of the tooling such as container, stem, die and also to the ambient surrounding. Additionally he was able to simulate heat conduction between billet and extrudate.

Another study carried out by Liang et al [71] dealt with the simulation of extrusion of AZ31 magnesium alloy with oil-based graphite lubricant. Hence stress-strain, friction and heat transfer parameters had been obtained with FEM. After simulating the process the results had been compared with a 2-D simulation (DEFORM-2D). He found that oil-based graphite reduces not only the extrusion load but also the temperature of the billet. Furthermore he could show that the billet temperature is influenced by several parameters:

- Extrusion process
- Initial billet temperature
- Friction
- Extrusion speed

Li et al. [72] realised a simulation of the extrusion process of Ti-6Al-4V (Alpha/-Beta Titanium Alloy) used in aerospace specification metals with FEM. Billet temperatures for the extrusion process with steel or Ti alloys reach 900-1000°C. Deformation process caused by temperature near the β transus are very hard to examine experimentally, not only because of high temperatures but also caused by considerable strain and temperature variations throughout the compound. He found that heat generation is caused by deformation. At the beginning of the extrusion process a significant increase of temperature could be found until the temperature profile reached a more or less steady state. Maximum local temperature rise had been found at the die-billet interface (over 160°C). As a consequence of the temperature rise an expanding deformation had been observed, while the effective stress within the deformation decreased during the extrusion process. The results of the simulation are close to the findings in experimental approaches.

Altınkaynak et al. [73] studied the ongoing of the melt process within the compression section of a SSE using full 3-D simulation as a modeling approach. Therefore an investigation of the Maddock-melting mechanism in simulations such as experiments have been carried out. At the entrance of the screw channel a constant flow rate was initiated leading to interesting results:

- Screw/barrel temperature have low effect on the melt-profile
- Screw/barrel temperature have significant effect on the pressure-profile (along the channel)
- Flow rate has significant effect on the melt-profile
- With zero-traction the screw temperature increases with the flow rate

Another 2-D simulation carried out by Liang et al. [74] was dealing with the investigation of the melt process in co-rotating TSE. The simulation resulted in findings such as:

- Hot melt flow influences the melting process

- Viscous dissipation contributes to the total energy required for the melt-process. (10-30%)
- Screw speed influences viscous dissipation
- Negligible influence of the heat flux of barrel-element on viscous dissipation

Chiruvella et al. [75] numerically simulated the extrusion process in SSE for materials used in extrusion cooking. More specifically, he investigated the conversion of starch. As a modeling approach he used FDM applying initial data from experimental observation. It was found that:

- 28% of conversion caused by viscous dissipation
- 61% of conversion if the barrel temperature is 25°C higher then the temperature of the die
- Smaller die diameter causes higher conversion
- Higher compression ratio at the screws leads to higher temperature and higher conversion
- Higher compression decreases the residence time leading to lower conversion
- Lower flow rates lead to high conversion

Eleni et al. [76] numerically simulated axisymmetric and plane extrusion jet-flows. They assumed the fluid to be Newtonian and homogeneous compressible. With this study he could solve swell flow in the extrusion-process and the effect of compressibility and slip. He also found that:

- High compressibility increased the expansion of the jet
- High compressibility increased the angle of separation of the jet
- Enhanced compressibility initially reduces the swelling of the jet
- For non-zero Reynolds-numbers the compressibility leads to a contraction after the expansion of the yet
- For high Reynold-numbers oscillation in the free surface profiles occur, disintegrating downstream

Zhu et al. [7] studied mixing and energy balance in TSE with FLUENT as a modeling approach. The effect of rotation speed, geometry of the screw and initial conversion in fully filled conveying elements of co-rotating TSE on the polymerization of ε-caprolactone was carried out. In Figure 1.2.3 a flow diagram of the factors affecting the polymerization in the conveying screw element are shown. Polymerisation in this case can be described as the energy balance during the reaction.

He could show that the complex polymerization kinetics are significantly influenced by several factors, such as: mixing intensity, heat transfer (barrel surface), viscous dissipation and heat generated from the reaction. He also found that:

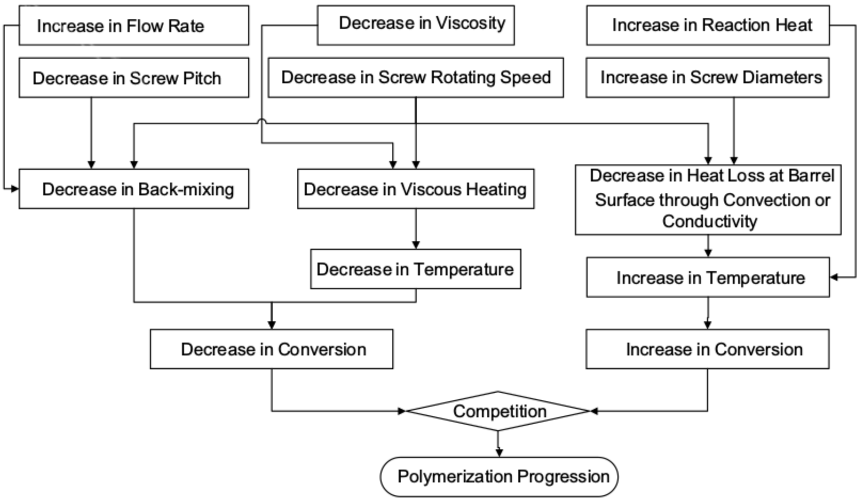
Increase in Flow Rate
Decrease in Viscosity
Increase in Reaction Heat
Decrease in Screw Pitch
Decrease in Screw Rotating Speed
Increase in Screw Diameters
Decrease in Back-mixing
Decrease in Viscous Heating
Decrease in Heat Loss at Barrel Surface through Convection or Conductivity
Decrease in Temperature
Increase in Temperature
Decrease in Conversion
Increase in Conversion
Competition
Polymerization Progression

Figure 1.2.3.: Factors affecting the polymerization in TSE with FLUENT [7].

- At low viscosity (conversion = 0) viscous dissipation is negligible for the energy balance
- Heat from reaction is a crucial factor for the energy balance
- Lower screw speed leads to heat loss at the surface (barrel), hence catalysing the reaction
- For high viscosity, viscous dissipation is crucial for energy generation
- Viscous dissipation decreases with lower screw speed leading to slower reaction

More recently Eitzlmayr et al. [1] introduced SPH as a modeling approach for HME. A Newtonian fluid with temperature independence had been assumed. The simulation was carried out for a completely and partially filled conveying screw element of a TSE. The results were in agreement with analytic solutions. Also the SPH-model regarding the conveying element of TSE accorded to FVM-results from the literature. Dimensionless results had been found robust regarding viscosity, screw speed and resolution. Another study carried out by Eitzlmayr et al. [77] with the purpose of investigation mixing in the conveying element in co-rotationg TSE showed the importance of residence time regarding mixing rates per screw revolution. Furthermore it was found, that:

- Increased residence time leads to better mixing performance in fully filled screw section
- Lower flow rates induce superior mixing-performance
- Better mixing caused by increasing the residence time also leads to higher specific mechanical energy

Based on the work of Eitzlmayer et al. [11,78] and Kondor [10] models regarding the temperature and viscosity distribution for incompressible Newtonian and non-Newtonian fluids will be studied, implemented into XPS and validated, in order to prove that SPH can be used as a scientific tool to simulate the fluid dynamics in complex geometries like twin screw extruders. Extended particle system (XPS) is a particle simulation framework which can simulate fluid flows with SPH as an simulation method. Detailed information about XPS and CFD-DEM coupling can be read at [79], presented by Dalibor and Eva et al.. In order to overcome problems related to the stated reasons in HME and also to gain more detailed information in the melt behaviour and the flow characteristics in the HME-process of co-rotating twin screw extruders, SPH represents a very promising modeling approach for incompressible and weakly compressible fluid flows.

2

Chapter 2.

Modeling approach

2.1. Thermodynamics and fluid modeling

In this chapter the most relevant fluid flow models, rheological parameters and governing equations related to hot-melt extrusion will be discussed.

2.1.1. Governing equations

The equation of continuity A quantity (mass, energy, momentum etc.) is conserved and can neither be created nor destroyed.

$$\frac{\partial \rho}{\partial t} + (\nabla \rho \boldsymbol{v}) = 0 \tag{2.1.1}$$

where ∇ is the divergence, ρ the amount of quantity q per unit volume, $\boldsymbol{v}$ the flux of q and t the time

The equation of momentum, general Naiver Stokes The foundation of the Naiver Stokes equation are the basic principles of continuity of mass, momentum and energy. The Navier–Stokes equations are based on the assumption that the fluid, at the scale of interest, is a continuum, in other words is not made up of discrete particles but rather a continuous substance.

The NS-equation is a continuation of Newton's second law ($F = ma$). Stokes included four components, the acceleration-, advection/convection-, pressure-, diffusion-term and external forces such as gravity.

$$\rho \left[\frac{\partial \boldsymbol{v}}{\partial t} + (\boldsymbol{v} \cdot \nabla)\, \boldsymbol{v}\right] = -\nabla p + \nabla \cdot (\mu \nabla \boldsymbol{v}) + \mathbf{f} \tag{2.1.2}$$

$$\rho\, (\nabla \cdot \boldsymbol{v}) = 0 \tag{2.1.3}$$

where

$$(\boldsymbol{v} \cdot \nabla)\, \boldsymbol{v} \equiv \left[v_x \frac{\partial v_x}{\partial x}, v_y \frac{\partial v_y}{\partial y}, v_z \frac{\partial v_z}{\partial z}\right] \tag{2.1.4}$$

$$\nabla p \equiv \left[\frac{\partial p}{\partial x}, \frac{\partial p}{\partial y}, \frac{\partial p}{\partial z}\right],\ p = k\,(p - p_0) \tag{2.1.5}$$

$$\nabla^2 \boldsymbol{v} \equiv \left[\nabla^2 v_x, \nabla^2 v_y, \nabla^2 v_z\right]^T ; \nabla^2 v \equiv \frac{\partial^2 v_x}{\partial x^2} + \frac{\partial^2 v_x}{\partial y^2} + \frac{\partial^2 v_x}{\partial z^2} \tag{2.1.6}$$

where a body force $\mathbf{f}$ can be ρg, with ρ as the density and g as the gravity, ∇p as pressure, the velocity $\mathbf{v}$, μ called the viscosity, the rest density or density at equilibrium p_0 and a constant k. $\frac{\partial \boldsymbol{v}}{\partial \mathrm{t}} + \boldsymbol{v} \cdot \nabla \boldsymbol{v}$ is defined as the acceleration term with v as the velocity. If in a local area the density is higher then the rest density positive pressure will occur. If the density is lower then the rest density, negative pressure and hence suction will occur. Fluids flow from high pressure to low pressure. Another necessary assumption is that all the quantities of interest like pressure, flow velocity, density, and temperature are differentiable.

The heat equation With constant pressure the energy equation for incompressible flows is decoupled from the continuity and momentum equations and can be written as:

$$\rho c_p \left(\frac{\partial T}{\partial t} + (\boldsymbol{v} \cdot \nabla) T \right) = k \nabla^2 T + \phi \tag{2.1.7}$$

The dissipation function for Newtonian fluids In order to derive the energy equation constant density for incompressible flows is considered. Furthermore enthalpy and internal energy is related to temperature: $dh = c_p dT$ and $de = c_v dT$. The dissipation function ϕ captures the conversion of internal energy emerged by work done against viscous forces. For Newtonian fluids constant μ, c_v, k, ρ are assumed and for non-Newtonian constant c_v, k, ρ

$$\phi = \left(\bar{\bar{\boldsymbol{\tau}}} \cdot \nabla \right) \boldsymbol{v} \tag{2.1.8}$$

with $\boldsymbol{v}$ as velocity vector, $\bar{\bar{\boldsymbol{\tau}}}$ as viscosity stress tensor and c_p as specific heat . ϕ has to be $\geq$0. Forϕ greater then 0 heat generation will occur. For Cartesian coordinates the dissipation function can be written as:

$$\begin{aligned} \phi = \mu \Bigg(& 2 \left[\left(\tfrac{\partial u}{\partial x}\right)^2 + \left(\tfrac{\partial v}{\partial y}\right)^2 + \left(\tfrac{\partial w}{\partial z}\right)^2 \right] + \left(\tfrac{\partial u}{\partial y} + \tfrac{\partial v}{\partial x} \right)^2 + \\ & \left(\tfrac{\partial u}{\partial z} + \tfrac{\partial w}{\partial x} \right)^2 + \left(\tfrac{\partial v}{\partial z} + \tfrac{\partial w}{\partial y} \right)^2 - \tfrac{2}{3} \mu \left(div\left(u \right) \right)^2 \Bigg) \end{aligned} \tag{2.1.9}$$

where $\frac{2}{3}\mu \left(div\left(u\right)\right)^2$ is the compressible part and u, v, w are components of the velocity $\mathbf{v}$.

2.1.2. Heat transfer

Vlachopoulos et al. [80] stated that heat transfer defines the rate of energy transferred between objects initiated by temperature differences. There are two concepts dealing with this issue. Thermodynamics considers system in equilibrium and tries to describe the change of state from one system to another regarding the required amount of heat in order to do so. The 2nd concept is the science of heat transfer. The latter deals with the question of how fast the change of state can be carried out. Thermodynamics investigates how much heat is transferred, how much work is done and determines the final state of the system. Heat transfer investigations deal with 2 major concepts, such as the rate of heat transfer and also the temperature distribution within a body.

Heat transfer modes Heat transfer can be separated into three modes:

- Conduction
- Convection
- Radiation

2.1.3. Rheological properties

Viscosity Vlachopoulos et al. [81] stated that, ”Panta Rei” or “all things flow” is the Greeks motto of rheology. In fact, all things do flow, this is just a matter of time. Rheology describes the deformation and flow of materials, with both solid and fluid characteristics. Viscosity describes the resistance to shearing. One easy and descriptive model of viscosity describes it as a deck of cards. If you shift the highest card with a certain force, underlying cards will move as well, until the force applied for shifting is less or equal then the shear stress between the cards. Once the force is no longer sufficient, no more cards will move. If you think of the deck of cards as a flow between two plates some statements can be made: Shear stress changes linearly and the shear rate nonlinearly from zero to a maximum (along the central axis to the wall). The velocity profile has a maximum at the plane and is zero at the wall (quasi-parabolic).

$$\mu = \frac{Shear\,Stress}{Shear\,Rate} = \frac{F/A}{\mathbf{v}/h} = \frac{\tau}{\dot{\gamma}} \tag{2.1.10}$$

$$\dot{\gamma} = \frac{d\gamma}{dt} \tag{2.1.11}$$

$$\dot{\gamma}_{ab} = \frac{\mathbf{v}_A - \mathbf{v}_B}{AB} \tag{2.1.12}$$

where τ it the shear stress and $\dot{\gamma}$ the shear rate. Viscosity in Eq. 1.2.12 is defined as the ratio of shear stress and shear rate or the ratio of applied force F (tangentially) divided by the area A and the velocity $\mathbf{v}$ divided by the gap h. Viscosity is measured in units of $Pa{\cdot}s$ (Pascal·second). Measurement of shear stress: Pa $= \frac{N}{m^2}$ or psi (pounds per square inch). Measurement of shear rate: reciprocal seconds (s^{-1}). Applied shear stress, shear rate, and time define the flow behaviour of melts. Shear rate can be approximated as the difference of the velocities v_A and v_B of two points A and B, as illustrated in Eq. 1.2.14.

A classification of rheological behaviour of solids and fluids had been summarized by Kohlgrüber [18]. For solids the deformation can be linear elastic, like Hookean solids or non-linear elastic or viscoelastic. Fluids can be separated between those with yield stress and those without. Viscoelasticity occur between the characteristics of elastic solids and Newtonian fluids. Shear thickening (dilatant) is defined as the increase of the viscosity caused by deformation (applied force) of the material, while a shear-thinnening (pseudoplastic) fluid implies a decrease of viscosity. These kind of fluids are also called non-Newtonian fluids. Fluids with yield stress can be separated into viscoplastic and elastoplastic fluids. Bingham fluids show a linear dependence of shear stress on shear rate, while Casson fluids show a non linear characteristic.

Newtonian fluid Newtonian fluids show a constant viscosity. The viscosity defines the fluid "stickiness"and it is independent from the stress state and the velocity of the flow. The relation between shear stress and shear rate is linear.

Non-Newtonian fluid Here the viscosity is dependent on shear rate. The relation between shear stress and shear rate is non-linear and can depend on time, resulting in a non-constant viscosity. There are different types of non-Newtonian fluids, some may become dilatant (higher viscosity), while others may become pseudoplastic (lower viscosity) when stress is applied.

Classification of the viscosities of non-Newtonian and Newtonian fluids Barman et al. [82] presented a classification of the viscous behaviour of Newtonian an non-Newtonian fluids.

- Viscosity of Newtonian fluids like water, ethyl alcohol or blood plasma show a constant viscosity tensor, which is independent of the stress state, the flow-velocity and time.
- Viscosity of non-Newtonian fluids can be time-independent dilatant or pseudoplastic. The viscosity of dilatant fluids like oobleck increases with increased stress, while the viscosity of pseudoplastics like blood or ketchup decrease with increased stress.

- Viscosity of non-Newtonian fluids can also be time-dependent classified as rheopecty- or thixotropic-fluids. Viscosity of a rheopecty fluids, like printer ink increases with the duration of applied stress, while the viscosity of thixotropic fluids like gelatin gels or yoghurt decreases with increased applied stress.
- Viscous material that show characteristics of a fluid at high stress and characteristics of a solid at low stress are called Bingham plastics

As time dependent viscosity is not relevant for the materials in extruders, I was focusing on fluids with Newtonian and non-Newtonian time-independent viscosity fluid flow behaviour.

Viscous heat generation If shear is applied on a polymeric melt heat will be evoked within the material. The heat generation is induced by friction and the magnitude of viscosity of the melt, stated by Rauwendaal [30]. Frictional heating related to HME occurs within the barell-screw and the screw-screw interface. *"In any sliding motion where a frictional force is operational, there will be frictional heat generation between two bodies"*, stated by Rauwendaal [24]. Friction is strongly related to the pressure within the barrel. In certain cases the melting temperatures can be reached only by frictional heating. In the extrusion process there are two friction coefficients. The internal coefficient of friction describes the interaction within the material, where particle layers slide over each other. On the other hand, there is the external coefficient of friction, which describes the resistance of the material particles to slide over the barrel/screw wall. Id est, it is the resistance at the particle-wall-interface between two different materials. The coefficient of friction can be written as:

$$f_{ij} = \frac{\tau_{ij}}{\tau_{ii}} \tag{2.1.13}$$

Friction in HME leads to higher temperatures differing from the temperatures induced by the heating elements mounted on the housing. As mentioned in chapter 1, in certain cases up to 80% of the temperature generation in HME can be induced by frictional heating. The frictional heat generation can be written as:

$$\dot{Q} = F_f \triangle v = f F_n \triangle v \tag{2.1.14}$$

where $F_{n/f}$ is the normal/friction force, f the coefficient of friction and $\triangle v$ is the relative velocity.

More precisely "*Viscous heat generation is the dissipation of mechanical energy in a viscous fluid*", stated by Rauwendaal [30]. Temperatures in HME are related to the viscosity of the material and the frictional heating caused by forcing material through a pipe or the shear forces in the small gap within the rotating intermeshing screws and the screw/barrel interface. Viscous dissipation causes the average temperature to rise. In certain cases the viscous heat generation needs to be compensated by cooling systems.

For a general case the viscous dissipation can be written as:

$$\Phi = \tau \dot{\gamma} \tag{2.1.15}$$

Now some statements can be made, stated by Rauwendaal [24]:

“If the shear rate is constant throughout the entire volume of a fluid, the viscous heat generation will be uniform throughout the fluid. This is the case in pure drag flow (Couette flow), i.e., flow without presence of pressure difference in the flow direction. If the shear rate is not uniform throughout the volume, the viscous heat generation will no be uniform either. This is the case in pure pressure flow (Poiseuille flow) through a pipe. In this flow situation, the shear rate in the centre is zero and maximum at the wall. Consequently, the viscous heat generation in the centre is zero and maximum at the wall. Since viscous heat generation occurs throughout a fluid, it is an effective way of heating a polymer melt because it will result in a relatively uniform temperature increase if the shear rate is approximately constant throughout the fluid.“

Models for the viscosity of non-Newtonian and Newtonian fluids For isotropic incompressible Newtonian fluids the following relation can be given:

$$\tau = \mu * \dot{\gamma} \tag{2.1.16}$$

with a constant viscosity μ and a shear rate $\dot{\gamma} = \frac{\partial u}{\partial y}$.

Viscosity η of non-Newtonian fluids depend on shear rate and can be defined as a power-law model stated by Garakani et al. [83]. In Figure 2.1.1 the application range of some viscosity models are illustrated.

$$\tau = K \dot{\gamma}^n \tag{2.1.17}$$

or

$$\eta = \mathrm{K}(\dot{\gamma})^{\mathrm{n}-1} \tag{2.1.18}$$

Where K is the flow consistency index in Si units of $Pa\, s^n$ (greater than zero), and n as the power law exponent which defines different material properties. For shear thinning fluids (pseudoplastic), n is within the range of 0 and 1, whereas a shear thickening (dilatant) characteristic is in the range from 1 to ∞. The smaller n the higher the shear thinning effect of the polymer. With $n = 1$ constant viscosity and hence the Newtonian model is acquired. Note, there are different viscosity

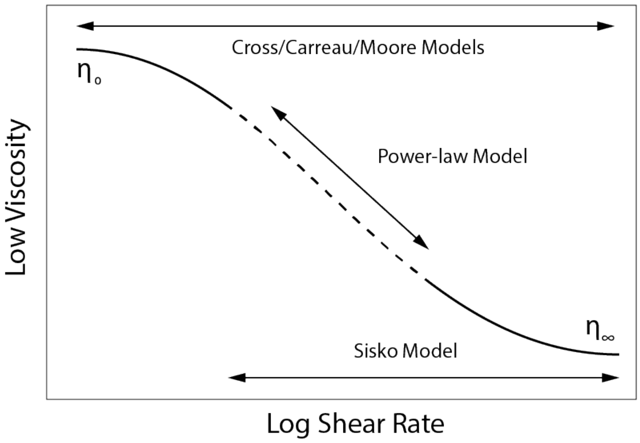

Figure 2.1.1.: Range of application of the power-law viscosity models.

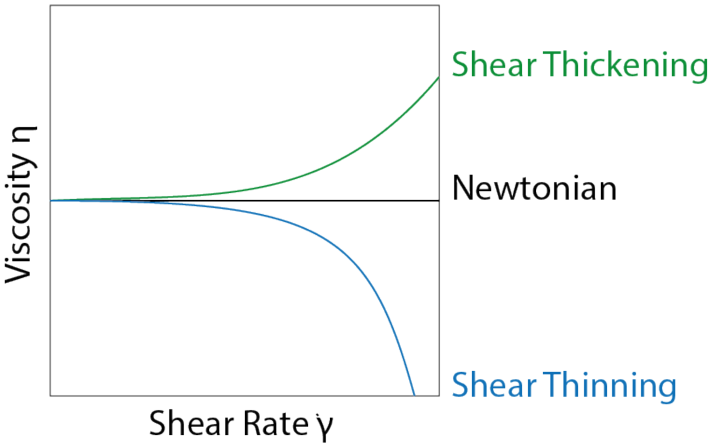

Figure 2.1.2.: Newtonian, pseudo plastic and dilatant characteristics.

models, such as models with temperature dependence for non-Newtonian fluids. Shear thinning, also known as pseudoplastic behaviour, is one notable property of polymeric liquids. It describes the phenomenon of reducing viscosity while increasing the rate of shearing. As described by Rauwendaal [24] polymer melts are shear thinning (pseudoplastic) fluids and characteristic for certain polymers. At low shear rates the viscosity is almost independent of shear rate. This implies a Newtonian behaviour, while at hight shear rates the viscosity is highly dependent on shear rate. This phenomenon is caused by molecular alignments of the polymer chains. While extruding a compound, shear rates at the screws are much smaller (can reach 200 s^{-1}in SKE) then at the dip of the die (up to 1000 s^{-1} in SKE). Therefore the movement of the polymer melt at the screw is small while it is much higher at the die. Same goes for wall shear rates at the barrel/screw-interface. Melt fractures may appear at very high shear rates, described by Vlachopoulos et al. [81]. With the power law model this function can be approximated with a constant line (power-law region), as shown in Figure 2.1.1. In Figure 2.1.2 the Newtonian, pseudoplastic and dilatant fluid flow behaviours are illustrated.

In order to make a fluid without yield stress flow, a certain amount of shear

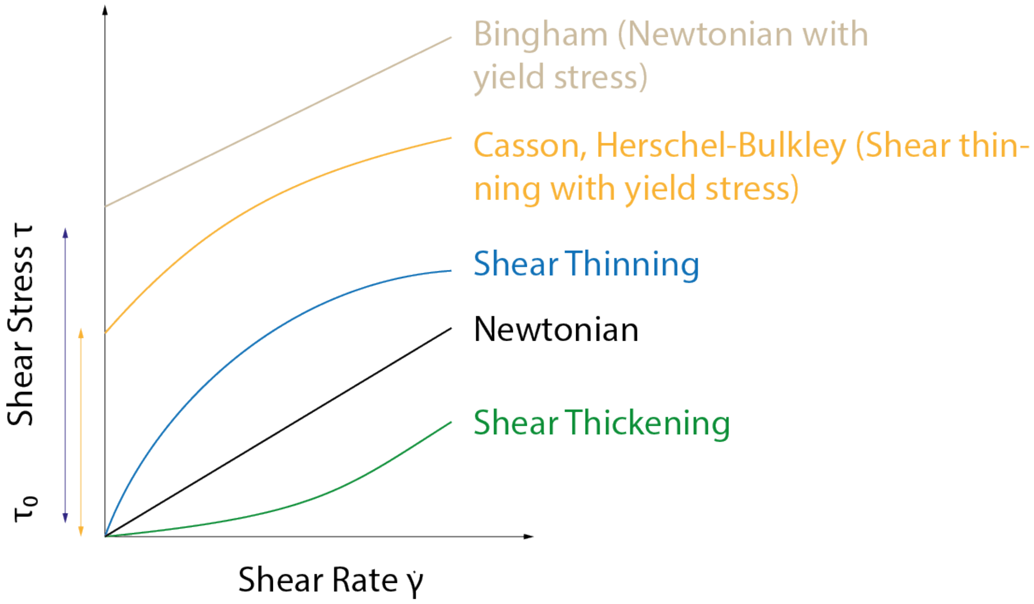

Figure 2.1.3.: Overview of the viscous behaviour of a variety of models.

stress τ_0 has to be applied. Below τ_0 the material is a solid. By adding τ_0 the Herschel-Bulkley correlation, described by Herschel [84] can be obtained:

$$\tau = K * \dot{\gamma}^n + \tau_0 \tag{2.1.19}$$

In Figure 2.1.3 the relation of shear rate and shear stress for different fluid models can be seen. Kohlgruber [18] found that in extrusion shear rates are usually in the range of 100-1000 s^{-1}. While the shear rate of polymer melts at processing temperature is zero, the viscosities can range from 100 to 10^6 Pas.

There are many fluid models describing the viscosity which are covering Newtonian / non-Newtonian fluid flow characteristics, such as:

- The Bingham model by Bingham [85]:

$$\tau = \tau_0 + \mu_p \gamma^n \tag{2.1.20}$$

where τ_0 is a yield point and μ_p is the plastic viscosity.

- A polynomial relation developed by Rabinowitsch and Weissenberg [86]:

$$\dot{\gamma} = \alpha_1 \tau + \alpha_3 \tau^3 \tag{2.1.21}$$

where α is a rheological constant related to the type of fluid.

- The Carreau model [87]:

$$\frac{\eta - \eta_{\infty}}{\eta_0 - \eta_{\partial}} = [1 + (\lambda\dot{\gamma})^{2}]^{\frac{n-1}{2}} \tag{2.1.22}$$

where η is the viscosity and λ a time constant.

- The Ellis model [86]:

$$\frac{\eta_0}{\eta} = 1 + \left(\frac{\tau}{\tau_{1/2}}\right)^{\alpha - 1} \tag{2.1.23}$$

with η_0 as the zero shear rate viscosity and $\tau_{1/2}$ as the shear stress at $\eta = \eta_{0/2}$.

- The Cross model [81]:

$$\eta = \frac{\eta_0}{1 + (\lambda\dot{\gamma})^{1-n}} \tag{2.1.24}$$

where η is the viscosity, n is the dimensionless exponent and λ is a time constant.

- The Moore model [88]:

$$\eta\,(t) = \eta_{\infty} + (\eta_0 - \eta_{\infty})\,\lambda \tag{2.1.25}$$

where, η is the viscosity, η_{∞} is the infinite shear viscosity and λ is an structural parameter.

Temperature viscosity relationship Rauwendaal [30] stated, that the viscosity is reduced if the temperature of a polymer melt is increased. This behaviour varies for different polymeric materials. Usually amorphous materials are more temperature sensitive then semi-crystalline materials.

The glass transition temperature describes the reversible transition from a hard (glass) state into a viscous state (amorphous materials) as the temperature increases due to internal movement of the polymer chains that form the solid/-plastic. More precisely the glass-transition-temperature T_g defines the range of temperature of the glass transition. Lang et al. [32] found, that the transition temperature has a wide range depending on the chemical structure ranging from 36°C (EVAc) up to 184°C (HPMC). Sperling et al. [89] found that the melt viscosity is depended on the glass transition temperature of polymer carriers. While glass transition occurs in amorphous polymers, melting happens to crystalline polymers. Amorphous polymers show no arranged order in their structure. In the process of melting, the polymer chains fall apart of their crystalline structure and form a disordered liquid. Note that crystalline polymers have amorphous regions (40% - 70%), therefore both quantities, glass transition and melting temperatures are crucial temperature parameters for the sample polymer. Here the amorphous part undergoes glass transition, while the crystalline part undergoes melting. Polystyrene is a hard plastic and therefore it is used below its glass transition temperature, while for example rubber elastomers are used above their

T_g, inducing the flexible and soft behaviour of this material. For amorphous polymers, Sperling introduced the William-Landel-Ferry equation (WLF):

$$\log\left(\frac{\eta}{\eta_{Tg}}\right) = \frac{-C_{1(T-T_g)}}{C_{2+(T-T_g)}} \tag{2.1.26}$$

where C_1, C_2 are constants, η and η_{Tg} are melt viscosities at processing and glass transition temperature, respectively

- An empirical model for the exponential temperature dependence of viscosity described by Rauwendaal [24] can be written as:

$$a_T = \exp\left[\alpha_T\left(T_r - T\right)\right] \tag{2.1.27}$$

where α_T is the temperature coefficient, T_r the reference temperature and a_T the shift factor.

- The Power law model with temperature dependence presented by Rauwendaal [24], is given as:

$$\tau = K_r a_T \dot{\gamma}^n \tag{2.1.28}$$

or

$$\eta = K_r a_T \dot{\gamma}^{n-1} \tag{2.1.29}$$

Assuming, that for many materials the shape of the viscosity-shear stress curve won't change when temperature is changed, this curve can be shifted with a_T accordingly to the temperature changes in order to generate a master curve.

The Arrhenius equation, a more general expression with temperature dependence on viscosity of fluids, also called the dynamic viscosity, can be written as:

$$\eta = \eta_0 \exp\left(\frac{E_A}{RT}\right) \tag{2.1.30}$$

where η_0 is a material constant, E_A is the activation Energy, R is the gas constant and T is the absolute temperature.

A power-law model with exponential temperature dependence, which had been used for validation stated by Turian et. al [90] can be written as:

$$\eta = \eta_0 \dot{\gamma}^{(n-1)} \exp\left(-\beta\Theta\right) \tag{2.1.31}$$

with

$$\Theta = \frac{T - T_0}{T_0} \tag{2.1.32}$$

where η is the non-Newtonian viscosity, η_0 is the viscosity at temperature T_0, Θ is the dimensionless temperature rise, β is the dimensionless coefficient in exponential viscosity-temperature relation and n is the power law index. With $n = 1$ the Newtonian model can be obtained, whereas with $n < 1$ the model provides a non-Newtonian pseudoplastic and for $n >1$ a non-Newtonian dilatant behaviour.

2.1.4. Shear flows

Shear flows can be either pressure driven, i.e. Poiseuille flows, or drag induced, defined as Couette flow. In extrusion processing not only pressure and drag flows, but also extensional flows occur. In this section I will give an overview on these flow models.

Poiseuille flow: The Poiseuille flow is defined as a laminar, stationary pressure induced channel flow. No turbulences occur and the flow behaves antisymmetrically, therefore only axial u_z components of the velocity profile are non-zero. Derived from the Navier-Stokes equation, the flow is assumed to be fully developed without slip at the wall and the yields are symmetric at the centre, leading to a parabolic velocity profile with u_{zmax} at the centre.

Couette flow The flow between two plates separated by a distance h is induced by the relative movement of one plate. The shear rate and the velocity profiles are not dependent on the properties of the fluid. The shear stress is constant.

Extensional Flow Wherever the cross section is very small the fluid will be compressed and extended. In extruders this happens at the tips or between the kneading elements and the wall. Extensional viscosity, also called melt strength describes the resistance of a fluid to extension, stated by Vlachopouos et al. [81]. The Trouton ratio, describes the resistance to stretching and shearing of rigid liquids. Trouton found that the ratio, valid for all Newtonian fluids is 3. This relation is called extensional or elongational viscosity (μ_e):

$$\mu_e = \frac{\sigma}{\varepsilon} \tag{2.1.33}$$

$$\frac{\mu_e}{\mu} = 3 \tag{2.1.34}$$

Extensional viscosity has influence on the manufacture regarding the type of application (film, blowing, coating, palletizing, spinning etc.) As a more precise description about extensional flow is outside the scope of this thesis, more detailed information about extensional flow can be read at “The Role of Rheology in Polymer Extrusion” by Vlachopoulos et al. [81].

Stokes flow: The stokes flow, also called creeping flow is a fluid flow occurring at very small Reynolds numbers $Re << 1$. Typical for Stokes flow are very low velocity- and high viscosity-profiles without turbulences. Lava flow or sperm have the characteristics of a stokes flow. In extruder processing creeping flows occur while mixing highly viscous material.

2.1.5. Molecular parameters influencing polymer melts

Factors influencing a fluid flow are ambient condition such as temperature and pressure, the external forces that are acting on the material such as gravity and also the inner structure of the material. Ferry et al. [91] found that Parameters such as molar mass, molar mass distribution and the molecular topology influence the rheological behaviour of polymer melts. For example a material with a very tight linking on the molecular level is more resistant to deformation and hence less “willing” to flow. Also the concentration of the dissolved substances in the material influence the viscosity. Low viscosity is associated with a low concentration and vice versa. High intermolecular attractive forces are related to higher viscosity. Another major effect on viscosity is the particle size. While small particle can move more freely, bigger particles are more restricted in their movement and therefore related to a higher viscosity.

2.1.6. Dimensionless relations in fluid dynamics

Reynolds number The Reynolds number is the ratio of inertial forces to viscous forces with respect to a fluid.

$$Re = \frac{\rho \mathrm{vL}}{\mu} \tag{2.1.35}$$

where ρ, v, L, μ is the density of the fluid, velocity of the fluid, linear dimension, dynamic viscosity of the fluid

Another definition of the Reynolds number used in extrusion can be written as:

$$Re = \frac{nD^2\rho}{\eta} \tag{2.1.36}$$

with n as revolutions per minute, D as diameter, æas density and η as viscosity.

With the Renyolds number laminar and turbulent flows can be calssified. At low Reynolds numbers, with high viscous forces and constant fluid motion a laminar flow occurs, while at high Reynolds numbers turbulent flow occurs. For channel flows, Reynolds numbers above 2100 are associated with turbulent flows. Turbulent flows are characterized by dominant inertial forces, which leads to flow instabilities. In the case of melt extrusion no critical Reynolds number will occur (10^{-3}) and therefore in this thesis I will focus on viscous, laminar flows.

Brinkman number *"The Brinkman number is a non-dimensional parameter that characterizes viscous dissipation in fluid flow"*, stated by Atkins et al. [92]

$$\mathrm{Br} = \frac{\mu v^2}{k(T_w - T_0)} = PrEc \tag{2.1.37}$$

where μ, v, k, T_w, T_0, Pr, Ec, is dynamic viscosity, flow velocity, thermal conductivity, bulk fluid temperature, wall temperature, Prandtl and Eckert number

2.2. Equations of SPH

In this section the most important equations in SPH for weakly compressible flows will be represented. This approaches is available in XPS (eXtended Particle System), which is under development at RCPE.

"XPS is a particle simulation framework originally developed for the simulation of granular flows using the discrete element method (DEM). It is written in `C++` and `CUDA` and is executed on general-purpose graphical processing units (GPGPUs). The smoothed particle hydrodynamics (SPH) method was added to XPS to be able to simulate fluid flows. As this macroscopic (continuum mechanical) approach uses particles for the discretisation of the fluid, it requires minimal modifications of the existing DEM framework." stated by Kondor et al. [10], the lead developer of SPH at RCPE, Graz.

2.3. The foundation

The interpolation in SPH for a specific quantity A, where A is a function of spatial coordinates was represented by Monaghan et al. [93]:

$$A_I(\mathbf{r}) = \int A(\mathbf{r}')W\left(\mathbf{r} - \mathbf{r}', h\right) d\mathbf{r}' \approx \sum_b A\left(\mathbf{r}_b\right) W\left(\mathbf{r} - \mathbf{r}_b, h\right) \tag{2.3.1}$$

with W as the kernel function, h as the smoothing length and $d\mathbf{r}'$ as the differential volume element. If the kernel is replaced with a delta function, the interpolation can generate A exactly. In general a kernel approximates the delta function. If the interpolation is used on fluids, a division into small mass elements is carried out, where "a" represents a specific element, with a mass m_a, density ρ_a, the position $\mathbf{r}_a$ and a value of A_a for a certain particle "a". With this approach we can represent any quantity by the summation of the quantity of nearby points, multiplied by a weighting function W, a smoothing kernel. W gives nearby particles more strength and particles further away less strength resulting in a weaker influence on the system until a certain point, where W becomes 0. Now the interpolation integral, where $\rho d\mathbf{r}'$ represents an element of mass can be stated as:

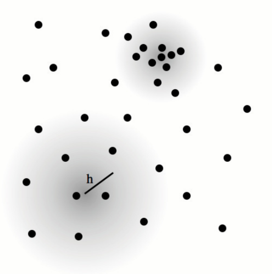

Figure 2.3.1.: SPH approach to computed the density [8].

$$\int \frac{A\left(\mathbf{r}^{'}\right)}{\rho\left(\mathbf{r}^{'}\right)}\rho\left(\mathbf{r}^{'}\right)d\mathbf{r}^{'} \tag{2.3.2}$$

Eq 2.2.2 can be approximated by summation over the mass elements depending on the smoothing length h:

$$A_s\left(\mathbf{r}\right)=\sum_b m_b\frac{A_b}{\rho_b}W\left(\mathbf{r}-\mathbf{r}_b,h\right) \tag{2.3.3}$$

Usually the kernel becomes 0 at a finite distance as compact support is used. Compact support is used for the summation over the nearest neighbours, to reduce computational cost.

The very basis of the Lagrangian particle method SPH deals with the calculation of the density of an arbitrary distribution of point-mass-particles. There are different approaches to solve this problem stated by Price et al. [8], where the most accurate equation computes the density with a weighted summation over nearby particles in order to estimate a density at a point $\mathbf{r}$:

$$\rho(\mathbf{r})=\sum_{b=1}^{N_{neigh}} m_bW\left(\mathbf{r}-\mathbf{r}_b,h\right) \tag{2.3.4}$$

with W as the weight function, h as a scale parameter describing the “fall-off-rate” of W and $\mathbf{r}$ as the particle position. In Figure 2.3.1 the SPH approach with the “weighted sum over neighbouring particles” and the scale factor is illustrated.

For the conservation of total mass Eq 2.3.5 is required to have a normalised kernel Eq 2.3.6, resulting in:

$$\int \rho dV=\sum_{b=1}^{Npart} m_b \tag{2.3.5}$$

$$\int_V W\left(\mathbf{r}^{'}-\mathbf{r}_b,h\right)dV^{'}=1 \tag{2.3.6}$$

with ρ as density, V as the volume and m_b as the mass of particle a. Then the smoothing kernel (weight function) is determining the accuracy of the density estimation. Price et al. [8] collected the essential properties of the kernel:

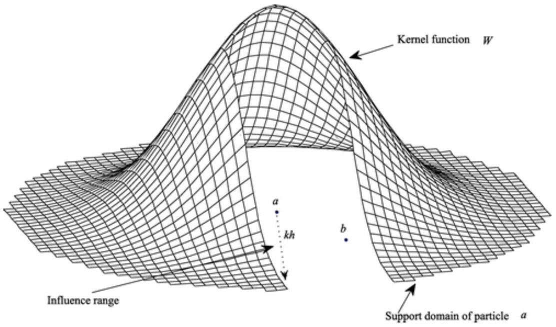

Figure 2.3.2.: Support domain with the kernel function W [9].

- Positive weight
- Monotonic decrease
- At least two smooth derivates
- Symmetry: $W(\mathbf{r}^{'} - \mathbf{r}, h) \equiv W(\left|\mathbf{r}^{'} - \mathbf{r}\right|, h)$
- Flat central portion leading to little impact by small position change of a neighbour

In Figure 2.3.2 an illustration of the support domain for an particle with the kernel function W can be seen, presented by Deb et al. [9]. There are different kernel functions such as the Gaussian, Wendland or the Schoenberg B-Spline functions shown as a Fourier transform. The general $\mathrm{M_n}$ spline function can be written as the Fourier transform:

$$M_n(x,h) = \frac{1}{2\pi}\int_{-\infty}^{\infty}\left[\frac{sin(kh/2)}{kh/2}\right]^n cos(kx)dk \qquad (2.3.7)$$

While the Gaussian approach considers the number of neighbours as infinite, the higher order B-Spline approach can generate a change in neighbour-number without changing the defined smoothing scale h. Therefore h is a size parameter. For this simulation the cubic spline approach will be used. Usually a kernel which vanishes at a finite distance, called kernels with compact support is used, as stated by Monaghan et al. [93].

2.3.1. Smoothing length

Originally the smoothing length was set to a constant resolution h, which was able to change with time. Another more precise approach resolves both, the clustered and the sparse region in the same way in order to relate the density of particles. For the calculation of the location of one particle “a”, a summation over a set of particle neighbours “b” is carried out, leading to the following equations, which is true for compressible flows:

$$\rho(\mathbf{r}_a) = \sum_b m_b W(\mathbf{r}_a - \mathbf{r}_b, h_a) \qquad (2.3.8)$$

$$h\left(\mathbf{r}_a\right)=\omega\left(\frac{m_a}{\rho_a}\right)^{1/d} \tag{2.3.9}$$

where d is the dimension and ω a value specifying the smoothing length in $[m/\rho]^{1/d}$. In order to solve both equations at the same time, standard root finding methods are used. These equations serve to “keep the mass in the smoothing sphere”. Here the density equation is time independent, but density depends on the particle positions and masses. As a result the density field can be calculated from point mass particles. This approach is also used to calculate supersonic turbulences and also represents a foundation for the gravitational force softening method represented by Price and Monaghan et al. [94]. In the SPH code, developed at RCPE a constant smoothing length is used.

$$h\left(\mathbf{r}_a\right)\equiv const \tag{2.3.10}$$

2.3.2. Discrete Lagrangian

In order to obtain a fully conservative SPH algorithm, density estimations are used. The discrete Lagrangian equation is a function of the dynamics of a system, where T is the kinetic and V the potential or thermal energies.

$$L=T-V \tag{2.3.11}$$

In order to generate a system of point masses, where the velocity v is dr/dt and the internal energy u is a function of density and entropy we can say:

$$L=\sum_b m_b\left[\frac{1}{2}v^2-u_b\left(\rho_{b,}s_b\right)\right] \tag{2.3.12}$$

2.3.3. Derivation of Euler Lagrange

With the help of the principle of least action the equation of motion is obtained:

$$S=\int Ldt \tag{2.3.13}$$

with δ as a variation with respect to change of the particle coordinates δr:

$$\delta S=\int \delta Ldt=0$$

The Lagrangian is a differentiable function, where r is the particle position and v is the velocity:

$$\delta S = \int \left(\frac{\partial L}{\partial \mathbf{v}} \delta \mathbf{v} + \frac{\partial L}{\partial \mathbf{r}} \delta \mathbf{r} \right) dt = 0 \tag{2.3.14}$$

Now an integration by parts can be accomplished, where $\delta \mathbf{v} = d(\delta \mathbf{r})/dt$ and d/dt $= \partial/\partial t + \mathbf{v}\nabla$:

$$\delta S = \int \left(\left[-\frac{d}{dt} \left(\frac{\partial L}{\partial \mathbf{v}} \right) + \frac{\partial L}{\partial \mathbf{r}} \right] \delta \mathbf{r} \right) dt + \left[\frac{\partial L}{\partial \mathbf{v}} \delta \mathbf{r} \right]_{t_0}^{t} = 0 \tag{2.3.15}$$

With an arbitrary variation of δr and no variation for the start and end times the equation of motion can be expressed as the Euler-Lagrange equation such as:

$$\frac{d}{dt} \left(\frac{\partial L}{\partial \mathbf{v}_a} \right) - \frac{\partial L}{\partial \mathbf{r}_a} = 0 \tag{2.3.16}$$

2.3.4. Equation of motion

The Euler Lagrange equation can be expressed as a function of coordinates and velocities:

$$\frac{\partial L}{\partial \mathbf{v}_a} = m_a \mathbf{v}_a \tag{2.3.17}$$

$$\frac{\partial L}{\partial \mathbf{r}_a} = -\sum_b m_b \frac{\partial u_b}{\partial \rho_b} |_s \frac{\partial \rho_b}{\partial \mathbf{r}_a} \tag{2.3.18}$$

Here the entropy is constant, in order to achieve no dissipation where u is a function of density ρ and entropy s.

2.3.4.1. Thermodynamics

The first law of thermodynamics, with $\delta Q \equiv TdS$ as “added heat” and $\delta W \equiv PdV$ the work depending on expansion and compression of the fluid can be captured. The volume as units per mass, were V= m/ρ and dV = -m/$\rho^2 d\rho$ leads to:

$$dU = TdS - PdV \tag{2.3.19}$$

$$du = Tds + \frac{P}{\rho^2} d\rho \tag{2.3.20}$$

where uis the internal energy per unit mass and U is the internal energy per unit volume. With constant entropy the change in thermal energy can be written as:

$$\frac{\partial u_b}{\partial \rho_b} |_s = \frac{P}{\rho^2} \tag{2.3.21}$$

2.3.4.2. Density gradient

The spacial derivative of Eq. 2.3.18 at a particle “b” with respect to the position of particle “a” can be written as:

$$\frac{\partial \rho_b}{\partial \mathbf{r}_\mathrm{a}} = \frac{1}{\Omega_b} \sum_c m_c \frac{\partial W_{bc}\left(h_b\right)}{\partial \mathbf{r}_\mathrm{a}} \left(\delta_{ba} - \delta_{ca}\right) \tag{2.3.22}$$

where $W_{bc}\left(h_b\right) \equiv W\left(\mathbf{r}_\mathrm{b} - \mathbf{r}_\mathrm{c}, h_b\right)$, δ_{ba} is the Dirac delta function, $h = h(p)$ for constant h, $\Omega = 1$ and the derivation of a constant becomes 0. Now Eq. 2.3.23 can be obtained:

$$\Omega_a \equiv \left[1 - \frac{\partial h_a}{\partial \rho_a} \sum_b m_b \frac{\partial W_{ab}\left(h_a\right)}{\partial h_a}\right] \tag{2.3.23}$$

For the $h - p$ relation from Eq. 2.3.8 and Eq. 2.3.9 the derivation can be written as:

$$\frac{\partial h}{\partial \rho} = -\frac{h}{\rho d} \tag{2.3.24}$$

with d as the number of spatial dimensions.

2.3.4.3. Standard SPH expression

If Eq. 2.3.21 and 2.3.22 is applied into Eq 2.3.17 and 2.3.18 the following equations can be written as:

$$\frac{\partial L}{\partial \mathbf{r}_a} = -\sum_b m_b \frac{P_b}{\Omega_b \rho_b^2} \sum_c m_c \frac{\partial W_{bc}\left(h_b\right)}{\partial \mathbf{r}_\mathrm{a}} \left(\delta_{ba} - \delta_{ca}\right) \tag{2.3.25}$$

With some simplification, the Euler-Lagrangian for the equation of motion is obtained:

$$\frac{\partial \mathbf{v}_a}{dt} = -\sum_b m_b \frac{P_a}{\Omega_a \rho_a^2} \frac{\partial W_{ab}\left(h_a\right)}{\partial \mathbf{r}_\mathrm{a}} + \frac{P_b}{\Omega_b \rho_b^2} \frac{\partial W_{ab}\left(h_b\right)}{\partial \mathbf{r}_\mathrm{a}} \tag{2.3.26}$$

with the smoothing length $h_a = h_b = h = const.$ the standard SPH expression can be written as:

$$\frac{\partial \mathbf{v}_a}{dt} = -\sum_b m_b \left(\frac{P_a}{\rho_a^2} + \frac{P_b}{\rho_b^2}\right) \cdot \nabla_a W_{ab} \tag{2.3.27}$$

2.3.4.4. Summary

In this section the SPH-equations which are solved explicitly are listed, stated by Kondor [10]:

1. Equation of Continuity:

$$\frac{d\rho_a}{dt} = \sum_b m_b \left(\mathbf{v_a} - \mathbf{v_b}\right) \cdot \nabla_a W_{ab} \tag{2.3.28}$$

   where ρ_a is the particle density, $m_a$is the mass of the particle, $\mathbf{v}$ is the velocity and W_{ab} the smoothing kernel.

2. Momentum Equation:

$$\frac{\partial \mathbf{v}_a}{dt} = -\sum_b m_b \left(\frac{P_a}{\rho_a^2} + \frac{P_b}{\rho_b^2} + Rf_{ab}^4\right) \cdot \nabla_a W_{ab} + \sum_b m_b \frac{1}{\rho_a \rho_b} \frac{4\mu_a \mu_b}{\mu_a + \mu_b} \left(\frac{1}{\mid \mathbf{r}_{\mathrm{ab}} \mid} \frac{\partial W_{ab}}{\partial \mathbf{x}_{\mathrm{a}}}\right) \mathbf{v}_{\mathrm{ab}} + \mathbf{a} \tag{2.3.29}$$

   where Rf_{ab}^4 is the artificial pressure within the pressure term. The Morris viscosity is used for the viscosity term of this equation. $\mathrm{P_a}$is the pressure of the particle , ¯$_{\mathrm{a}}$is the dynamic viscosity and $\mathbf{a}$ is a volume force.

3. Tait's equation of state:

$$P_a = \frac{c^2 \rho_0}{\gamma} \left[\left(\frac{\rho_i}{\rho_0}\right)^\gamma - 1\right] + P_{back} \tag{2.3.30}$$

   In order to close the continuity and momentum equation (2.3.28 and 2.3.29), Tait's EoS is used by relating the particle pressure to the particle density. Where c is the speed of sound, ρ_0 is the reference density at $P = 0$, $P_{back}$is the background pressure and γ is used to ensure weakly compressibility.

4. Time integration:

   In order to update the particles position the Verlet scheme. Here a temporal integration of the governing equations is carried out. The update sequence can be written as:

$$\boldsymbol{v}^{n+1/2} = \boldsymbol{v}^n + 0.5\Delta t \left(\frac{\mathrm{d}\boldsymbol{v}}{\mathrm{d}t}\right)^n \tag{2.3.31}$$

$$\boldsymbol{v}^{n+1,est} = \boldsymbol{v}^n + \Delta t \left(\frac{\mathrm{d}\boldsymbol{v}}{\mathrm{d}t}\right)^n \tag{2.3.32}$$

$$\boldsymbol{r}^{n+1} = \boldsymbol{r}^n + \Delta t \boldsymbol{v}^{n+1/2}. \tag{2.3.33}$$

   where n is the time level. In the next step the change in density is updated:

$$\rho^{n+1} = \rho^n + \Delta t \left(\frac{\mathrm{d}\rho}{\mathrm{d}t}\right)^{n+1}. \tag{2.3.34}$$

With the updated values the forces are calculated. In the last step the new velocity is calculated such as:

$$\boldsymbol{v}^{n+1} = \boldsymbol{v}^{n+1/2} + 0.5\Delta t \left(\frac{\mathrm{d}\boldsymbol{v}}{\mathrm{d}t}\right)^{n+1} . \tag{2.3.35}$$

The time step criterion can be written as:

$$\Delta t \leq \min\left(0.25\frac{h}{c},\ 0.25\sqrt{\frac{h}{a}},\ 0.125\frac{h^2}{\nu},\ 0.15 c_p \rho \frac{h^2}{\kappa}\right) . \tag{2.3.36}$$

3 Chapter 3.
Comparison

In this section the comparison of analytical solutions with simulations will be discussed. As a test model the 3D-XPS-Simulations of a rectangular channel will be expressed into 2-D-profiles and matched against analytical or experimental data. Figure 3.0.1 shows the geometry which had been used for the channel flow simulations. It contains 6 flat STL-plates called left, right, top, bottom, front and back. The length L is 10 mm, the height H = 5 mm and the width W = 1 mm. The fluid flows in the positive x direction by a drag or pressure induced flow. In Figure 3.0.2 the XPS front post view of an 3-D channel flow simulation, which had been used for the comparison can be seen. A more detailed description about this simulation can be read in section 3.2. XPS provides several post processing tools including staining, cutting, creating videos or the calculation of statistics of the simulation. The channel flow simulations consist of 6250 particles in total. Periodic boundaries are defined for the left and right plate in order to simulate an infinitely long channel. For the heat transfer simulation fixed temperatures had been prescribed for the top and bottom plate. In order to simulate viscous heating, zero heat flux boundaries had been set for the top and bottom plate. Typical velocity and shear rate parameters which are present in extrusion had been used for the channel flow simulations.

3.1. Pressure and drag flow

In this Section the validation of pressure and drag induced flows are illustrated. Kondor [10] could show, that the implementation of the models for the flow fields worked very well and that the results of the XPS-code are in agreement with the analytical solution.

3.1.1. Couette flow

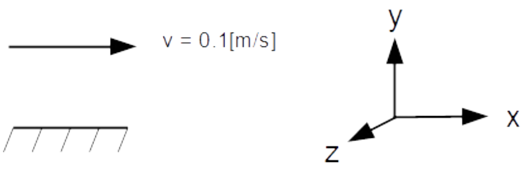

Figure 3.1.1.: Sketch of the simulation setup for a Couette flow.

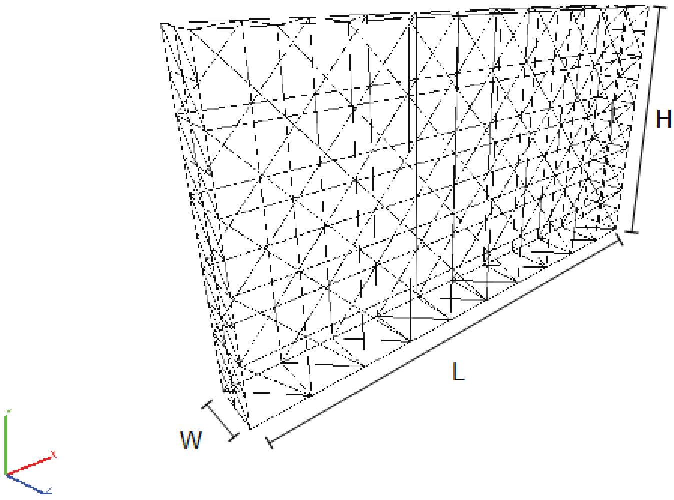

Figure 3.0.1.: Geometry of the channel flow simulation.

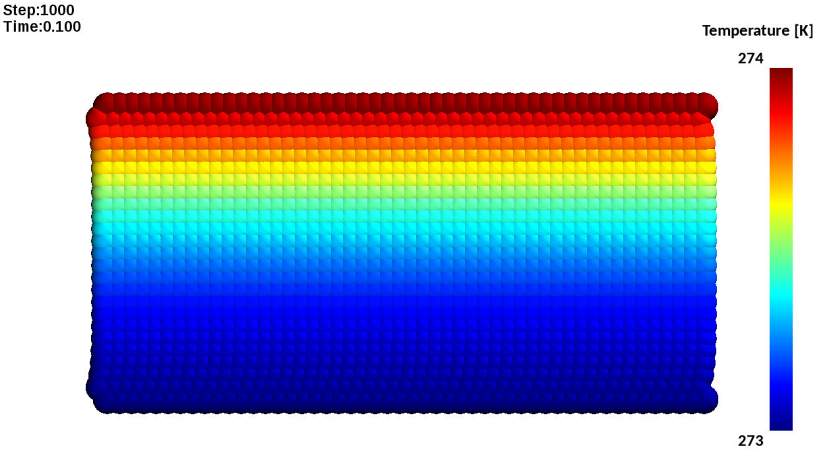

Figure 3.0.2.: Post view of the simulation for the heat transfer of $\triangle T$ is 1 Kelvin for 0.1 second.

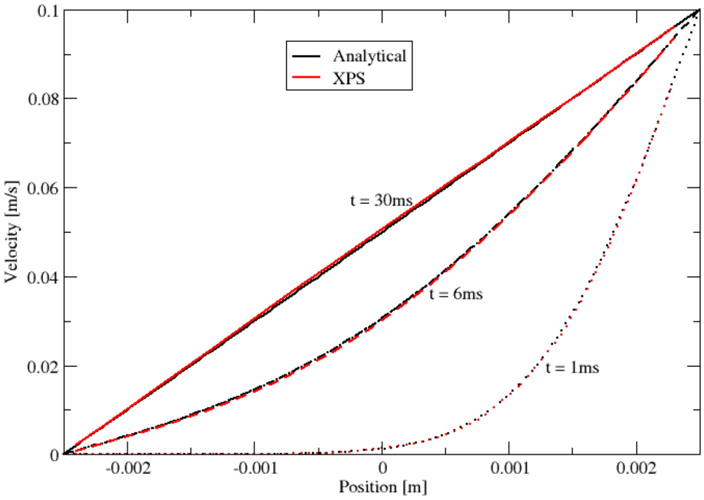

Figure 3.1.2.: Velocity profile of a drag induced flow for 1, 6 and 30 ms, [10].

Figure 3.1.1 shows a sketch of the simulation setup for a drag induced flow. In Figure 3.1.2 the velocity profile of a couette flow at 1, 6 and 30 ms is illustrated. The flow is induced with a lead velocity of 0.1 m/s. This validation was carried out by Kondor [10] and as illustrated he could show that the analytical results are in very good agreement with the XPS results.

3.1.2. Poiseuille flow

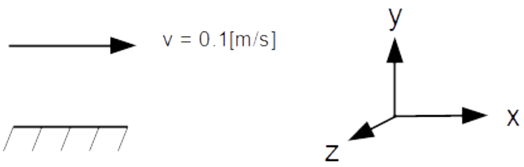

Figure 3.1.3.: Sketch of the simulation setup for a Poiseuille flow

Figure 3.1.3 shows a sketch of the simulation setup for a pressure driven flow. In Figure 3.1.4 the velocity profile of a Poiseuille flow at 1, 6 and 30 ms can be seen. The flow is induced with a gravity-force of 10 m/s^2 in the x direction.This validation was carried out by Kondor [10] and as illustrated he could show that the XPS results are in very good agreement with the analytical results.

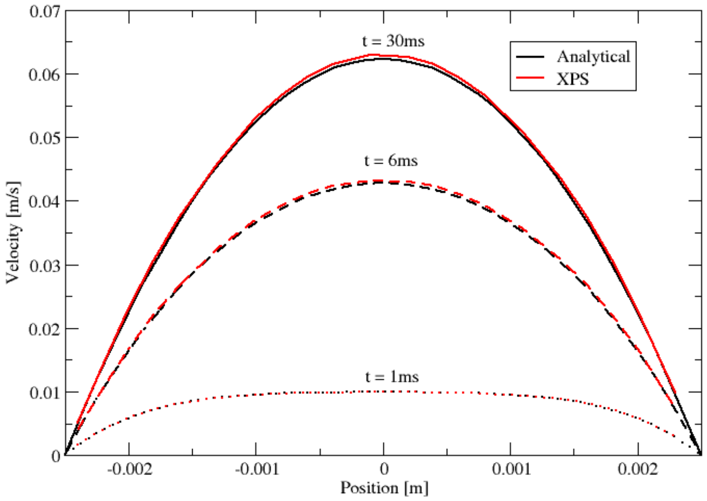

Figure 3.1.4.: Velocity profile of a pressure induced flow for 1, 6 and 30 ms, [10].

3.2. Heat transfer

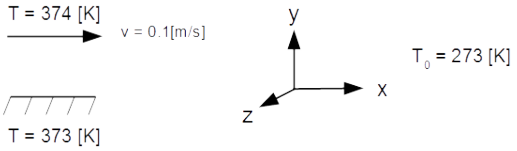

Figure 3.2.1.: Sketch of the simulation setup for the heat transfer

In Figure 3.2.1 a sketch of the simulation setup for heat transfer can be seen.

The heat equation In order to correctly calculate energy transferred between objects induced by temperature differences, the parabolic partial differential heat equation had been used to calculate the variation in temperature:

$$\frac{\partial u}{\partial t} = \alpha \nabla^2 u \tag{3.2.1}$$

with

$$\alpha = \frac{k}{\rho c_p} \tag{3.2.2}$$

where $u(x, y, z, t)$ is the temperature and α the thermal diffusivity.

A model for the heat transfer of a Poiseuille flow was obtained using a Wolfram Alpha development platform[1] for the calculation of the well known partial dif-

---

[1] https://www.wolframalpha.com/

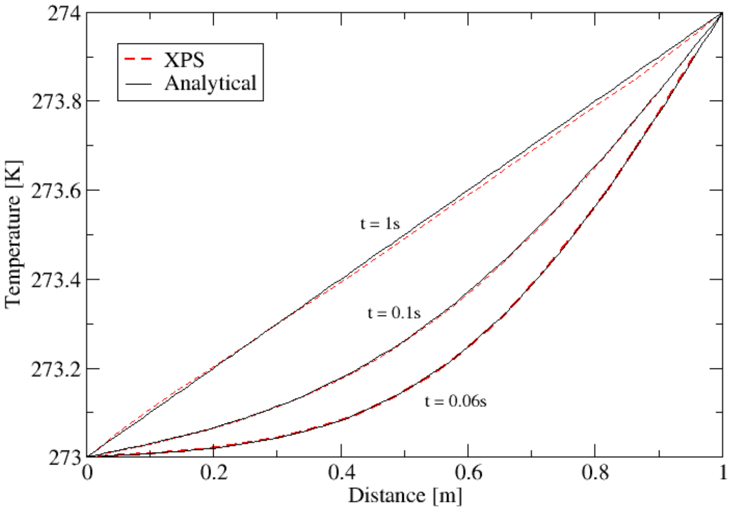

Figure 3.2.2.: Temperature profile for 0.06 , 0.1 and 1 s.

ferential heat equation. The validation was executed with a $\triangle T$ of 1K for 3 different time steps, 1, 0.1 and 0.06 s. As shown in Figure 3.2.2 the results of the heat transfer model implemented into XPS are in very good accordance with the analytical results.

3.3. Viscous heating

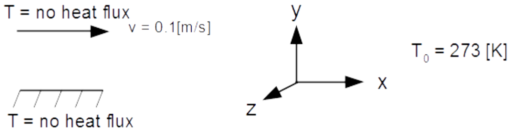

Figure 3.3.1.: Sketch of the simulation setup for viscous heating

Figure 3.3.1 shows a sketch of the viscous heating simulation setup. In Figure 3.3.2 the temperature development of viscous heating induced by friction and the magnitude of the viscosity in a time-frame of 5 ms is shown. The XPS solution of the viscous heating model expressed from the heat equation matches the analytical data as expected with an error below 1%. For the validation zero heat flux boundaries had been used and Eq. 2.1.7 was reduced to:

$$\frac{\partial T}{\partial t} = \frac{\mu}{\rho c_p} \left(\frac{\partial u}{\partial y} \right)^2 \tag{3.3.1}$$

where u is the velocity component in the y-direction, μ is the kinematic viscosity, ρ as density, $\mathrm{c_p}$ as specificity heat capacity and T as temperature.

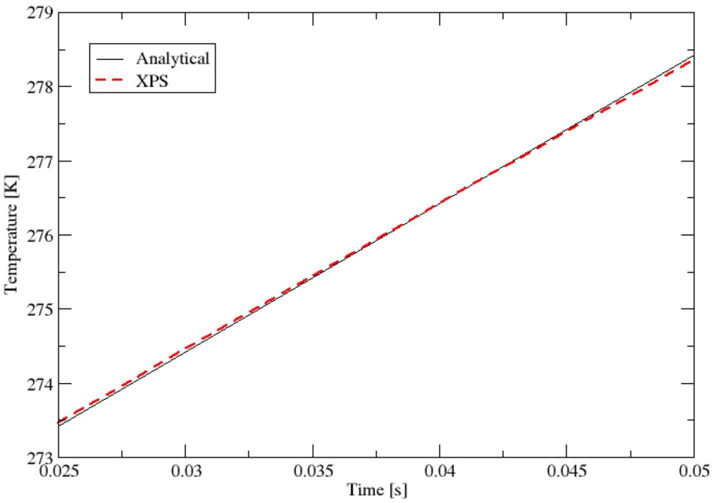

Figure 3.3.2.: Temperature profile with viscous heating for 5 ms.

3.4. Power law viscosity

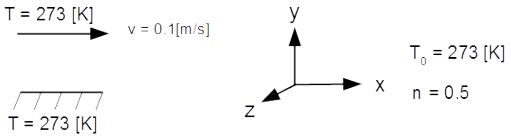

Figure 3.4.1.: Sketch of the simulation setup for a power law viscosity in a Couette flow

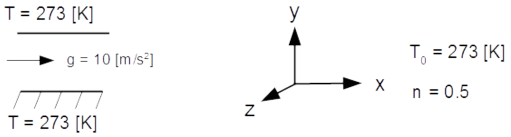

Figure 3.4.2.: Sketch of the simulation setup for a power law viscosity in a Poisseuille flow

Figure 3.4.1 - 3.4.2 shows the sketch of the simulation setup for a pressure and drag induced power law fluid.

In Figure 3.4.3 the power law viscosity profile in a drag driven flow without the viscous heating effect is shown. With a power law index of 0.5 a pseudo plastic behaviour can be set. The implementation provides a acceptable viscosity profile which matches the analytical solution with an error below 10%. Equation 3.4.1

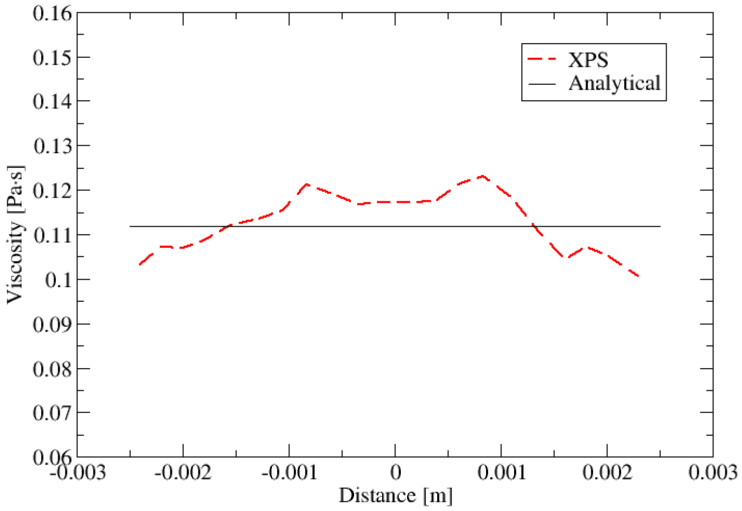

Figure 3.4.3.: Viscosity profile of a non-Newtonian pseudo-plastic drag driven fluid flow.

shows the viscosity model without temperature dependence which had been used for the simulation.

$$\eta = \eta_0 \dot{\gamma}^{(n-1)} \tag{3.4.1}$$

The error is induced by an inaccurate calculation of the shear rate due to particle rearrangement. In Figure 3.4.4 the validation of the power law viscosity in a pressure driven flow is shown. As illustrated it could be shown that the XPS implementation is a very good approximation on the analytical results.

3.5. Viscous heating in Couette flow for Newtonian and Powerlaw fluids

In order to get a more realistic viscosity model, viscosity with exponential temperature dependence was implemented and validated. As a validation for the temperature and shear-dependent viscosity-models, the analytical solutions of Turian et al. [90, 95] had been used. Equation 3.5.1 shows the viscosity model with temperature dependence which had been used for the simulation.

$$\eta = \eta_0 \dot{\gamma}^{(n-1)} \exp\left(-\beta \Theta\right) \tag{3.5.1}$$

A case for the temperature profile between two plates for Newtonian fluids with temperature dependent viscosity and constant thermal conductivity and another

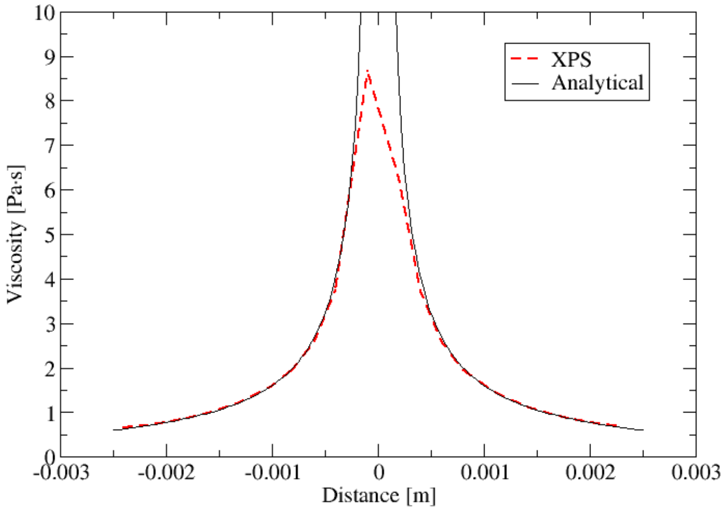

Figure 3.4.4.: Viscosity profile of a non-Newtonian pseudo-plastic pressure driven fluid flow.

x = 0	v_z= 0	T = T_0
x = b	v_z= v_0	T = T_0

ξ= 0	ϵ= 0	Θ= 0
ξ=1	ϵ= 1	Θ= 0

Table 3.5.1.: Boundary Conditions for the channel flow.

one with non-Newtonian fluids had been analysed. The analytic solutions were coded in C++ and the results compared with results of approved studies.

In Table 3.5.1 the boundary conditions of this model are shown. The hight b is 0.005 m, the upper plate velocity v is 0.1 [m/s] , the temperature T , the reference temperature T_0 is 273 K, the dimensionless rectangular coordinate ξ is $\frac{x}{b}$, the dimensionless temperature rise Θ is $\frac{(T-T_0)}{T_0}$ and the dimensionless velocity rise Couette flow ϵ is $\frac{v_z}{V}$. The dimensionless temperature is evaluated at the reference temperature. For the solution, a dimensionless velocity and also dimensionless coordinates had been used. The Results of this chases will be discussed in section 3.5.1 and 3.5.2

3.5.1. Newtonian fluids with exponential temperature dependent viscosity and constant thermal conductivity

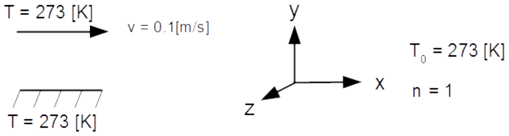

Figure 3.5.1.: Sketch of the simulation setup for a power law viscosity in a Couette flow.

In Figure 3.5.1 a sketch of the simulation setup can be seen.

Turian et al. [95] developed an analytic solution for the temperature profile for drag induced Couette flow of Newtonian fluids within two infinite long parallel plates. Therefore heating effects related to viscous dissipation are taken into account. Additionally the temperature dependence of the viscosity and also the thermal conductivity are included. This analytical solution was compared with data of experimental flow curves which are in good accordance. As validation model viscosity with exponential temperature dependence and constant thermal conductivity had been analysed. This case is very important because usually the impact of thermal conductivity with temperature is minor. The C++ code for the non-Newtonian case is attached in the appendix.

Solution: In Figure 3.5.2-3.5.4 the analytical velocity, temperature and viscosity profiles are matched against the solutions of the XPS-implementation. As illustrated, all profiles (Velocity, Temperature and Viscosity) are in very good accordance with an error under 1%.

3.5.2. Non-Newtonian fluids with temperature dependent viscosity and thermal conductivity

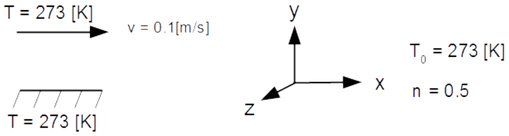

Figure 3.5.5.: Sketch of the simulation setup for a power law viscosity in a Couette flow.

In Figure 3.5.5 a sketch of the simulation setup can be seen.

Another analytic solution given by Turian et al. [90] based on the previous study including Newtonian fluids with temperature dependent viscosity and thermal

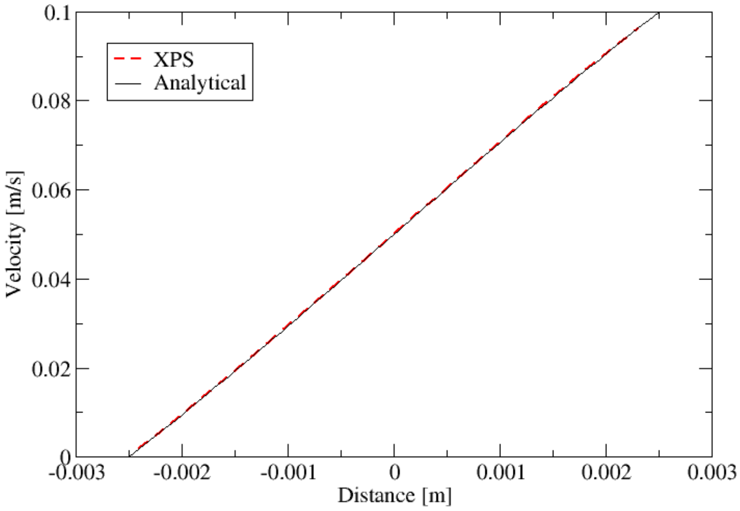

Figure 3.5.2.: Velocity profiles for Newtonian fluids with temperature dependence.

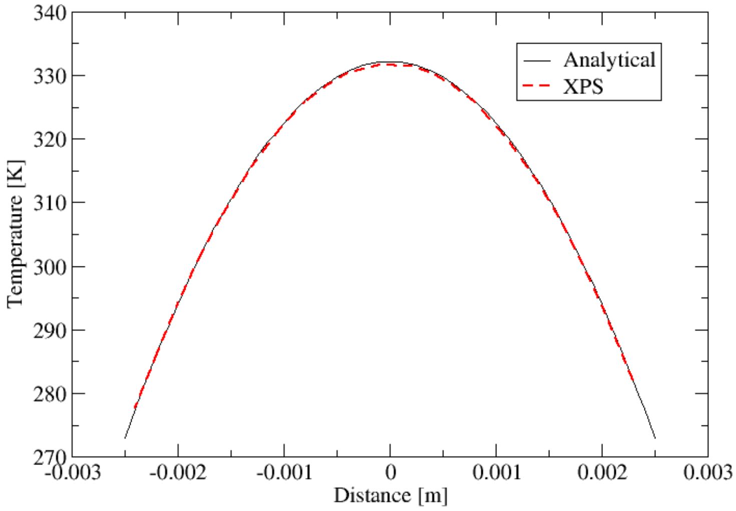

Figure 3.5.3.: Temperature profiles for Newtonian fluids with temperature dependence.

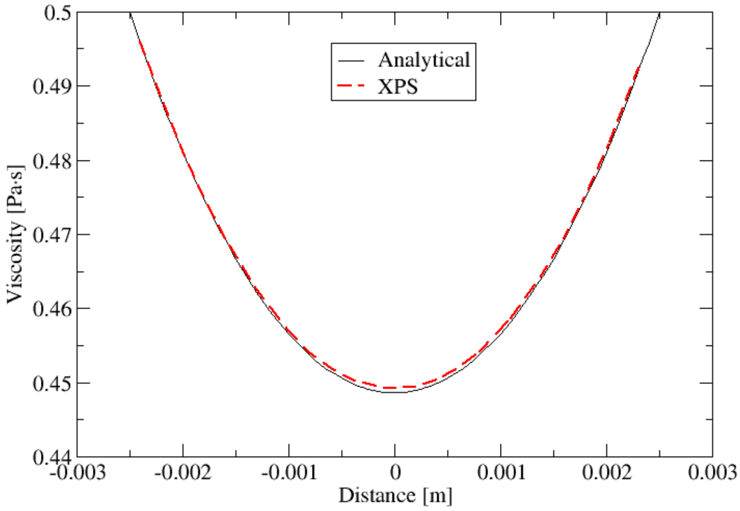

Figure 3.5.4.: Viscosity profiles for Newtonian fluids with temperature dependence.

conductivity had been carried out for non-Newtonian, power law fluids. For the analytical solution a perturbation model had been used. In order to cover a wide range of applications, both, Newtonian and non-Newtonian fluids are very relevant. Empirical rheological models including temperature dependence had been considered. The C++ code for the non-Newtonian case is attached in the appendix.

Solution: In Figure 3.5.6-3.5.8 the analytical velocity, temperature and viscosity profiles are matched against the solutions of the XPS-implementation. As illustrated, the velocity and viscosity profiles are in very good accordance with an error under 1%. The temperature profile is over predicted with an maximal error under 10%.

3.6. Back flow characteristics

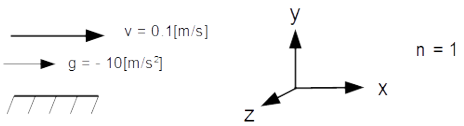

Figure 3.6.1.: Sketch of the back flow simulation setup for a Newtonian fluid.

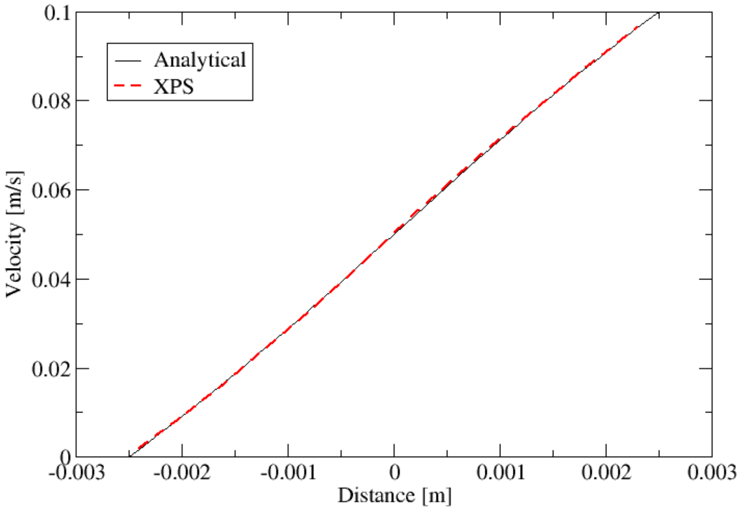

Figure 3.5.6.: Velocity profiles for non-Newtonian fluids with temperature dependence.

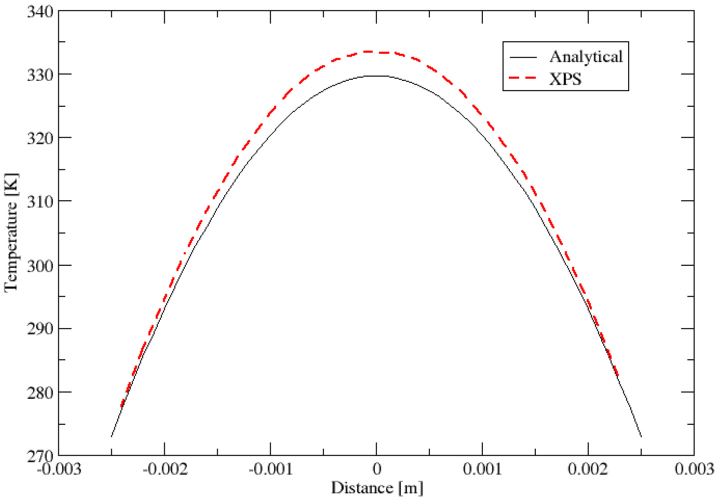

Figure 3.5.7.: Temperature profiles for non-Newtonian fluids with temperature dependence.

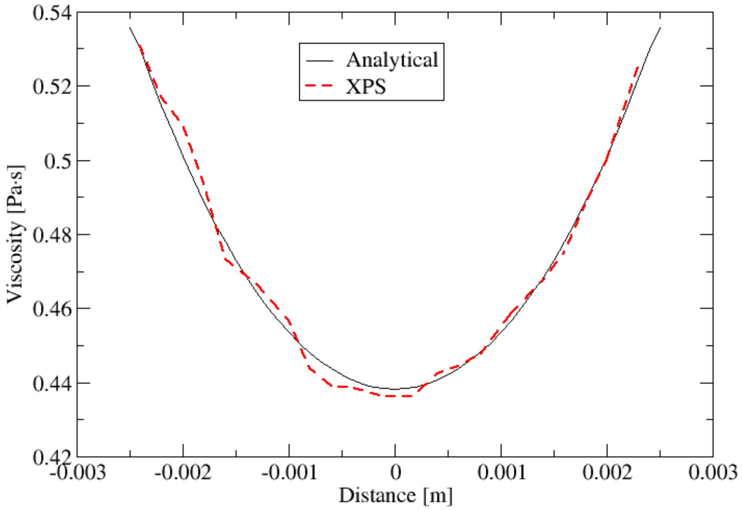

Figure 3.5.8.: Viscosity profiles for non-Newtonian fluids with temperature dependence.

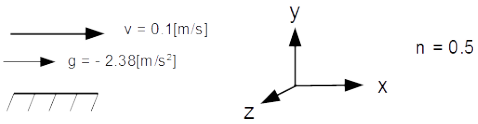

Figure 3.6.2.: Sketch of the back flow simulation setup for a non-Newtonian fluid.

A sketch of the simulation setup for the back flow for a Newtonian fluid can be seen in Figure 3.6.1. Figure 3.6.2 shows the sketch of the simulation setup of the back flow for a non-Newtonian fluid. The back flow is induced by a negative body force in the x-direction.

In Figure 3.6.3 - 3.6.4 the back flow phenomenon occurring in extrusion for a Newtonian and a non-Newtonian fluid are illustrated. As expected the profiles show a negative velocity up to an certain extent in order to provide proper filling.

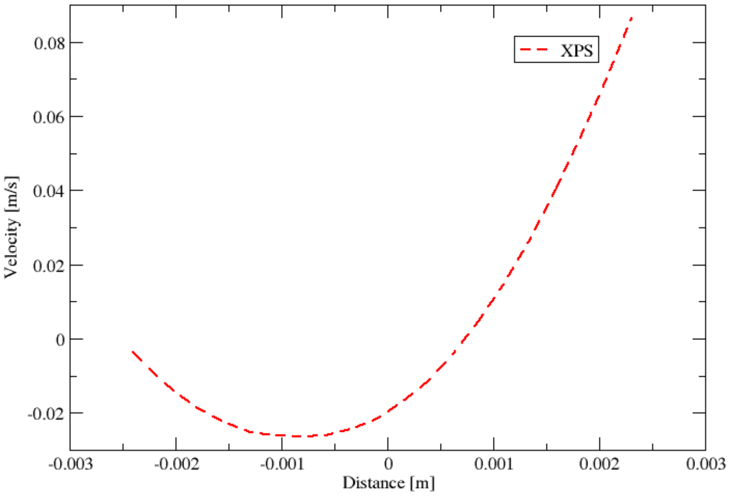

Figure 3.6.3.: Velocity profile of the Couette-Poiseuille-backflow for Newtonian fluids.

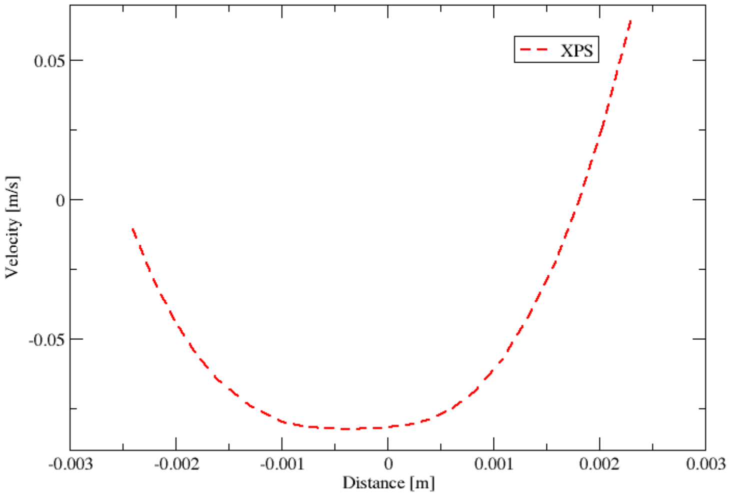

Figure 3.6.4.: Velocity profile of the Couette-Poiseuille-backflow for non-Newtonian fluids.

4

Chapter 4.

Simulation details

4.1. Geometries, materials and operating conditions

In this section geometries and most importing setting parameters, that had been used for the cylinder and extruder simulations are listed.

4.1.1. Geometries:

Geometry 1

This geometry represents two intermeshing, double flighted conveying elements. In Table 4.1.1 the geometry properties are listed. In Figure 4.1.1 the geometry used for the extruder simulation and in Figure 4.1.2 Detail 1, illustrating the gap can be seen.

Geometry 2

In order to calculate the local heat-up rate a more simple geometry had been used. Instead of the double flighted conveying screw elements two simple rotating cylinders had been created. The geometry parameters for the cylinder case can be seen in Table 4.1.2.

4.1.2. Materials:

The material properties have to be set in the MaterialDatabase_Extruder.xpsx file in order to correctly perform the simulations. In Table 4.1.3 the material parameters for a general Newtonian material are shown.

In order to provide a non-Newtonian material the power-law index has to be changed. The material characteristics of Soluplus, which can be described with

Screw diameter D_0	60 mm
Inner screw diameter D_i	38 mm
Centerline distance C	50 mm
Gap between screw and barrel	0.5 mm
Pitch L	60 mm

Table 4.1.1.: Geometry parameters of the conveying element in HME.

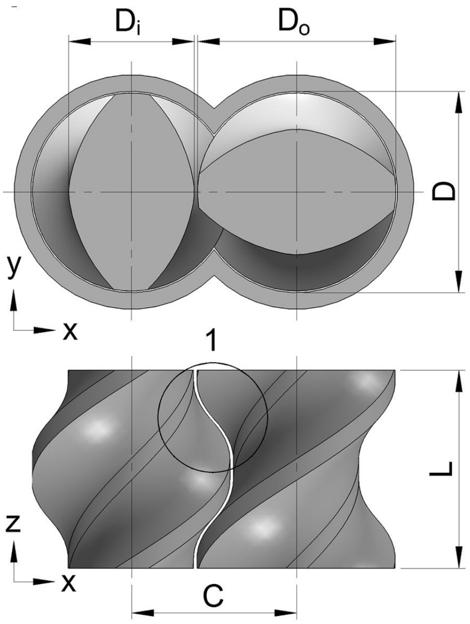

Figure 4.1.1.: Geometry of an double flighted intermeshing conveying element and within a barrel [11].

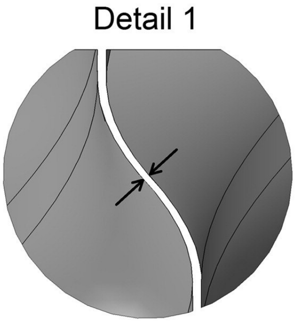

Figure 4.1.2.: Detail 1 of the conveying element displaying the gab of 0.5mm between the extruder screws [11].

Cylinder diameter D_i	38mm
Centerline distance C	50 mm
Pitch L	60 mm

Table 4.1.2.: Geometry parameters of the rotating cylinders.

Dynamic viscosity η	1.0 Pas
Density ρ	1000 kg/m^3
Initial density ρ_{init}	1050 kg/m^3
Mass m	1.329146e-7 kg
Power-law index n	1
Spacing ratio $h/\Delta x$	1.2
Background pressure ρ_0	500 Pa
Heat capacity c_p	2000 J/(kgK)
Heat conductivity κ	0.3 W/(mK)
Reference temperature T_0	443.15 K
Dimensionless viscosity temperature coefficient β	0.002
Particle spacing $\triangle x$	0.5 mm
Smoothing length h	0.6 mm

Table 4.1.3.: Material parameters used in the simulation.

Body force	0 0 0 m/s^2
Particle temperature	436 K
Time step	1e-5 s
Screw temperature boundary	Zero heat flux
Screw rotation	-60 rpm
Barrel temperature	373 K

Table 4.1.4.: Simulation settings used in the simulation of the extruder.

a power-law index of 0.5846 had been used for the simulations of non-Newtonian fluids.

4.1.3. Simulation setting:

The simulation parameters have to be set in the xps.config file. In Table 4.1.4 some simulation settings, which had been used for the extruder simulation are shown.

For the simulation of the cylinder, the config file was changed as listed in Table 4.1.5.

The body force acting on the particles can be set for x, y, z directions. In order to

Body force	0 0 0 m/s^2
Particle temperature	373 K
Time step	5e-6 s
Screw temperature boundary	Zero heat flux
Screw rotation	-600 rpm
Barrel temperature	373 K

Table 4.1.5.: Simulation settings used for the cylinder simulation.

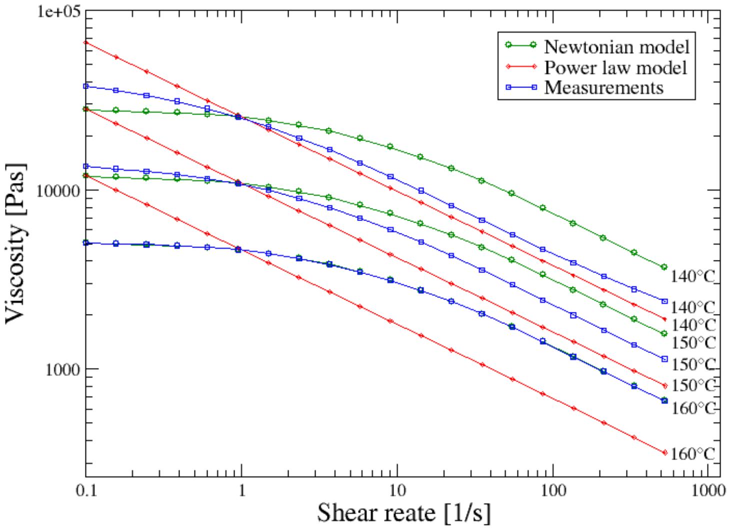

Figure 4.1.3.: Comparison of the viscosity models and experimental data of Soluplus at 140, 150 and 160°C.

simulate a zero throughput characteristic for Newtonian temperature independent fluids in extrusion, the body force has to be set to 25 m/s^2 in the negative z-direction, as presented by Eitzlmayr et al. [11]. For the cylinder simulation no body force was added and the screw rotation speed was increased by a factor of 10.

4.1.4. Master curve

In Figure 4.1.3 the master curve can be seen. For this case Geometry 1 had been used. Here the power law model is compared with a temperature dependent Newtonian model and measurement data for different temperatures. The measurements of Soluplus had been carried out at RCPE. A logarithmic relation of the viscosity and shear rate had been used for the evaluation. The models had been fitted to a viscosity at a shear rate of 1 s^{-1}. In Eq. 4.1.1 the viscosity model developed by Turian et al. [95] used for the simulation can be seen. By setting $\beta = 0$, a temperature independent viscosity can be obtained. The Newtonian model contains a power law exponent of 1, resulting in a Newtonian temperature dependent fluid flow behaviour.

$$\eta = \eta_0 \dot{\gamma}^{(n-1)} \exp\left(-\beta \Theta\right) \tag{4.1.1}$$

As illustrated in Figure 4.1.3 this power law model is a acceptable method to quantify shear thinning temperature dependent fluids. It also provides a temperature dependent viscosity model for Newtonian fluids, by just setting the power law exponent to 1. The measurements had been carried out with a rheometer

MCR301 for Soluplus at RCPE. The accuracy could be improved by using a more sophisticated viscosity model.

4.1.5. Hardware and computational time

In this section the hardware, which had been used for the simulation and the computational times are listed in Table 4.1.6 - 4.1.8. The simulations had been run locally and on two DLAs, equipped with different GPUs. For the simulations a Geforce GTX 670, a Geforce GTX Titan X, a Geforce GTX Titan Black and a Geforce GTX 1080 had been used. A more detailed description about test case 1-6 can be read in section 5.3.

Channel flow simulation

Channel flow	Simulation time [s]	Physical time [s]	GPU
Poiseuille flow	< 60	0.03	GTX 670
Couette flow	< 60	0.03	GTX 670
Heat conduction	60 s	1	GTX 670
Viscous heating 1	1140	1	GTX 670
Viscous heating 2	3720	3	GTX 670

Table 4.1.6.: Computation time of the channel flow simulations.

Cylinder simulation

Cylinder	Simulation time [s]	Physical time [s]	GPU
Heat-up Newtonian	4081	5	GTX Titan Black
Heat-up non-Newtonian	4119	5	GTX Titan Black

Table 4.1.7.: Computation time of the cylinder simulations

Extruder simulation

Extruder	Simulation time [h]	Physical time [s]	GPU
Case 1	507	61.9	GTX Titan Black
Case 2	457	54.8	GTX Titan Black
Case 3	504	62.9	GTX Titan Black
Case 4	301	65.8	GTX Titan 1080
Case 5	361	100	GTX Titan X
Case 6	167	42.1	GTX Titan X
Frozen sim. approach	171	40	GTX Titan Black

Table 4.1.8.: Computation time of the extruder simulations.

The extruder simulation took 1 - 3 weeks until a steady state solution had been calculated, illustrated in Table 4.1.8. Based on this findings, a simulation over physical time relation had been evaluated.

GPU	Release	Simulation time / Physical time
GTX Titan Black	18.2.2014	8.2
GTX Titan X	17.3.2015	4.2
GTX Titan 1080	10.3.2017	3.6

Table 4.1.9.: Development of the GPU performance.

Table 4.1.9 shows that the development of the GPU technology since 2014 led to a reduction of the computational time by a factor more than 2.

5 Chapter 5. Results

In this section the outcome of the simulations will be discussed for Newtonian and non-Newtonian fluids in the conveying element of an extruder used in HME regarding temperature, throughput and pressure characteristics. Furthermore the heat-up rate which had been simulated with geometry 2 will be discussed.

5.1. Heat-up rate

In order to simulate the viscous heat generation, geometry 2 consisting of two co-rotating cylinders within a barrel had been used. The barrel walls were set to 373 K and for the temperature of the cylinders zero heat flux boundaries had been used. The reference temperature had been set to 373 K. For the purpose of capturing non-Newtonian fluid flow behaviour, Soluplus had been used as material and the screw rotation speed was set to 600 rpm. In Figure 5.1.1 a qualitative view of the contour plot of the local heat up rate initiated by viscous heating can be seen. As expected the heat generation has its maximum at the screw-screw interface, where two opposed fluid flow directions are present. At the screw-barrel interface the flow direction is uniform, therefore about half of the amount of the shear rate is present, leading to lower viscous heat generation, illustrated in figure 5.1.2.

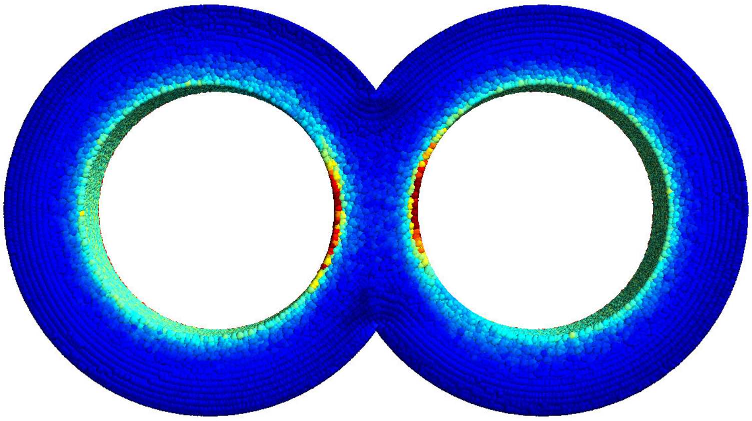

Figure 5.1.1.: Qualitative post view of the heat generation in rotating cylinders.

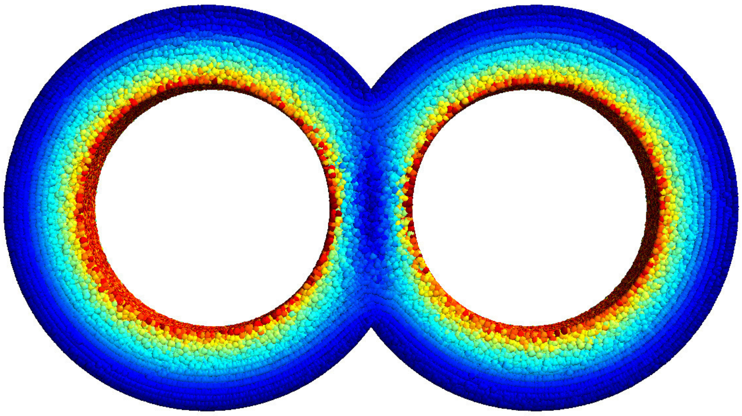

Figure 5.1.2.: Qualitative post view of the velocity of the particles in rotating cylinders.

5.2. Pressure characteristics

Dimensionless numbers such as the pressure gradient, power and throughput for screw machines had been examined extensively. Kohlgrüber [18] presented the quantities, which are necessary to predict the pressure generation and energy behaviour in extrusion:

- Dimensionless pressure gradient:

$$\triangle\rho^{*} = \frac{\triangle\rho}{\eta n}\frac{D}{L} \tag{5.2.1}$$

- Dimensionless power:

$$P^{*} = \frac{P}{\eta n^{2} D^{2} L} \tag{5.2.2}$$

- Dimensionless throughput:

$$\dot{V}^{*} = \frac{\dot{V}}{n D^{3}} \tag{5.2.3}$$

with $\dot{V}$ as the dimensionless throughput, n as the rotational speed, $\triangle p$ as the pressure difference, P as the power, D as the barrel inner diameter, L as the screw length and η as the viscosity. For further calculations, also the centreline distance C and the clearance between the screw-screw and screw-barrel interface are taken into account. Pawlowski et al. [96] presented the kinematic flow equation $\mathit{\Lambda}$ which can be seen in Eq. 5.2.4.

$$\mathit{\Lambda} := \frac{\dot{V}}{A_1 n D^{3}} \tag{5.2.4}$$

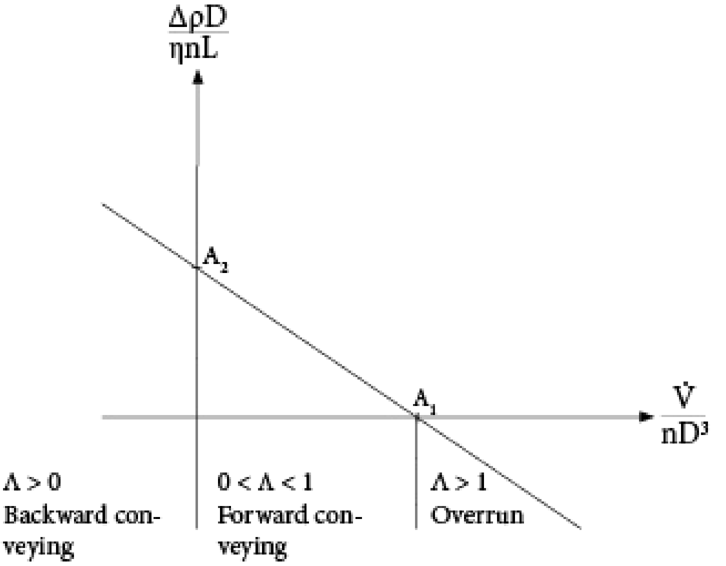

Figure 5.2.1.: Pressure characteristic and throughput in extrusion.

$$\frac{\triangle pD}{\eta nL} = A_2(1 - \mathit{\Lambda}) \tag{5.2.5}$$

A_1 defines the maximum throughput, where no pressure is present and A_2 defines a zero-throughput characteristic. A backward conveying screw is characterised with a kinematic flow parameter $\mathit{\Lambda} < 0$, whereas $0 < \mathit{\Lambda} < 1$ defines the throughput regime of an conveying element and $\mathit{\Lambda} > 1$ is typical for a overrun screw, see Figure 5.2.1.

Based on the work of Eitzlmayr et al. [97] the pressure characteristics of viscous, temperature dependent Newtonian fluid flows had been examined. In Figure 5.2.2 the comparison of the results of an FVM simulation for a Newtonian temperature independent fluid realised by Bierdel et al. [98] and the results of the simulation of an conveying element carried out in this thesis can be seen. By applying the same simulation settings for temperature independent fluids the A2-point is over predicted by 10 % with the SPH approach. This error could arise due to different simulation settings such as the rpm for the screws or slightly different geometries that had been used. Bierdel used a rotational speed per minute of 95. Another explanation would suggest that without a gap model the SPH simulation could generate an error. With the SPH approach a 1-particle-layer is used for narrow regions like the screw-screw or the barrel-screw interface. This could cause an inaccurate calculation due to an inadequate particle distribution. Eitzlmayr et al. [11] had developed a gap model, which could resolve the correct velocity distribution for a single particle layer in the clearance for Newtonian fluids. The model is not available for non-Newtonain fluids at the moment and is not implemented in the current version of SPH. For temperature dependent fluids, backward conveying characteristics will appear with a body force as used in the temperature independent SPH simulations. Eitzlmayr suggested a body force of 25 m/s^2 in

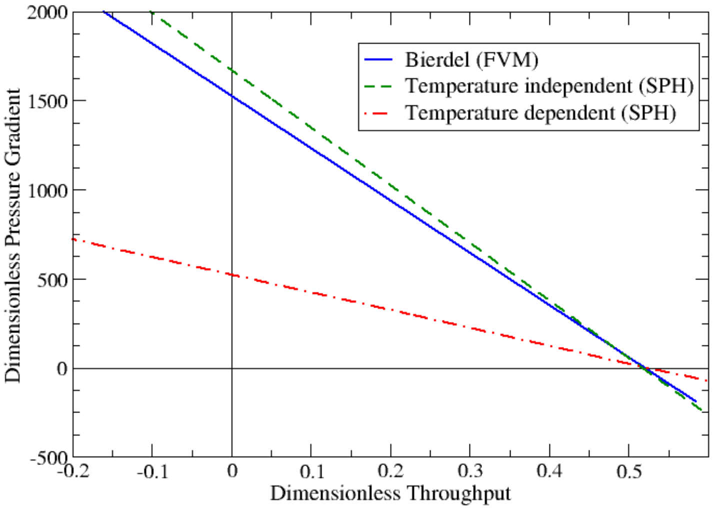

Figure 5.2.2.: Pressure characteristics of the conveying element.

the negative z-direction to generate a zero throughput behaviour, which can be seen in the A2-point. If the fluid is temperature dependent, the viscosity will decrease when the temperature rises, leading to higher velocities and a change in the pressure characteristics. It had been found that the temperature has minor influence on the pressure characteristics in the A1 point. Furthermore it could be shown that a pressure number of 550 will adjust at the zero throughput A2-point, if a body force of 5 m/s^2 in the negative z-direction will be set for a temperature dependent Newtonian fluid.

5.3. Temperature characteristics

In this section the results of the velocity, temperature and viscosity calculations for fluids in the conveying element of an twin screw extruder will be discussed. For that purpose simulations with and without back pressure, with temperature dependence and with temperature independence had been carried out.

Zero heat flux boundaries had been set for the screws. The initial temperature was set to 433.15 K and the barrel temperature was fixed at 373 K. To spare computational time a dynamic viscosity of 1 Pas had been used for the simulation. Eitzlmayr et al. [99] showed that in extruders highly viscous materials ranging from 10^2 - 10^3 Pas are present. Furthermore he presented that in co-extrusion the creeping flow regime is obtained with Re $<$ 10. In Equation 5.3.1 the calculation of the Reynolds number in extrusion can be seen. By setting the viscosity to 1, a Re-number of 3.72 is obtained.

Case	Modification
1	Newtonian fluid with temperature independence, without back pressure
2	Newtonian fluid with temperature dependence, without back pressure
3	Newtonian fluid with temperature independence, with back pressure
4	Newtonian fluid with temperature dependence, with back pressure
5	Non-Newtonian fluid with temperature independence, without back pressure
6	Non-Newtonian fluid with temperature dependence, without back pressure

Table 5.3.1.: Modifications of the test cases 1-6.

$$Re = \frac{nD^2\rho}{\eta} \tag{5.3.1}$$

For creeping flows the dependence of the Re-number on the power characteristics vanishes, which leads to a reduced computational time, but still yields the same flow field behaviour as with higher viscosities, stated by Eitzlmayr et al. [100]

Furthermore, the dissipation term was multiplied with a factor of 4630, so that viscous dissipation is realistic. This factor was deduced from experimental data of Soluplus. The 3-D results of the simulation had been compared with experimental measurements.

Table 5.3.1 shows an overview of the test cases that had been investigated. In Figure 5.3.1 the times to reach steady state for the different test cases are illustrated. In Table 5.3.2 an comparison of the times to reach steady state can be seen, and in Table 5.3.3 minimum, maximum and average temperatures are listed.

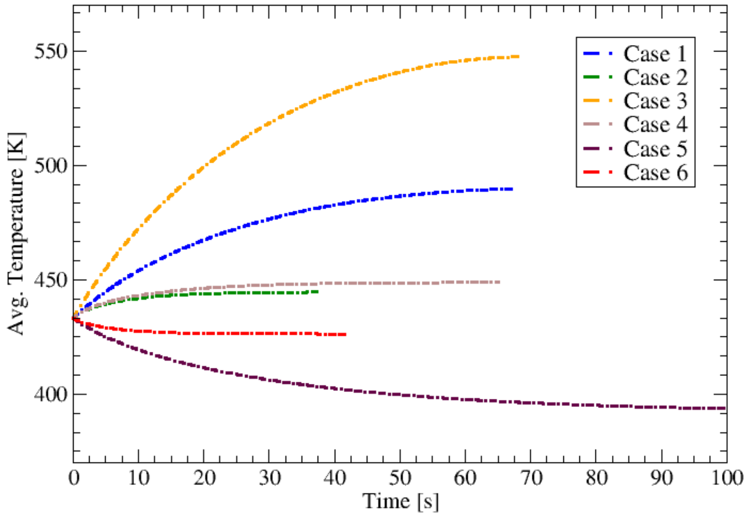

Figure 5.3.1.: Times to reach a steady state temperature distribution of the test cases 1-6.

Case	Time to reach steady state [s]
1	60
2	25
3	65
4	45
5	100
6	20

Table 5.3.2.: Overview of the times to reach steady state.

Case	Min. temperature [K]	Max. temperature [K]	Avg. temperature [K]
1	439.2	574.6	489.784
2	416.7	485.4	444.576
3	453.4	604.4	547.331
4	418.1	457.3	448.802
5	382.6	400.9	393.721
6	434.2	404	426.345

Table 5.3.3.: Minimum, maximum and average temperature of the test cases 1-6.

Case 1: Newtonian fluid with temperature independence and no back pressure

Minimum velocities had been predicted at the barrel wall, illustrated in picture a of Figure 5.3.2. Near the clearance zone the particles show a maximum velocity magnitude of 0.27 m/s. Highest temperatures were observed at the intermehsing zone. For this case a constant viscosity of 1 Pas had been used.

Case 2: Newtonian fluid with temperature dependence and no back pressure

In Picture a of Figure 5.3.3 minimum velocities can be seen at the barrel wall. Near the clearance zone the particles show a maximum velocity magnitude of 0.23 m/s. Picture b of Figure 5.3.4 shows a viscosity ranging from 0.1157 Pas to 4.085 Pas. Minimum viscosity had been calculated at the intermeshing zone and at the screw walls. The highest temperature initiated by viscous dissipation was predicted at the intermeshing zone and at the screw walls after the particles leave the clearance, downstream the screw. This behaviour displays the typical phenomena of a temperature dependent Newtonian viscosity. The fixed temperature at the barrel wall are cooling the system.

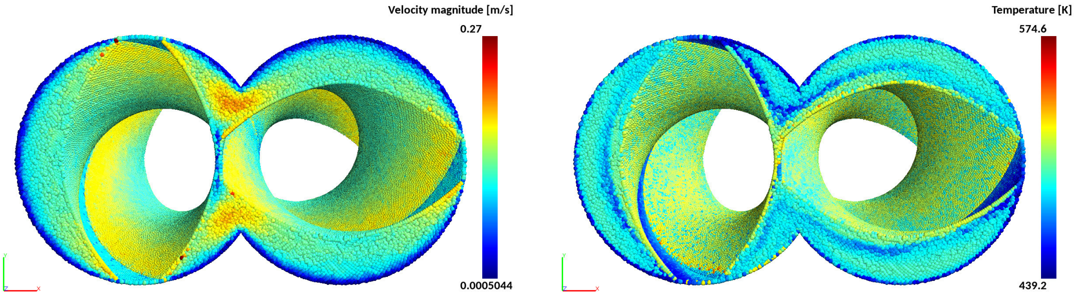
Velocity magnitude [m/s]
0.27
0.0005044
Temperature [K]
574.6
439.2

(a) Velocity profile front view (b) Temperature profile front view

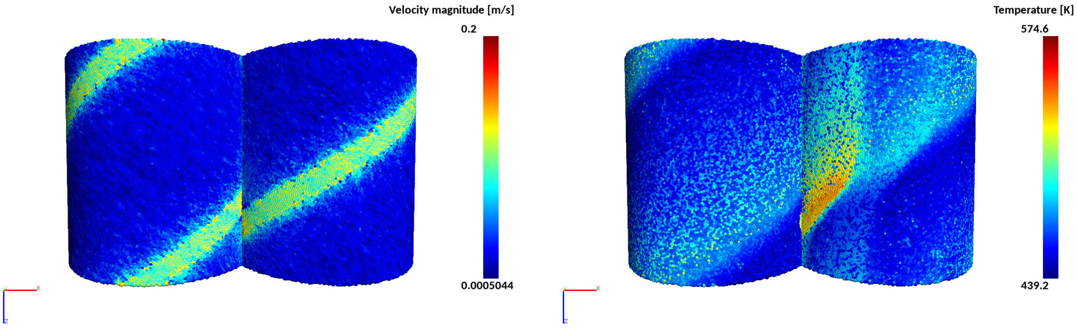
Velocity magnitude [m/s]
0.2
0.0005044
Temperature [K]
574.6
439.2

(c) Velocity profile top view (d) Temperature profile top view

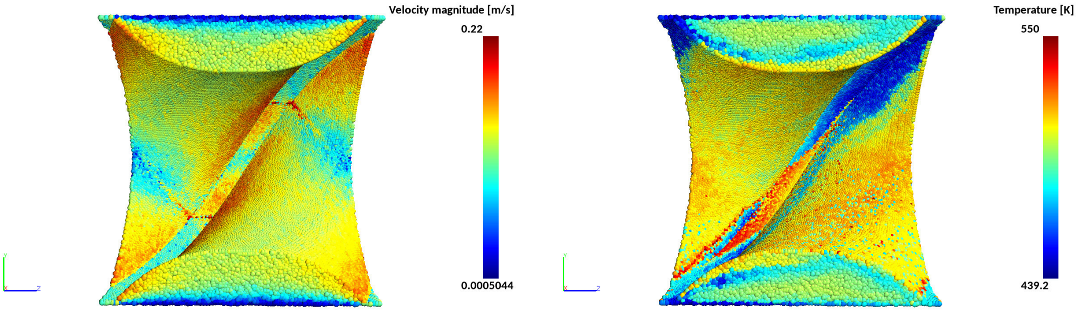
Velocity magnitude [m/s]
0.22
0.0005044
Temperature [K]
550
439.2

(e) Velocity profile side view cut (f) Temperature profile side view cut

Figure 5.3.2.: Velocity and temperature profiles of case 1.

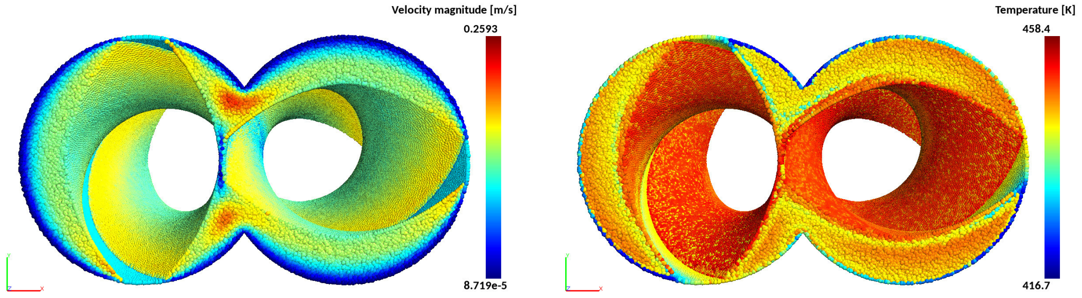
Velocity magnitude [m/s]
0.2593
8.719e-5
Temperature [K]
458.4
416.7

(a) Velocity profile front view (b) Temperature profile front view

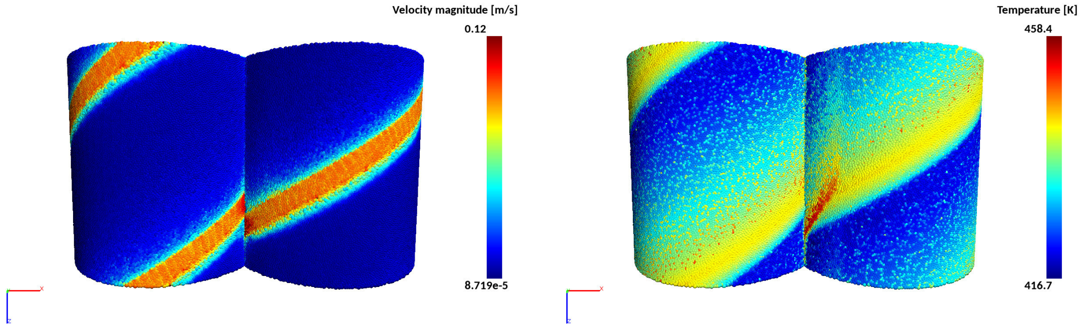
Velocity magnitude [m/s]
0.12
8.719e-5
Temperature [K]
458.4
416.7

(c) Velocity profile top view (d) Temperature profile top view

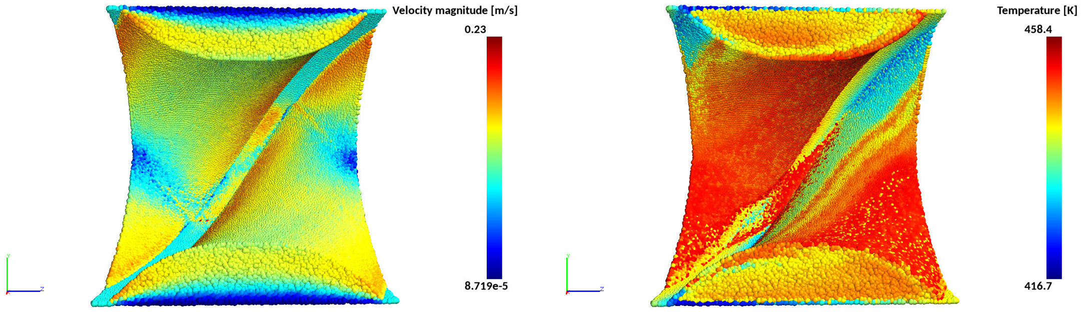
Velocity magnitude [m/s]
0.23
8.719e-5
Temperature [K]
458.4
416.7

(e) Velocity profile side view cut (f) Temperature profile side view cut

Figure 5.3.3.: Velocity and temperature profiles of case 2.

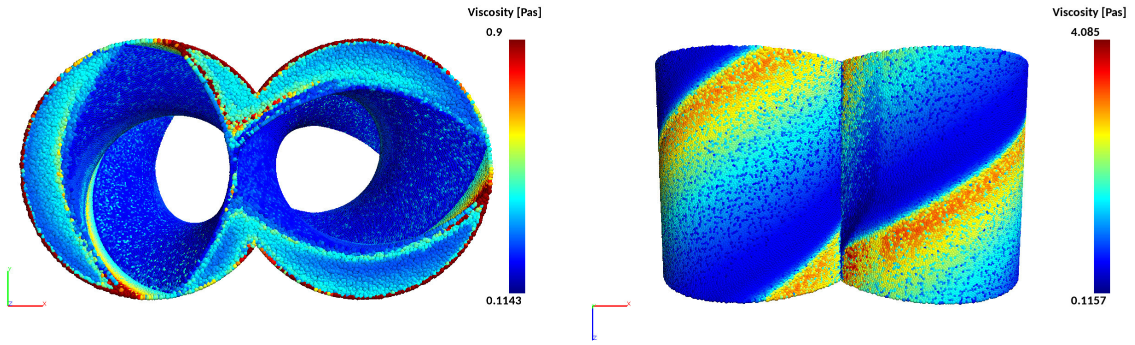

(a) Viscosity profile front view

(b) Viscosity profile top view

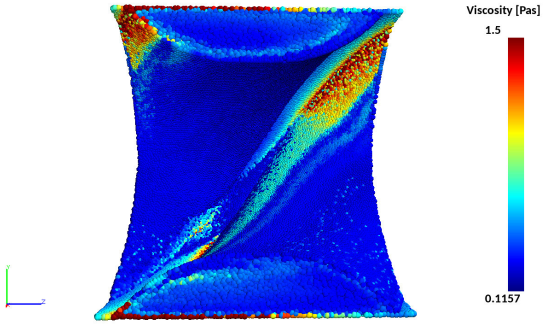

(c) Viscosity profile side view cut

Figure 5.3.4.: Viscosity profiles of case 2.

Case 3: Newtonian fluid with temperature independence and back pressure

The velocity of the melt behaves as in the previous simulations, ranging up to to 0.31 m/s, illustrated in Picture a of Figure 5.3.5. Picture b shows the highest temperatures of 604.4 K at the intermehsing zone and within the barrel-screw channel. For this case a constant viscosity of 1 Pas had been used and a body force of 25 m/s^2 in the negative z-direction was set, inducing higher shear rates, which generate higher temperatures than in the “no back pressure” case for temperature independent Newtonian fluid simulations.

Case 4: Newtonian fluid with temperature dependence and back pressure

The velocity of the melt behaves as in the previous simulations, ranging up to 0.3341 m/s illustrated in Picture a of Figure 5.3.6. Picture a of Figure 5.3.7 shows a viscosity ranging from 0.1012 Pas to 3.8 Pas. Minimum viscosity was calculated at the intermeshing zone and at the screw walls. After the melt had left the intermeshing zone and clearance the highest viscosity was calculated. The highest temperature initiated by viscous dissipation was predicted at the intermeshing

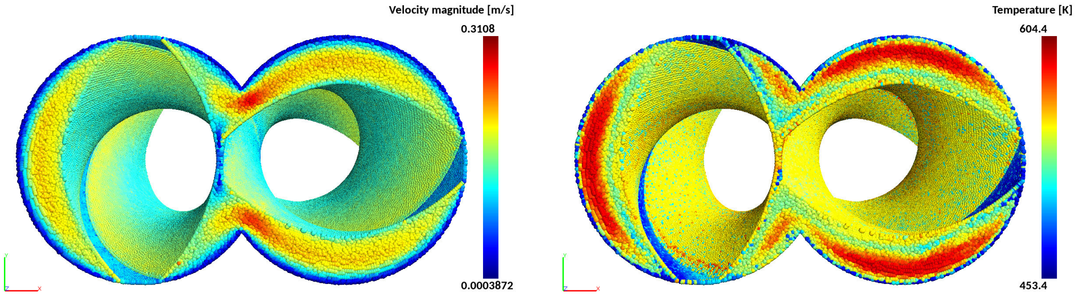
Velocity magnitude [m/s]
0.3108
0.0003872
Temperature [K]
604.4
453.4

(a) Velocity profile front view (b) Temperature profile front view

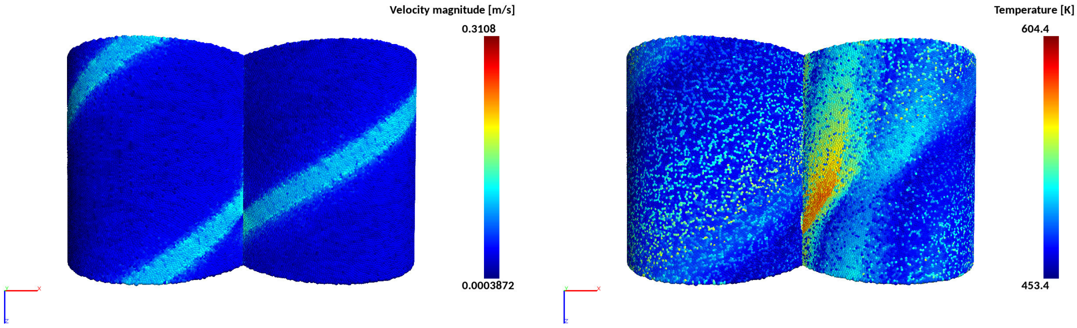
Velocity magnitude [m/s]
0.3108
0.0003872
Temperature [K]
604.4
453.4

(c) Velocity profile top view (d) Temperature profile top view

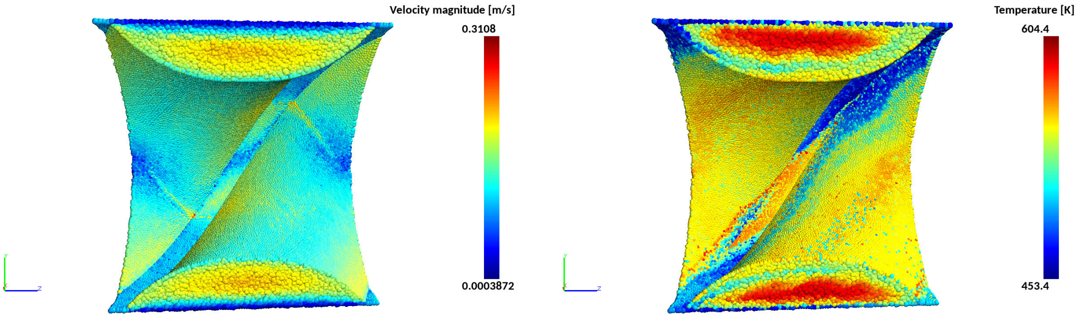
Velocity magnitude [m/s]
0.3108
0.0003872
Temperature [K]
604.4
453.4

(e) Velocity profile side view cut (f) Temperature profile side view cut

Figure 5.3.5.: Velocity and temperature profiles of case 3.

zone and at the screw-barrel channel. Higher temperatures were found compared to the simulation of case 2. This behaviour displays the typical phenomena of a temperature dependent Newtonian viscosity. The fixed temperature at the barrel wall are cooling of the system.

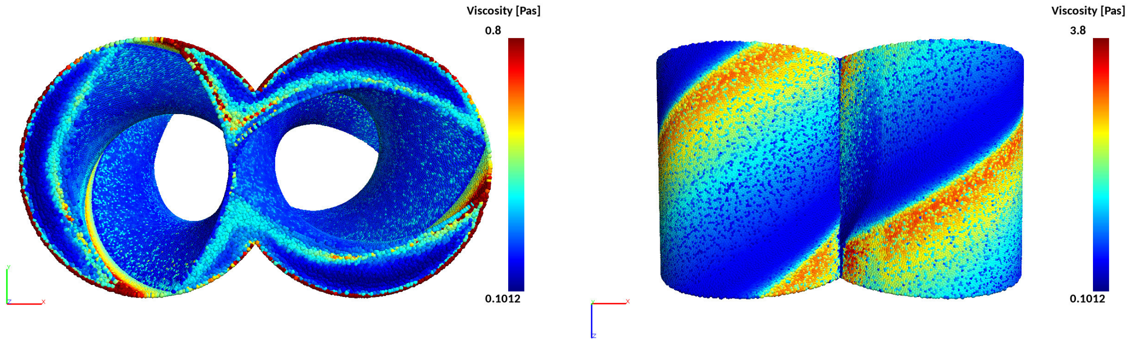

(a) Viscosity profile front view (b) Viscosity profile top view

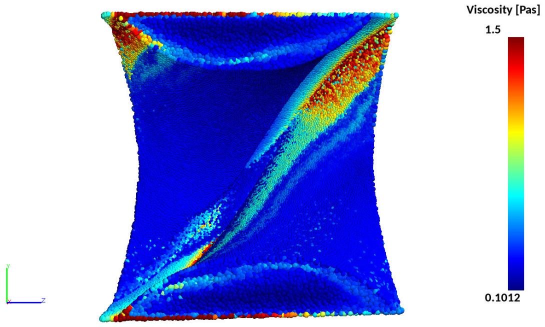

(c) Viscosity profile side view cut

Figure 5.3.7.: Viscosity profiles of case 4 .

Case 5: Non-Newtonian fluid with temperature independence and no back pressure

For this case Soluplus was modelled as non-Newtonian material. The velocity of the melt behaves as in the previews simulations, ranging up to 0.2617 m/s, illustrated in Picture a of Figure 5.3.8. The viscosity decreases with applied shear stress, leading to a lower minimum and maximum viscosity. The lowered viscosity also induces a lowered heat up rate. In Picture a of Figure 5.3.9 a viscosity ranging from 0.07371 Pas to 0.6512 Pas can be seen. The lowest viscosity was predicted in the clearance and at the screw-screw interface. Here highest shear rates are present. The highest viscosity was calculated at the centre of the channel, due to slow relative particle motion and low shear rates. In this set up the temperature will not influence the viscosity leading to the highest temperatures at the screw-barrel channel, induced by a high velocity gradient. The lowest temperatures were calculated at the barrel wall after the particles had left the flight clearance.

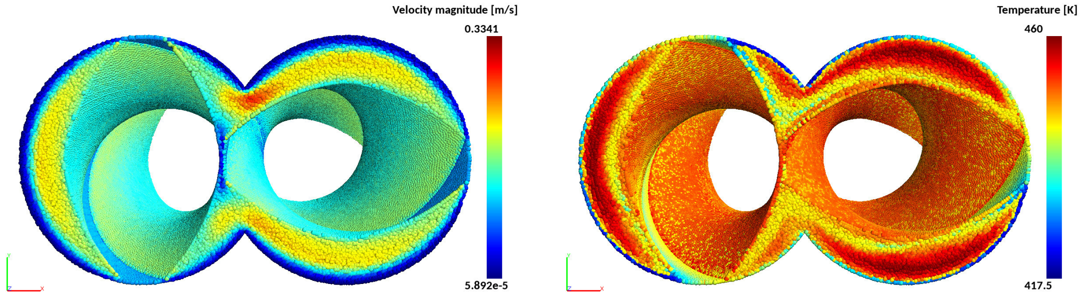
Velocity magnitude [m/s]
0.3341
5.892e-5
Temperature [K]
460
417.5

(a) Velocity profile front view (b) Temperature profile front view

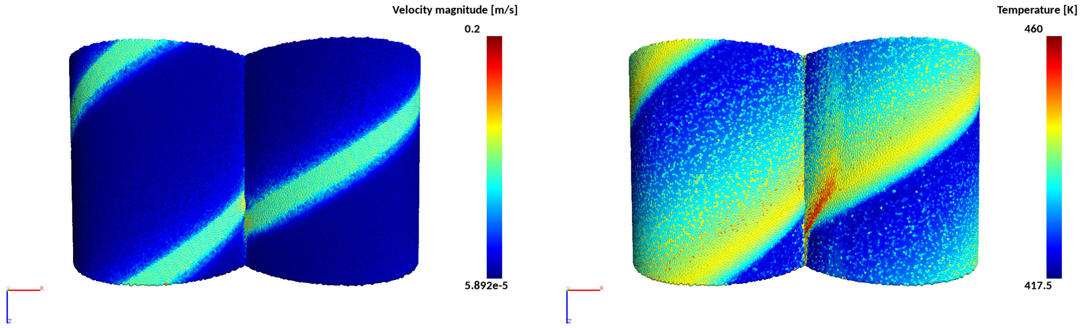
Velocity magnitude [m/s]
0.2
5.892e-5
Temperature [K]
460
417.5

(c) Velocity profile top view (d) Temperature profile top view

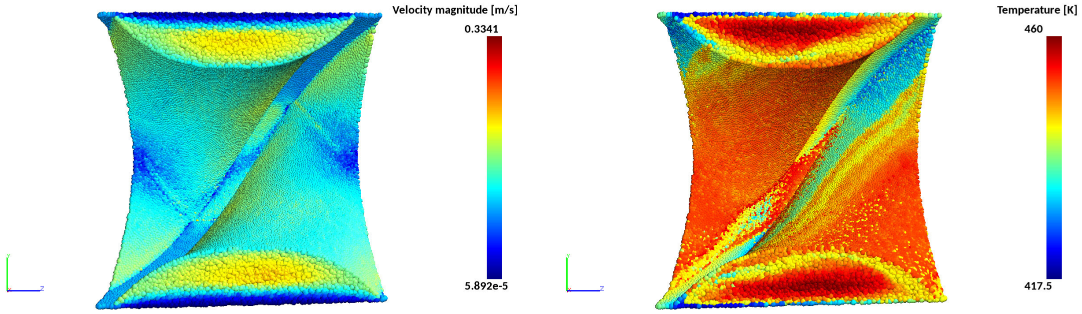
Velocity magnitude [m/s]
0.3341
5.892e-5
Temperature [K]
460
417.5

(e) Velocity profile side view cut (f) Temperature profile side view cut

Figure 5.3.6.: Velocity and temperature profiles of case 4.

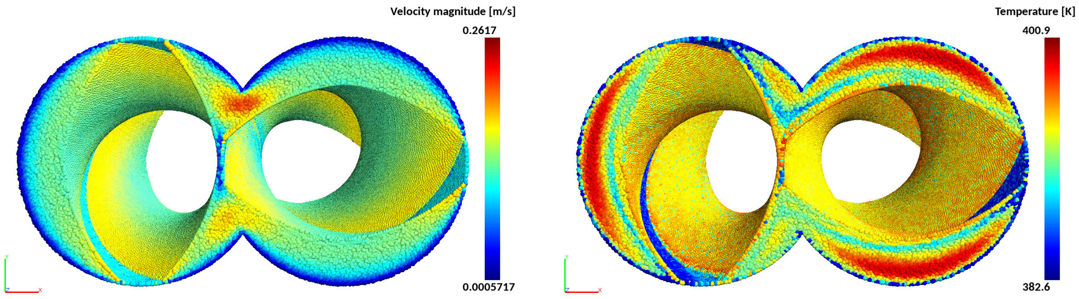
Velocity magnitude [m/s]
0.2617
0.0005717
Temperature [K]
400.9
382.6

(a) Velocity profile front view (b) Temperature profile front view

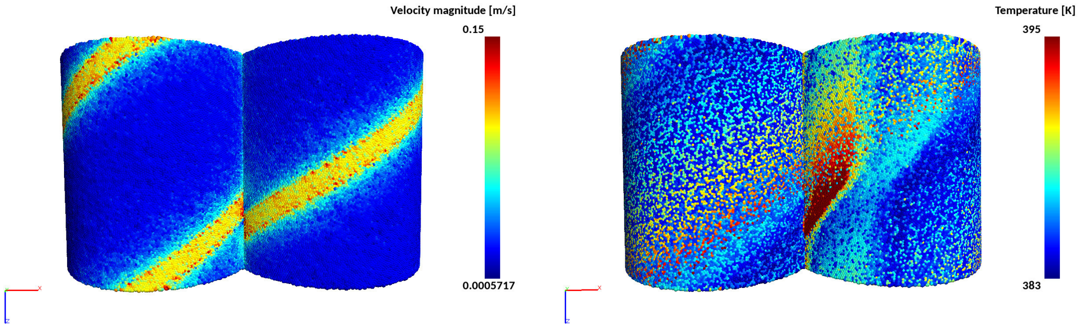
Velocity magnitude [m/s]
0.15
0.0005717
Temperature [K]
395
383

(c) Velocity profile top view (d) Temperature profile top view

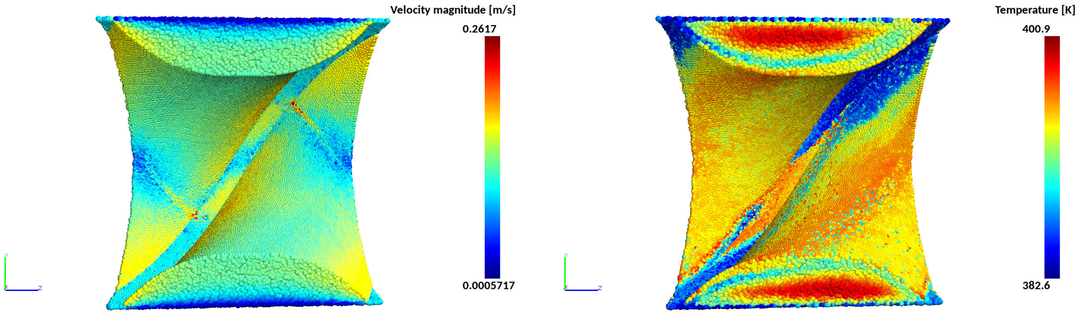
Velocity magnitude [m/s]
0.2617
0.0005717
Temperature [K]
400.9
382.6

(e) Velocity profile side view cut (f) Temperature profile side view cut

Figure 5.3.8.: Velocity and temperature profiles of case 5.

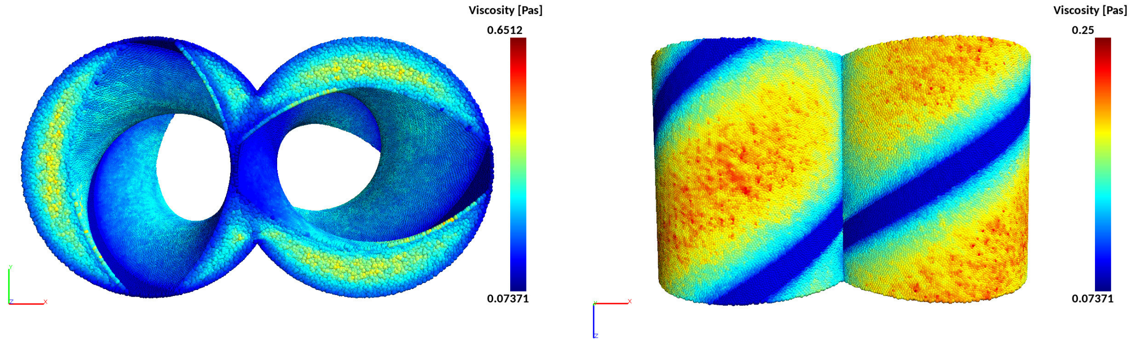

(a) Viscosity profile front view

(b) Viscosity profile top view

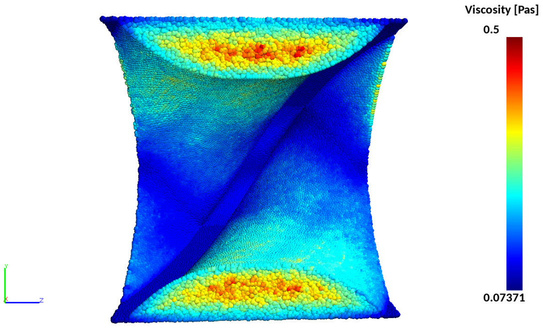

(c) Viscosity profile side view cut

Figure 5.3.9.: Viscosity profiles of case 5.

Case 6: Non-Newtonian fluid with temperature dependence and no back pressure

For this case Soluplus was modelled as non-Newtonian material. Picture a of Figure 5.3.10 shows that the velocity of the melt behaves as in the previews simulations, ranging up to 0.2573 m/s. The viscosity decreases with applied shear stress, leading to a lower minimum and maximum viscosity. Not only the pseudoplastic behaviour, but also the temperature dependence of the viscosity contributes to the decrease in viscosity. Picture b of Figure 5.3.11 shows a viscosity ranging from 0.08263 Pas to 3.424. The lowest viscosity is predicted before the particles enter the flight clearance and at the intermeshing zone. The highest temperatures can be seen at the screw-barrel channel, initiated by a high velocity gradient. The highest viscosity can be found near the barrel wall at the screw-barrel channel, where the lowest temperatures are present. These results demonstrate the influence of shear thinning and temperature dependence on non-Newtonian viscosity. The highest temperatures had be expected at the intermeshing zone. An explanation for the unexpected temperature profiles suggest an inadequte clearance modelling.

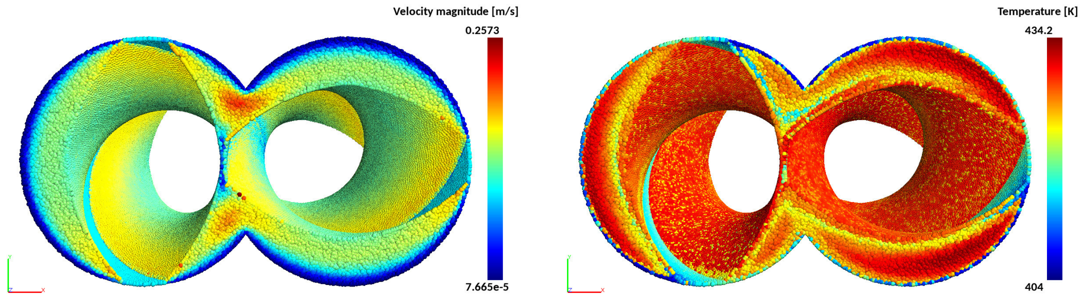
Velocity magnitude [m/s]
0.2573
7.665e-5
Temperature [K]
434.2
404

(a) Velocity profile front view (b) Temperature profile front view

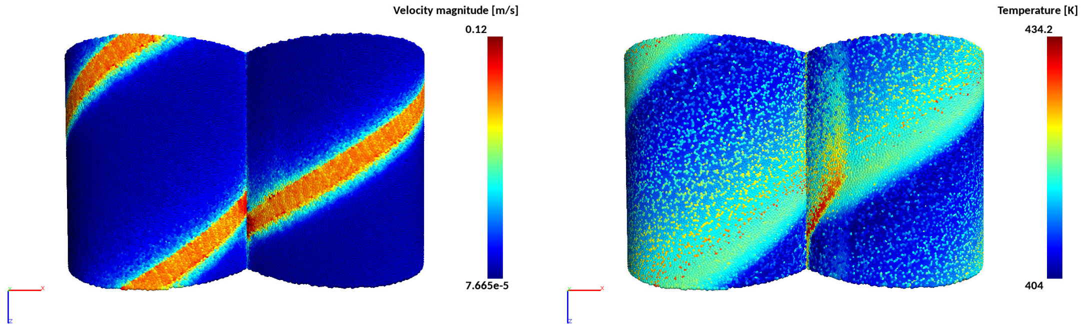
Velocity magnitude [m/s]
0.12
7.665e-5
Temperature [K]
434.2
404

(c) Velocity profile top view (d) Temperature profile top view

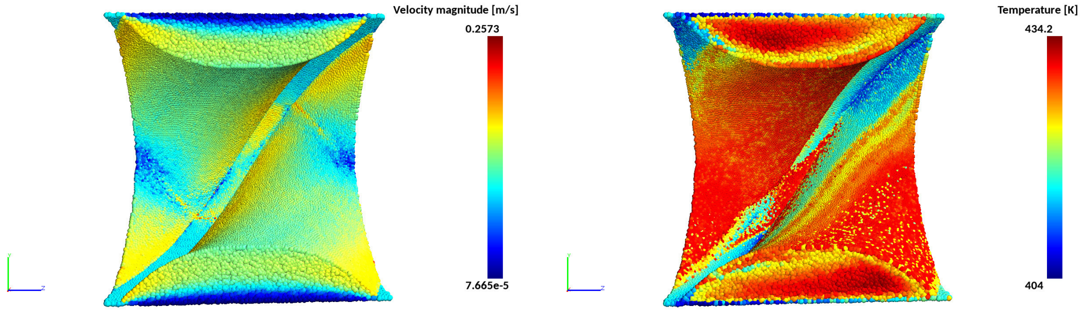
Velocity magnitude [m/s]
0.2573
7.665e-5
Temperature [K]
434.2
404

(e) Velocity profile side view cut (f) Temperature profile side view cut

Figure 5.3.10.: Velocity and temperature profiles of case 6.

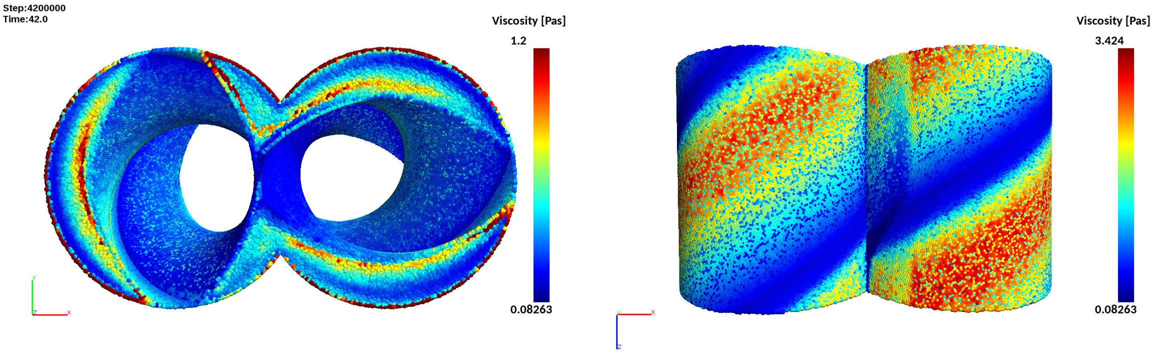

(a) Viscosity profile front view (b) Viscosity profile top view

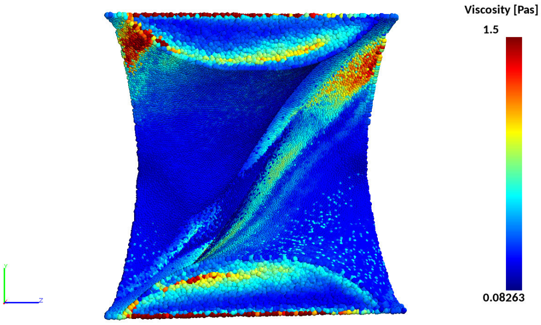

(c) Viscosity profile side view cut

Figure 5.3.11.: Viscosity profiles of case 6.

The temperature dependent fluid shows differences of viscosity and temperature development, compared to the temperature independent fluid. As expected the simulation display the difference of a Newtonian and non-Newtonian fluid regarding velocity, temperature and viscosity. The results imply that the greatest heat generation is related to the highest shear rates. Furthermore the simulations yield different fluid dynamics in extrusion with different viscosity models.

The findings of this thesis are not in exact agreement with CFD temperature simulations of a conveying element presented by Kohlgrüber [18]. He could show a temperature development of the melt ranging from 300°C to 325°C. He predicted the highest temperatures at the screw tips with an increase in temperature of 25°C. The simulations shown by Kohlgrüber were carried out for two revolutions only, which would imply that the temperature field had not yet reached the steady state. Another explanation could be that the distribution for the SPH simulation within the screw-screw interface and the screw-barrel interface is not adequate. At the gaps a 1-layer particle distribution can be simulated at the moment, which could lead to an inaccurate calculation of the temperature distribution. Also different geometries used for the simulation could cause a deviation of the results.

Depending on the material properties, simulation settings and model method, minimum temperatures ranging from 382.6 K to 453.4 K and maximum temperatures ranging from 400.9 K to 604.4 K had been observed with the SPH approach.

As expected the variation in velocity and viscosity for the different test cases could be shown. The highest average temperatures of 547.331 K had been found in the Newtonian, temperature-independent simulations for the A2 point, listed in Table 5.3.3. There, a body force of 25 m/s^2 in the negative z-direction and no decrease in viscosity due to heat is taking place, therefore no reduction of the viscous dissipation will occur. The lowest average temperatures can be observed in the non-Newtonian, temperature-independent simulations of the A1 point. Here no body force is present, and the heat is not contributing to the decrease in viscosity. That behaviour would imply that less viscous dissipation and a lowered heat-up rate compared to case 6 is taking place. Therefore one would expect the lowest average temperature in case 6. As the initial temperature is higher then the maximum average temperature in the system, the viscosity will increase instead of dropping. This effect leads to higher shear rates and a higher maximum average temperature in the temperature dependent case 6 compared to the temperature independent case 5.

Figure 5.3.12 shows a comparison of case 2 and case 6. Picture a and c display the lowest viscosity, whereas in b and d the highest temperatures can be seen.

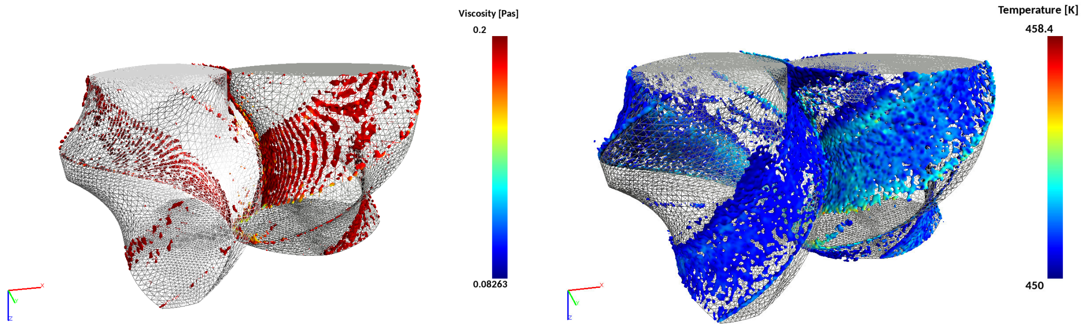

(a) Viscosity profile front view of case 2 (b) Temperature profile front view of case 2

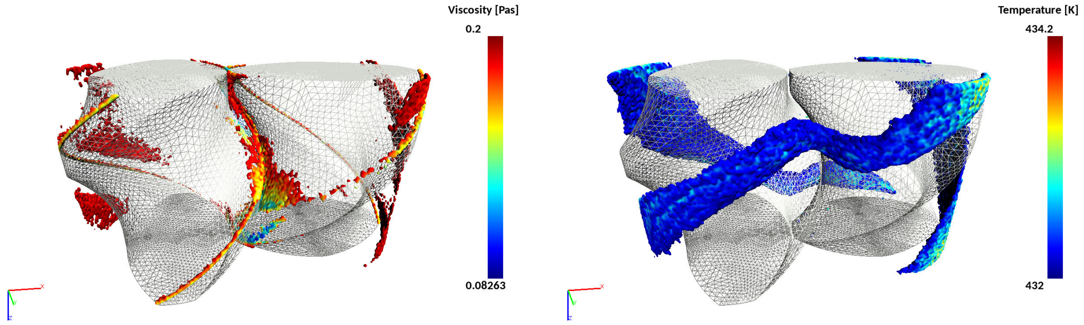

(c) Viscosity profile top view of case 6 (d) Temperature profile top view of case 6

Figure 5.3.12.: Lowest viscosity and highest temperature of case 2 and case 6.

The confrontation of both cases illustrate the variation in temperature and viscosity of the temperature dependent Newtonian fluid and the temperature dependent shear thinning non-Newtonian fluid. The models predict a different magnitude of viscosity and temperature. Moreover the heat generation will take place at dif-

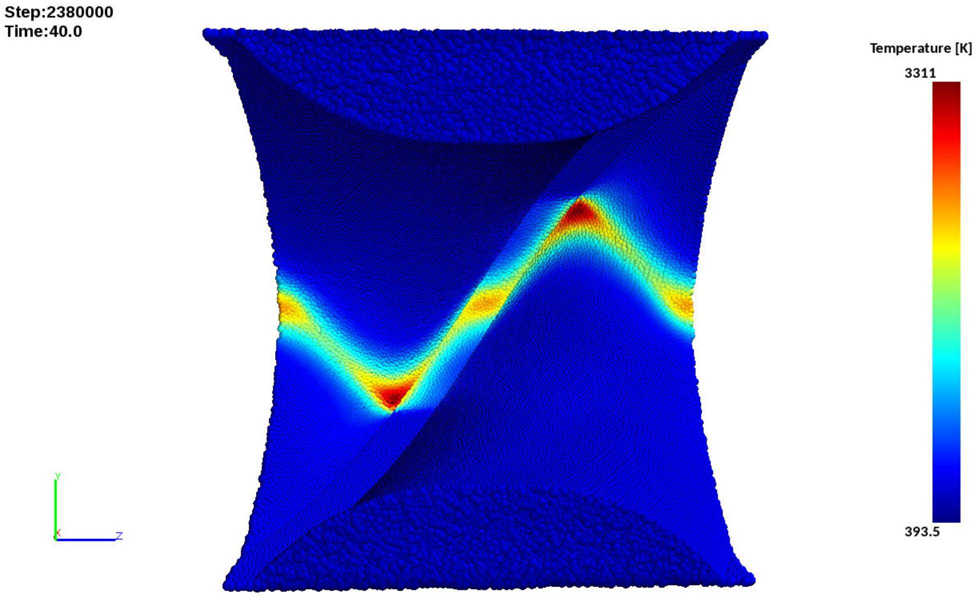

Figure 5.4.1.: Post view of the heat generation in rotating cylinders.

ferent positions within the device. This results indicate that in order to generate a correct temperature distribution in CFD for complex geometries as in HME a deep understanding and precise handling of viscosity related models has to be considered.

5.4. Frozen Simulation approach

An frozen simulation approach to spare computational time had been set up and tested. The basic idea was to calculate the velocity field first, and once steady state for the velocity field was reached the same simulation had been reinitialised without the momentum equations turned on. Once the momentum equation had been turned off, the temperature could bee calculated with stationary particles. After a couple of seconds the momentum equation had been reintroduced and then turned off again, and so on. For the frozen simulation approach a Newtonian material had been used. With that alternating approach the time step size could be reduced by a factor of 10 for the simulations which did not solve the momentum equations. Unfortunately it was found that the heat up rate was unrealistic for complex geometries used in HME. Temperatures up to 3311 K had been investigated within the screw-screw interface. The reason for this behaviour lies in the nature of conduction and convection. As there is no convection taking place without momentum and the conduction rate is negligibly small, high shear rates within the screw-screw interface lead to the very high temperatures as shown in Figure 5.4.1. Base on this findings the frozen simulation approach had been discarded.

6 Chapter 6.

Conclusion

As part of this work a viscosity model with exponential temperature dependence for SPH had been successfully tested and compared to existing valid viscosity models in CFD as well as experimental data. The results are in good agreement with a priori expectations. Furthermore it could be shown that SPH is a very promising tool to predict Newtonian and non-Newtonian temperature dependent fluid flow behaviour in complex geometries like the conveying element in HME.

The theoretical part of this work contains an overview of the hot melt extrusion process, the applications of HME in the field of pharmaceutical engineering, an description of smooth particle hydrodynamics and the derivation of governing equations in fluid dynamics regarding HME.

With this thesis the importance of temperature related phenomena in hot melt extrusion could be shown. The results indicate that without considering temperature dependence of the viscosity, a different range of temperature will be calculated, which would lead to different results for pressure characteristics, throughput rates, viscosities, velocities or shear rates. Especially in pharmaceutical engineering, where heat sensitive products are fabricated, a precise understanding of the proceedings within the devices is necessary. A minor change in temperature could lead to a total degradation of the API, or in the worst case to a destruction of the device.

It was also found that the computation time of the simulations carried out in SPH can be problematic. As the SPH code developed at RCPE is using uniform sized particles, the number of particles in complex geometries needed for a proper distribution can be enormous, if small gaps are present. One way of solving this problem could be achieved with a local refinement of the particle size. A refined distribution of the particles at very narrow regions would reduce computation time and also lead to an improvement of the results carried out by this thesis. Computation time reduction could also be achieved with multi-GPUs. Further improvements in the GPU-technologie will lead to a crucial reduction in computation time and therefor provide an refinement of the particle distribution.

Bibliography

[1] Andreas Eitzlmayr and Johannes Khinast. Co-rotating twin-screw extruders: Detailed analysis of conveying elements based on smoothed particle hydrodynamics. part 1: Hydrodynamics. *Chemical Engineering Science*, 134:861–879, 2015. i, 9, 22, 28

[2] George L Bata. The archimedean screw as an extruder; historical note. *Polymer Engineering & Science*, 24(9):624–625, 1984. ix, 1, 2

[3] P Chinna Reddy, KSC Chaitanya, and Y Madhusudan Rao. A review on bioadhesive buccal drug delivery systems: current status of formulation and evaluation methods. *DARU Journal of Pharmaceutical Sciences*, 19(6):385, 2011. ix, 3

[4] Inc. C.W. BrabenderÂ® Instruments. cwbrabender. http://www.cwbrabender.com/, June 2017. ix, 6

[5] Hot melt extrusion particle sciences-technical brief. 3, 2011. ix, 8, 9

[6] Bjorn Sjodin. What is the difference between fem, fdm, and fvm. http://www.machinedesign.com/fea-and-simulation/what-s-difference-between-fem-fdm-and-fvm, June 2017. ix, 23

[7] Linjie Zhu, Kwabena A Narh, and Kun S Hyun. Investigation of mixing mechanisms and energy balance in reactive extrusion using three-dimensional numerical simulation method. *International journal of heat and mass transfer*, 48(16):3411–3422, 2005. ix, 27, 28

[8] Daniel J Price. Smoothed particle hydrodynamics and magnetohydrodynamics. *Journal of Computational Physics*, 231(3):759–794, 2012. ix, 44

[9] D Deb and R Pramanik. Failure process of brittle rock using smoothed particle hydrodynamics. *Journal of Engineering Mechanics*, 139(11):1551–1565, 2013. ix, 45

[10] Kondor I. A1$_{D}OK_{X}PSdocumentationforsph, 2016. ix, 28, 43, 49, 51, 53, 54$

[11] Andreas Eitzlmayr and Johannes Khinast. Co-rotating twin-screw extruders: Detailed analysis of conveying elements based on smoothed particle hydrodynamics. part 1: Hydrodynamics. *Chemical Engineering Science*, 134:861–879, 2015. x, 25, 28, 66, 68, 73

[12] Barbara Aterini. Guidobaldo del monte (1545–1607). In *Distinguished Figures in Descriptive Geometry and Its Applications for Mechanism Science*, pages 153–180. Springer, 2016. 1

[13] Diane K Haberbusch. Viscosity regulation in polymer extrusion. 2013. 1

[14] Girish K Jani. Hot melt extrusion: An emerging technology in pharmaceuticals. 2015. 1

[15] P Maier. Kontinuierlich arbeitende knetmaschinen zur herstellung von schokoladen-massen. *Fette, Seifen, Anstrichmittel*, 61(8):686–690, 1959. 1

[16] Sandeep Singhal, Vikram K Lohar, and Vimal Arora. Hot melt extrusion technique. 2011. 1

[17] Mohammed Maniruzzaman, Joshua S Boateng, Martin J Snowden, and Dennis Douroumis. A review of hot-melt extrusion: process technology to pharmaceutical products. *ISRN pharmaceutics*, 2012, 2012. 1

[18] Klemens Kohlgrüber. *Co-rotating twin-screw extruder*. Carl Hanser Verlag GmbH Co KG, 2008. 2, 4, 6, 9, 34, 38, 72, 86

[19] Hemlata Patil, Roshan V Tiwari, and Michael A Repka. Hot-melt extrusion: from theory to application in pharmaceutical formulation. *AAPS PharmSciTech*, 17(1):20–42, 2016. 2, 4, 5, 6, 8, 10, 12, 14

[20] Th. Gabor M. Bastian. Plastifizierung von polymeren in gleichdrall doppelschneckenextrudern. 202. 4

[21] Jörg Breitenbach. Melt extrusion: from process to drug delivery technology. *European journal of Pharmaceutics and Biopharmaceutics*, 54(2):107–117, 2002. 4

[22] James L White. Twin screw extrusion: technology and principles. 1991. 5

[23] Michael M Crowley, Feng Zhang, Michael A Repka, Sridhar Thumma, Sampada B Upadhye, Sunil Kumar Battu, James W McGinity, and Charles Martin. Pharmaceutical applications of hot-melt extrusion: part i. *Drug development and industrial pharmacy*, 33(9):909–926, 2007. 5, 6, 9, 12, 17

[24] Chris Rauwendaal. *Polymer extrusion*. Carl Hanser Verlag GmbH Co KG, 2014. 5, 10, 17, 35, 36, 37, 40

[25] Winston Wang and Ica Manas-Zloczower. Dispersive and distributive mixing characterization in extrusion equipment. *Polym Eng Sci*, 41(6):1–068, 2001. 6

[26] L Cong and M Gupta. Simulation of distributive and dispersive mixing in a co-rotating twin-screw extruder. *J Soc Plast Eng Annu Tech (ANTEC)*, 54:300–304, 2008. 8

[27] Charlie Martin. Twin screw extruders as continuous mixers for thermal processing: a technical and historical perspective. *AAPS PharmSciTech*, 17(1):3–19, 2016. 8

[28] R Erdmenger. Apparatus for mixing and kneading liquid. *HIGHLY VISCOUS PLASTIC, POWDERED OR GRANULAR SUBSTANCES German Patent*, (813):154, 1951. 9

[29] Rina Chokshi and Hossein Zia. Hot-melt extrusion technique: a review. *Iranian Journal of Pharmaceutical Research*, pages 3–16, 2010. 10

[30] Chris Rauwendaal. *Understanding extrusion.* Hanser, 1998. 10, 35, 39

[31] J Baronsky-Probst, C-V Möltgen, W Kessler, and RW Kessler. Process design and control of a twin screw hot melt extrusion for continuous pharmaceutical tamper-resistant tablet production. *European Journal of Pharmaceutical Sciences*, 87:14–21, 2016. 11, 12

[32] Bo Lang, James W McGinity, and Robert O Williams III. Hot-melt extrusion–basic principles and pharmaceutical applications. *Drug development and industrial pharmacy*, 40(9):1133–1155, 2014. 12, 39

[33] Daniel Markl, Patrick R Wahl, José C Menezes, Daniel M Koller, Barbara Kavsek, Kjell Francois, Eva Roblegg, and Johannes G Khinast. Supervisory control system for monitoring a pharmaceutical hot melt extrusion process. *AAPS PharmSciTech*, 14(3):1034–1044, 2013. 12

[34] Mohammed Maniruzzaman, Joshua S Boateng, Martin J Snowden, and Dennis Douroumis. A review of hot-melt extrusion: process technology to pharmaceutical products. *ISRN pharmaceutics*, 2012, 2012. 13

[35] Dave A Miller, Jason T McConville, Wei Yang, Robert O Williams, and James W McGinity. Hot-melt extrusion for enhanced delivery of drug particles. *Journal of pharmaceutical sciences*, 96(2):361–376, 2007. 13

[36] Geert Verreck, Annelies Decorte, Koen Heymans, Jef Adriaensen, Dehua Liu, David Tomasko, Albertina Arien, Jef Peeters, Guy Van den Mooter, and Marcus E Brewster. Hot stage extrusion of p-amino salicylic acid with ec using co 2 as a temporary plasticizer. *International journal of pharmaceutics*, 327(1):45–50, 2006. 14

[37] Wenping Wang, Qian Kang, Na Liu, Qing Zhang, Yewen Zhang, Hui Li, Bochen Zhao, Yanyan Chen, Yi Lan, Qiang Ma, et al. Enhanced dissolution rate and oral bioavailability of ginkgo biloba extract by preparing solid dispersion via hot-melt extrusion. *Fitoterapia*, 102:189–197, 2015. 14

[38] L Diane Bruce, Navnit H Shah, A Waseem Malick, Martin H Infeld, and James W McGinity. Properties of hot-melt extruded tablet formulations for the colonic delivery of 5-aminosalicylic acid. *European Journal of Pharmaceutics and Biopharmaceutics*, 59(1):85–97, 2005. 14

[39] Ellen Verhoeven, TRM De Beer, Guy Van den Mooter, Jean Paul Remon, and Chris Vervaet. Influence of formulation and process parameters on the release characteristics of ethylcellulose sustained-release mini-matrices produced by hot-melt extrusion. *European journal of pharmaceutics and biopharmaceutics*, 69(1):312–319, 2008. 14

[40] Joseph Price Remington, David B Troy, and Paul Beringer. *Remington: The science and practice of pharmacy*, volume 1. Lippincott Williams & Wilkins, 2006. 15

[41] Chinna Reddy Palem, Sunil Kumar Battu, Sindhuri Maddineni, Ramesh Gannu, Michael A Repka, and Madhusudan Rao Yamsani. Oral transmucosal delivery of domperidone from immediate release films produced via

hot-melt extrusion technology. *Pharmaceutical development and technology*, 18(1):186–195, 2013. 15

[42] Zahra Ghalanbor. *Formulation development of biodegradable implants for extended parenteral delivery of protein drugs*. PhD thesis, Freie Universität Berlin, 2011. 15

[43] DeXia Li, Gang Guo, Xin Deng, RangRang Fan, QingFa Guo, Min Fan, Jian Liang, Feng Luo, and ZhiYong Qian. Pla/peg-ppg-peg/dexamethasone implant prepared by hot-melt extrusion for controlled release of immunosuppressive drug to implantable medical devices, part 2: in vivo evaluation. *Drug delivery*, 20(3-4):134–142, 2013. 15

[44] Ramona Baumgartner, Andreas Eitzlmayr, Nadejda Matsko, Carolin Tetyczka, Johannes Khinast, and Eva Roblegg. Nano-extrusion: a promising tool for continuous manufacturing of solid nano-formulations. *International journal of pharmaceutics*, 477(1):1–11, 2014. 16

[45] Ana Almeida, Lien Saerens, Thomas De Beer, Jean Paul Remon, and Chris Vervaet. Upscaling and in-line process monitoring via spectroscopic techniques of ethylene vinyl acetate hot-melt extruded formulations. *International journal of pharmaceutics*, 439(1):223–229, 2012. 16

[46] Barbara Van Melkebeke, Chris Vervaet, and Jean Paul Remon. Validation of a continuous granulation process using a twin-screw extruder. *International journal of pharmaceutics*, 356(1):224–230, 2008. 16

[47] Isaac Ghebre-Sellassie, Matthew J Mollan Jr, Nitin Pathak, Mayur Lodaya, and Mebrahtu Fessehaie. Continuous production of pharmaceutical granulation, December 31 2002. US Patent 6,499,984. 16

[48] B Mu and MR Thompson. Examining the mechanics of granulation with a hot melt binder in a twin-screw extruder. *Chemical engineering science*, 81:46–56, 2012. 16

[49] H Potente. Existing scale-up rules for single-screw plasticating extruders. *International Polymer Processing*, 6(4):267–278, 1991. 17

[50] Sandra Guns, Vincent Mathot, Johan A Martens, and Guy Van den Mooter. Upscaling of the hot-melt extrusion process: comparison between laboratory scale and pilot scale production of solid dispersions with miconazole and kollicoat® ir. *European Journal of Pharmaceutics and Biopharmaceutics*, 81(3):674–682, 2012. 17

[51] Adam Dreiblatt. Technological considerations related to scale-up of hot-melt extrusion processes. *Hot-Melt Extrusion: Pharmaceutical Applications*, pages 285–300, 2012. 17

[52] James C DiNunzio, Feng Zhang, Charlie Martin, and James W McGinity. Melt extrusion. In *Formulating poorly water soluble drugs*, pages 311–362. Springer, 2012. 20

[53] Silvio Eccher and Aldo Valentinotti. Experimental determination of velocity profiles in an extruder screw. *Industrial & Engineering Chemistry*, 50(5):829–836, 1958. 20

[54] WD Mohr, JB Clapp, and FC Starr. Flow patterns in a non-newtonian fluid in a single-screw extruder. *Polymer Engineering & Science*, 1(3):113–120, 1961. 20

[55] KP Choo, NR Neelakantan, and JFT Pittman. Experimental deep-channel velocity profiles and operating characteristics for a single-screw extruder. *Polymer Engineering & Science*, 20(5):349–356, 1980. 20

[56] Kathryn L McCarthy, Robert J Kauten, and Cynthia K Agemura. Application of nmr imaging to the study of velocity profiles during extrusion processing. *Trends in Food Science & Technology*, 3:215–219, 1992. 21

[57] Murali Chandrasekaran and Mukund V Karwe. Measurement of velocity profiles in reverse-screw elements of a twin-screw extruder. *AIChE journal*, 43(10):2424–2431, 1997. 21

[58] MUKUND V KARWE and VALENTINAS SERNAS. Application of laser doppler anemometry to measure velocity distribution inside the screw channel of a twin-screw extruder. *Journal of food process engineering*, 19(2):135–152, 1996. 21

[59] T Nietsch, Ph Cassagnau, and A Michel. Melt temperatures and residence times in an extruder by infrared spectroscopy. *International Polymer Processing*, 12(4):307–315, 1997. 21

[60] AK Wood, YH Judeh, and M Yue. Patent application gb 2291197, 1996. 21

[61] N. Sombatsompop and M. Panapoy. Effect of screw rotating speed on polymer melt temperature profiles in twin screw extruder. *Journal of Materials Science*, 35(24):6131–6137, 2000. 21

[62] Juha-Pekka Pöyry. Extruder die coatings in polymer processing. 2012. 21

[63] TJ Chung. *Computational fluid dynamics.* Cambridge university press, 2010. 22

[64] Open university. Introduction finite element analysis. http://www.open.edu/openlearn/science-maths-technology/introduction-finite-element-analysis/content-section-1.5, June 2017. 23

[65] W Chajec and A Dziubiński. Advances in mechanics: Theoretical, computational and interdisciplinary issues. 24

[66] Corina Höfler. *Entwicklung eines Smoothed Particle Hydrodynamics (SPH) Codes zur numerischen Vorhersage des Primärzerfalls an Brennstoffeinspritzdüsen.* Logos Verlag Berlin GmbH, 2013. 24

[67] Roland Speith. *Untersuchung von smoothed particle hydrodynamics anhand astrophysikalischer Beispiele.* R. Speith, 1998. 24

[68] Leon B Lucy. A numerical approach to the testing of the fission hypothesis. *The astronomical journal*, 82:1013–1024, 1977. 24

[69] Robert A Gingold and Joseph J Monaghan. Smoothed particle hydrodynamics: theory and application to non-spherical stars. *Monthly notices of the royal astronomical society*, 181(3):375–389, 1977. 24

[70] Luo-xing Li, Jie Zhou, and J Duszczyk. Prediction of temperature evolution during the extrusion of 7075 aluminium alloy at various ram speeds by means of 3d fem simulation. *Journal of Materials Processing Technology*, 145(3):360–370, 2004. 25

[71] SJ Liang, ZY Liu, and ED Wang. Simulation of extrusion process of az31 magnesium alloy. *Materials Science and Engineering: A*, 499(1):221–224, 2009. 26

[72] LX Li, KP Rao, Y Lou, and DS Peng. A study on hot extrusion of ti–6al–4v using simulations and experiments. *International Journal of Mechanical Sciences*, 44(12):2415–2425, 2002. 26

[73] A Altınkaynak, M Gupta, MA Spalding, and SL Crabtree. Melting in a single screw extruder: experiments and 3d finite element simulations. *International Polymer Processing*, 26(2):182–196, 2011. 26

[74] Chang Liang, Kui Sheng Wang, and Bing Luo. Analysis on melting mechanism in the cross section of co-rotating twin screw extruder. In *Advanced Materials Research*, volume 548, pages 571–575. Trans Tech Publ, 2012. 26

[75] Raman V Chiruvella, Y Jaluria, and Mukund V Karwe. Numerical simulation of the extrusion process for food materials in a single-screw extruder. *Journal of Food Engineering*, 30(3):449–467, 1996. 27

[76] Eleni Taliadorou, Georgios C Georgiou, and Evan Mitsoulis. Numerical simulation of the extrusion of strongly compressible newtonian liquids. *Rheologica Acta*, 47(1):49–62, 2008. 27

[77] Andreas Eitzlmayr and Johannes Khinast. Co-rotating twin-screw extruders: Detailed analysis of conveying elements based on smoothed particle hydrodynamics. part 2: Mixing. *Chemical Engineering Science*, 134:880–886, 2015. 28

[78] Andreas Eitzlmayr and Johannes Khinast. Co-rotating twin-screw extruders: Detailed analysis of conveying elements based on smoothed particle hydrodynamics. part 2: Mixing. *Chemical Engineering Science*, 134:880–886, 2015. 28

[79] Dalibor Jajcevic, Eva Siegmann, Charles Radeke, and Johannes G Khinast. Large-scale cfd–dem simulations of fluidized granular systems. *Chemical Engineering Science*, 98:298–310, 2013. 29

[80] John Vlachopoulos and David Strutt. Basic heat transfer and some applications in polymer processing. *Plastics Technicianâs Toolbox*, 2:21–33, 2002. 33

[81] John Vlachopoulos and David Strutt. The role of rheology in polymer extrusion. In *New Technology for Extrusion Conference. Milan, Italy. Nov*, pages 20–21, 2003. 33, 37, 39, 41

[82] Purna Chandra Barman, Rishi Raj Kairi, Ashoke Das, and Rabiul Islam. An overview of non-newtonian fluid. *International Journal of Applied Science and Engineering*, 4(2):97–101, 2016. 34

[83] AH Khalili Garakani, N Mostoufi, F Sadeghi, M Hosseinzadeh, H Fatourechi, MH Sarrafzadeh, and MR Mehrnia. Comparison between different models for rheological characterization of activated sludge. *Iranian journal of environmental health science & engineering*, 8(3):255, 2011. 36

[84] Winslow H Herschel and Ronald Bulkley. Konsistenzmessungen von gummibenzollösungen. *Colloid & Polymer Science*, 39(4):291–300, 1926. 38

[85] Eugene Cook Bingham. *Fluidity and plasticity*, volume 2. McGraw-Hill Book Compny, Incorporated, 1922. 38

[86] Markus Reiner and Herbert Leaderman. Deformation, strain, and flow. *Physics Today*, 13(9):47–48, 1960. 38, 39

[87] Pierre J Carreau, Ian F MacDonald, and R Byron Bird. A nonlinear viscoelastic model for polymer solutions and meltsâii. *Chemical Engineering Science*, 23(8):901–911, 1968. 38

[88] WR Moore and AM Brown. Viscosity-temperature relationships for dilute solutions of cellulose derivatives: I. temperature dependence of solution viscosities of ethyl cellulose. *Journal of Colloid Science*, 14(1):1–12, 1959. 39

[89] Leslie Howard Sperling. *Introduction to physical polymer science.* John Wiley & Sons, 2005. 39

[90] Raffi M Turian. Viscous heating in the cone-and-plate viscometerâiii: Non-newtonian fluids with temperature-dependent viscosity and thermal conductivity. *Chemical Engineering Science*, 20(8):771–781, 1965. 40, 57, 59

[91] John D Ferry. *Viscoelastic properties of polymers.* John Wiley & Sons, 1980. 42

[92] Anthony G Atkins, Tony Atkins, and Marcel Escudier. *A dictionary of mechanical engineering.* Oxford University Press, 2013. 43

[93] Joe J Monaghan. Smoothed particle hydrodynamics. *Reports on progress in physics*, 68(8):1703, 2005. 43, 45

[94] DJ Price and JJ Monaghan. An energy-conserving formalism for adaptive gravitational force softening in smoothed particle hydrodynamics and n-body codes. *Monthly Notices of the Royal Astronomical Society*, 374(4):1347–1358, 2007. 46

[95] Raffi M Turian and R Byron Bird. Viscous heating in the cone-and-plate viscometerâii: Newtonian fluids with temperature-dependent viscosity and thermal conductivity. *Chemical Engineering Science*, 18(11):689–696, 1963. 57, 59, 68

[96] Juri Pawlowski. *Die Ähnlichkeitstheorie in der physikalisch-technischen Forschung: Grundlagen und Anwendung.* Springer-Verlag, 2013. 72

[97] Andreas Eitzlmayr and Johannes Khinast. Co-rotating twin-screw extruders: Detailed analysis of conveying elements based on smoothed particle hydrodynamics. part 1: Hydrodynamics. *Chemical Engineering Science*, 134:861–879, 2015. 73

[98] M Bierdel. Computational fluid dynamics. *Co-Rotating Twin-Screw Extruders, Carl Hanser Publishers, Munich*, pages 139–158, 2008. 73

[99] Andreas Eitzlmayr, Josip Matić, and Johannes Khinast. Analysis of flow and mixing in screw elements of corotating twin-screw extruders via sph. *AIChE Journal*, 63(6):2451–2463, 2017. 74

[100] Andreas Eitzlmayr, Gerold Koscher, and Johannes Khinast. A novel method for modeling of complex wall geometries in smoothed particle hydrodynamics. *Computer Physics Communications*, 185(10):2436–2448, 2014. 75

Appendix A.

A Algebraic and differential operations for scalars, vectors and tensors for Cartesian coordinates

Del Operator:

$$\nabla = \left(\frac{\partial}{\partial x}, \frac{\partial}{\partial y}, \frac{\partial}{\partial z},\right) \tag{A.1.1}$$

Laplacian Operator:

$$\nabla^2 = \nabla \cdot \nabla = \left(\frac{\partial^2}{\partial x^2} + \frac{\partial^2}{\partial y^2} + \frac{\partial^2}{\partial z^2}\right) \tag{A.1.2}$$

Gradient:

$$\nabla p = \left(\frac{\partial p}{\partial x}, \frac{\partial p}{\partial y}, \frac{\partial p}{\partial z},\right) \tag{A.1.3}$$

Vector Gradient:

$$\nabla \boldsymbol{u} = (\nabla u, \nabla v, \nabla w) \tag{A.1.4}$$

Divergence:

$$\nabla \cdot \boldsymbol{u} = \frac{\partial u}{\partial x} + \frac{\partial v}{\partial y} + \frac{\partial w}{\partial z} \tag{A.1.5}$$

Directional Derivative:

$$\boldsymbol{u} \cdot \boldsymbol{\nabla} = u\frac{\partial}{\partial x} + v\frac{\partial}{\partial y} + w\frac{\partial}{\partial z} \tag{A.1.6}$$

B

Appendix B.

C++ source code

```
/* Turian 3
 * non-Newtonian, couette flow
 * Validation Velocity/Temperature/Viscosity
 * Turian et al. 1964
*/

#include <iostream>
#include <fstream>
#include <stdio.h>
#include <math.h>
#include <cstdlib>

  using namespace std;

  int    numPoints   = 50;
  double alpha_one   = 0.0;
  double alpha_two   = 0.0;
  double beta        = 0.5;
  double beta_one    = 0.0;
  double beta_two    = 0.0;
  double mu_zero     = 0.50
  double V           = 0.1;
  double k_zero      = 0.00001;
  double T_zero      = 273;
  double b           = 1.0;
  double dx          = 1.0 / numPoints;
  double n_zero      = 1;
  double B           = 1;
  double mu;
  double un;
  double unp1;
  double unm1;
  double dy;
  double du;

int main () {

  double s           = 1 / n_zero;
  double gamma_one   = (B*s) / 1;
double gamma_two    = pow(B * s, 2) / 2;
double zeta;
double zetap1;
double zetam1;
double phi[numPoints];
double theta;
double theta_1;
double K            = du/dy;
double Br           = (mu_zero * double (pow (V, 2)))
                      /(k_zero * T_zero);

std::cout << "Br-nbr: " << Br << std::endl;


ofstream out;
ofstream out2;
out.open("Velocity.dat");

  for (int i = 0; i <= numPoints; i++) {

        zeta    = i * dx;

        phi[i]  = zeta - Br/12 * gamma_one * (zeta - 3
                * (pow (zeta, 2))   + 2 *  (pow (zeta, 3)))
                + (pow (Br, 2)) / 720 *  (pow (gamma_one, 2))
                * ((5 * n_zero + 4) * zeta - 15 * (n_zero + 1)
                *  (pow (zeta, 2)) + 10 * (n_zero +2)
                *  (pow (zeta, 3)) - 15 *  (pow (zeta, 4)) + 6
                * (pow(zeta, 5))) + ((pow (Br, 2)) / 240)
                * (alpha_one * gamma_one - 2 * gamma_two)
                * (zeta - 10 *  (pow (zeta, 3)) + 15
                *  (pow (zeta, 4)) - 6 *  (pow (zeta, 5)));
                                   //+ O * (pow (zeta, 3))

    out << zeta << "\t" << phi[i] << endl;
    std::cout << "Velocity: " << zeta * b << "\t" <<

    phi[i] * V << std::endl;
  }


out.close();
out.open("Temperature.dat");
out2.open("Viscosity.dat");

  for (int i = 0; i <= numPoints; i++) {
      zeta    =  i * dx;
      zetap1  = (i + 1) * dx;    //Central Differencial method
      zetam1  = (i - 1) * dx;    //Central Differencial method

      theta_1 = (Br / 2 * (zeta -  (pow (zeta, 2))))
                - ((pow (Br, 2)) / 24) * gamma_one
                * (n_zero * zeta - (n_zero + 1) * (pow (zeta, 2))
                + 2 * (pow (zeta, 3)) - (pow (zeta, 4)))
                - (pow (Br, 2) / 8) * alpha_one * (pow (zeta, 2)
                - 2 *  (pow (zeta, 3)) + (pow (zeta, 4)))
                + (pow (Br, 3)/2880) * pow (gamma_one, 2)
                * ((3 * n_zero) * (5 * n_zero + 1) * zeta
                - (15 * n_zero + 8) * (n_zero +1)
                * (pow (zeta, 2)) + 20 * (2 * n_zero + 1)
                * (pow (zeta, 3)) - 20 * (n_zero + 1)
                * (pow (zeta, 4)) + 12 * (pow (zeta, 5))
                - 4 *  (pow (zeta, 6))) + ((pow (Br, 3))/480)
                * alpha_one * gamma_one
                * (n_zero * zeta + (9 * n_zero - 1)
                * (pow (zeta, 2)) - 10 * (2 * n_zero + 1)
                * pow (zeta, 3)) + 5 * (2 * n_zero + 7)
                * (pow (zeta, 4)) - 36 * (pow (zeta, 5))
                + 12 *  (pow (zeta, 6))) + ((pow (Br, 3))/48)
                * (3 * pow (alpha_one, 2) - 2 * alpha_two)
                * (pow (zeta, 3) - 3 * (pow (zeta, 4))
                + 3 * (pow (zeta, 5)) - (pow (zeta, 6)))
                + ((pow (Br, 3))/240) * gamma_two
                * (- n_zero * zeta + (n_zero +1) * (pow (zeta, 2))
                - 5* (pow (zeta, 4)) + 6 * (pow (zeta, 5)) - 2
                * (pow (zeta, 6)));    //+0.001 * pow (Br, 4)

      theta   = theta_1 * 273 + 273;

  out << zeta << "\t" << theta << endl;
  std::cout << "Temperature: " << zeta * b <<"\t"<<
  theta << std::endl;
                  //Central diff method
if  (i == 0)

      K       = (phi[i+1] - phi[i]) / dx;      //Bottom boundary

else if (i == numPoints)

      K       = (phi[i] - phi[i-1]) / dx;      //Top boundary
else
```

```
          K        = (phi[i+1] - phi[i-1]) / (2.0 * dx);


          mu        = mu_zero * (exp (-beta * theta_1))* (pow (K,-0.5));

      out2 << zeta << "\t" << mu << endl;
      std::cout << "Viscosity: " << zeta << "\t" << mu << std::endl;
    }

  out.close();
  out2.close();

  return 0;
}

/* Turian 2 Case B1
 * Newtonian, couette flow
 * Validation Velocity/Temperature/Viscosity
 * Turian et al. 1964
*/

#include <iostream>
#include <fstream>
#include <stdio.h>
#include <math.h>
#include <cstdlib>

  using namespace std;

  int      numPoints = 10;
  double   mu_zero   = 0.5;
  double   V         = 0.1;
  double   k_zero    = 0.004;
  double   T_zero    = 273;
  double   H         = 1;
  double   dy        = H / numPoints;


int main () {

  double   phi;
  double   theta;
  double   beta        = 0.5;
  double   zeta;
  double   Br          = mu_zero * double (pow (V, 2))/(k_zero * T_zero);
  std::cout << "Br-nbr: " << Br << std::endl;

  ofstream out;
  out.open("Turian2b1velo.dat");

    for (int i = 0; i <= numPoints; i++) {

          zeta  =   i * dy;
          phi   =   1.0 / 2.0  * ( (pow (1.0 + (8.0 / (Br * beta)),
                    (1.0 / 2.0))) * (tanh ((2 * zeta -1.0)
                    * (asinh (sqrt ((Br * beta) / 8.0))))) + 1.0);


        out << zeta << "\t" << phi << endl;
        std::cout << "Velocity: " << zeta
        << ' ' << phi * V << std::endl;
    }

        out.close();
  out.open("Turian2b1temp.dat");

    for (int i  =   0; i <= numPoints; i++) {

          zeta  =   i * dy;
          theta =   1.0 / beta * log ((1 + Br * beta / 8.0)
                    * (1.0 - (pow (tanh ((2 * zeta -1.0)
                    * asinh ( sqrt ((Br * beta) / 8.0))), 2.0))));

        out << zeta << "\t" << theta << endl;
        std::cout << "Temperature: " << zeta << ' '
        << theta << std::endl;
    }

  return 0;
}
```